Development, Characterization, Alignment and Experimental Validation of Partial Sphere Target Arrays for Advanced Proton Acceleration Studies

Zur Erlangung des Grades eines Doktors der Naturwissenschaften (Dr. rer. nat.)
Genehmigte Dissertation von Timo Sebastian Bauer
Tag der Einreichung: 16.04.2025, Tag der Prüfung: 12.05.2025

1. Gutachten: Prof. Dr. Markus Roth
2. Gutachten: Prof. Dr. Stephan Kuschel
Darmstadt, Technische Universität Darmstadt

TECHNISCHE
UNIVERSITÄT
DARMSTADT

Physics Department
Institut für Kernphysik
Prof. Dr. Markus Roth

Development, Characterization, Alignment and Experimental Validation of Partial Sphere Target Arrays for Advanced Proton Acceleration Studies

Accepted doctoral thesis by Timo Sebastian Bauer

Date of submission: 16.04.2025
Date of thesis defense: 12.05.2025

Darmstadt, Technische Universität Darmstadt

Bitte zitieren Sie dieses Dokument als:
URN: urn:nbn:de:tuda-tuprints-300725
URL: http://tuprints.ulb.tu-darmstadt.de/30072
Jahr der Veröffentlichung auf TUprints: 2025

Erklärungen laut Promotionsordnung

§ 8 Abs. 1 lit. c PromO

Ich versichere hiermit, dass die elektronische Version meiner Dissertation mit der schriftlichen Version übereinstimmt.

§ 8 Abs. 1 lit. d PromO

Ich versichere hiermit, dass zu einem vorherigen Zeitpunkt noch keine Promotion versucht wurde. In diesem Fall sind nähere Angaben über Zeitpunkt, Hochschule, Dissertationsthema und Ergebnis dieses Versuchs mitzuteilen.

§ 9 Abs. 1 PromO

Ich versichere hiermit, dass die vorliegende Dissertation selbstständig und nur unter Verwendung der angegebenen Quellen verfasst wurde.

§ 9 Abs. 2 PromO

Die Arbeit hat bisher noch nicht zu Prüfungszwecken gedient.

Darmstadt, 16.04.2025

T. Bauer

Abstract

Proton Fast Ignition ist ein fortschrittliches Trägheitsfusionsverfahren (Inertial Confinement Fusion), das auf der Entkopplung von Kompression und Zündung des Deuterium-Tritium (DT) Brennstoffs basiert. Durch diese Entkopplung wird eine effizientere Umwandlung von Laserenergie in freigesetzte Fusionsenergie bei gleichzeitig reduzierten Laseranforderungen erwartet.

Die erforderliche Zündungsenergie für Proton Fast Ignition, wird durch einen kollimierten Protonenstrahl in ein kleines Volumen im vorkomprimierten DT Brennstoff eingebracht. Eine zentrale Herausforderung ist die Erzeugung dieses präzisen, hochintensiven laserinduzierten Protonenstrahls. In dieser Arbeit werden systematisch die Fokussierungseigenschaften von Laser getriebenen Protonen untersucht, die mittels Target Normal Sheath Acceleration (TNSA) von Kugelkalotten erzeugt werden.

Vergangene Untersuchungen in diesem Gebiet verglichen wenige Probenkonfigurationen, limitiert durch eine geringe Anzahl an Schüssen. Diese Einschränkung limitiert die statistische Auswertung der Daten und verhindert eine umfassende Untersuchung verschiedener Laserparameter oder Probenkonfigurationen. Neuere Lasersysteme ermöglichen mittlere Schussraten in der Größenordnung von ca. 1 Hz. Um das Potential dieser Systeme für Untersuchungen zur Protonenfokussierung auszuschöpfen zu können, wird in dieser Arbeit ein neuartiges Fertigungsverfahren entwickelt. Dieses ermöglicht erstmals die Herstellung von Kugelkalotten mit Durchmessern von 220 µm, 325 µm und 525 µm in großen Stückzahlen (>1000).

Durch die gründliche metrologische Analyse und Qualitätsprüfung wurde zudem ein zweistufiges Ausrichtungsverfahren entwickelt.

Im Rahmen dieser Arbeit wurden 320 Kugelkalotten verteilt über 42 unterschiedliche Probenkonfigurationen am L-ALPEH Laser der Colorado State University bestrahlt. Die 200 Proben pro Halter werden vor dem Experiment im Labor montiert und vermessen. Kombiniert mit einer schnellen Montage und vereinfachtem Einmessen während des Experiments, kann die Zeit zwischen den Schusssequenzen deutlich reduziert werden. Die beschriebenen Verfahren ermöglichen – in Anbetracht der komplexen Probengeometrie – erstmals Schussfrequenzen von $^1/_3$Hz.

Protonen-Gitterradiographie diente zur Bestimmung des Protonenstrahldurchmessers an unterschiedlichen Distanzen zum Apex in einem Bereich von $\sim$ 280 µm bis 960 µm. Weiterhin erlaubte die Radiographie die Bestimmung der virtuellen Protonenpunktquelle.

In einer weiteren Konfiguration werden Sekundärfolien in Abständen von 160 µm bis 320 µm hinter den Apizes der Kalotten montiert. Diese werden von durch den Energieeintrag des Protonenstrahls isochor erhitzt und die dabei entstehende thermische Strahlung wird mittels einer EUV Kamera zeitlich integriert gemessen. Diese Messungen zeigen, dass Protonenstrahlen von kleineren, vom Laser gut ausgeleuchteten Kalotten über eine lange Distanz kollimiert sind. Im Gegensatz dazu, zeigen Protonenstrahlen von schlecht ausgeleuchteten großen Kalotten keine Kollimation. Im Zuge der Vorbereitungen für das Experiment wurden Particle-in-Cell (PIC) Simulationen durchgeführt, deren Resultate mit den zuvor genannten Ergebnissen übereinstimmen.

Zusammenfassend wurde in dieser Dissertation ein Verfahren entwickelt, mit dem Kugelkalotten für die Fokussierung lasergetriebener Protonen in Serie gefertigt, eingerichtet und vermessen werden können. Die erzielten Ergebnisse bilden die Grundlage für groß angelegte Parameterstudien zur Optimierung der Protonenbeschleunigung und -fokussierung im Rahmen der Proton Fast Ignition.

Abstract

Proton Fast Ignition is an advanced Inertial Confinement Fusion scheme that is based on decoupling compression and heating of Deuterium-Tritium (DT) fuel, paving a promising path towards higher fusion energy gain with reduced laser requirements. A key challenge in Proton Fast Ignition is generating precisely tailored, high-intensity proton beams, that can deposit the necessary energy into a small volume of the pre-compressed DT fuel. This work addresses this challenge by systematically studying the focusing properties of protons accelerated via Target Normal Sheath Acceleration (TNSA) from partial sphere targets.

Past studies in this field have been comparing few target configurations with, at most, tens of shots, massively limiting the statistical evaluation of the data while impeding the exploration of target and laser parameters. To support the medium repetition rate ($\sim 1\,\mathrm{Hz}$) experiments, a novel fabrication method was developed to produce 1050 partial sphere targets ranging in three sizes ($\varnothing 220\,\mu\mathrm{m}$, $\varnothing 325\,\mu\mathrm{m}$ and $\varnothing 525\,\mu\mathrm{m}$), an unprecedented scale in this domain. Consistent target quality was ensured through comprehensive metrology, including automated individual position measurements of 200 targets mounted in a frame. This enabled the development of a two-stage alignment procedure aimed at achieving rapid turnaround times and ensuring rapid, precise target alignment in the experimental chamber, enabling a repetition rate of $1/3$Hz under optimal conditions, an unprecedented feat given the target's complex geometry.

The partial sphere targets were shot at the L-ALEPH laser system at the Colorado State University, resulting in 320 shots across 42 different target configurations. Proton mesh radiography provided energy resolved beam size measurements at distances of $\sim 280\,\mu\mathrm{m}$ to $960\,\mu\mathrm{m}$ from the target's apex, as well as the virtual focus position. Secondary foils, heated by the proton beam at distances of $160\,\mu\mathrm{m}$ to $320\,\mu\mathrm{m}$ from the apex, were observed by an XUV imager. This revealed that smaller, well illuminated partial spheres generated a proton beam with extended collimation, in contrast to larger partial spheres with poorer illumination. These findings validated Particle-in-Cell (PIC) simulations preceding the campaign.

This thesis demonstrates reliable large-batch fabrication and fast target alignment in the context of a comprehensive experimental study on the focusing of TNSA protons generated from partial sphere targets. These results enable future large scale parametric studies centered on optimizing proton acceleration and focusing, contributing to the advancement of Proton Fast Ignition research by enabling large parametric studies on the new generation of high energy medium repetition rate facilities.

Contents

1 Introduction 1

2 Laser Plasma Interactions 5
- 2.1 Ionization and Plasma Generation . . . 5
- 2.2 Plasma Properties . . . 7
- 2.3 Single Electron Motion in an Electric Field . . . 8
- 2.4 Laser Absorption Processes and Energy Transfer in Overdense Plasmas . . . 9
- 2.5 Target Normal Sheath Acceleration . . . 11

3 Methodology 15
- 3.1 Radiochromic Film . . . 15
  - 3.1.1 Application . . . 18
  - 3.1.2 Mesh Magnification and Ray-tracing . . . 20
- 3.2 XUV Imaging . . . 25
- 3.3 Metrology . . . 26
  - 3.3.1 Confocal Measurement . . . 26
  - 3.3.2 Confocal Scanning Microscope . . . 27
  - 3.3.3 Analysis of a 3D areal Surface Texture . . . 27
- 3.4 Electroplating . . . 29

4 Arrays of Partial Sphere Targets 31
- 4.1 Design Description . . . 32
- 4.2 Fabrication of Spherical Targets . . . 34
- 4.3 Manufacturing Evaluation . . . 38
  - 4.3.1 Spherical Targets . . . 38
  - 4.3.2 Assembly . . . 43
- 4.4 Target Alignment . . . 45
  - 4.4.1 Concept . . . 46
  - 4.4.2 Evaluation . . . 46

5 Experiment - Proton Focusing with Partial Sphere Targets 49
- 5.1 Experimental Setup . . . 49
- 5.2 Focusing Dynamics of Hemispherical Targets investigated through Particle-In-Cell Simulations 51
- 5.3 Proton Beam Measurements using Radiochromic Film Stacks . . . 53
  - 5.3.1 Energy Conversion and Energy Distribution . . . 53
  - 5.3.2 Magnification and Virtual Focus Position . . . 55
  - 5.3.3 Proton Beam Size Determination and Comparison with Numerical Data . . . 59

6 Outlook 65

1 Introduction

Over the last decades, advances of ultra-high-intensity laser are continuously opening new frontiers in high-energy density physics and laser driven particle acceleration. Laser driven particle sources have been extensively studied, by tailoring laser parameters, target shape and structure for a variety of applications, like the generation of warm dense matter samples, equation of state studies, neutron production (Macchi et al., 2013; Roth et al., 2013). One of the most compelling application is Inertial Confinement Fusion(ICF), in particular Proton Fast Ignition (PFI) – the motivation behind the studies presented in this thesis (Roth et al., 2001).

In direct drive inertial confinement fusion, a capsule of solid deuterium and tritium is evenly irradiated by high-intensity short pulse lasers (Craxton et al., 2015; Nuckolls et al., 1972) , resulting in a blow-off of the outer shell of the fuel capsule. This drives a high velocity ($\sim 400\,\mathrm{km\,s^{-1}}$) implosion, which compresses the fuel and, if the pressure and temperature are sufficient, ignites[1] the deuterium tritium mixture in the central 'hotspot'. This scheme requires precise control and high uniformity of the high energy laser pulses.

An alternative, advanced approach offer Fast Ignition (Fernández et al., 2014; Kodama et al., 2001; Roth et al., 2001; Tabak et al., 1994) schemes, with a separation of the compression and ignition into two separate steps. One flavour of Fast Ignition is Proton Fast Ignition (PFI), where a hollow capsule made from solid deuterium-tritium is spherically compressed by high-intensity short pulse lasers, with relaxed requirements for the required compression and implosion velocity ($\sim 200\,\mathrm{km\,s^{-1}}$). In a separate step, a proton beam generated from a solid target driven by a high intensity ultra-short laser pulse will then heat a small volume of the pre-compressed matter, resulting in ignition. Here protons offer a preferable characteristic over electrons as they can penetrate a dense plasma but still deposit their energy relatively localized at the location of their Bragg peak (Atzeni et al., 2002; Roth et al., 2002). PFI promises an overall lower amount of laser energy required due to the relaxed implosion requirements, which also decreases the requirements on the uniformity on the lasers and capsule. The separation of the compression and ignition offers more control over the heating profile, allowing for a separate optimization of the two parts, at the cost of introducing a more complex target. As PFI aims to deliver the necessary energy to the hotspot more efficiently, therefore a higher fusion yield for a given laser energy can be expected, making this approach attractive for energy-production (Honrubia et al., 2009).

An effective and well studied mechanism for such ion acceleration is Target Normal Sheath Acceleration (TNSA). Here the laser drives hot electrons through a thin target, which results in a strong charge separation on the target's laser averted (rear) surface. This sheath field then accelerates ions from the surface (Fuchs et al., 2006; Macchi et al., 2013; M. S. Schollmeier, 2009). The resulting beam is highly laminar despite a broad energy distribution, with a relatively low divergence of about 8° to 16° (M. S. Schollmeier, 2009). It further carries a significant percentage of the beams energy and inherits a temporal profile similar to the one of the driving laser, making it attractive for the generation of short, high intensity beams, required for PFI (Daido et al., 2012).

Ion beams driven by TNSA from plain, flat targets are divergent, making them unfeasible to heat a small volume of dense plasma. But, the temporal and spatial profile can be shaped by manipulating the laser

---

[1] starts a fusion reaction

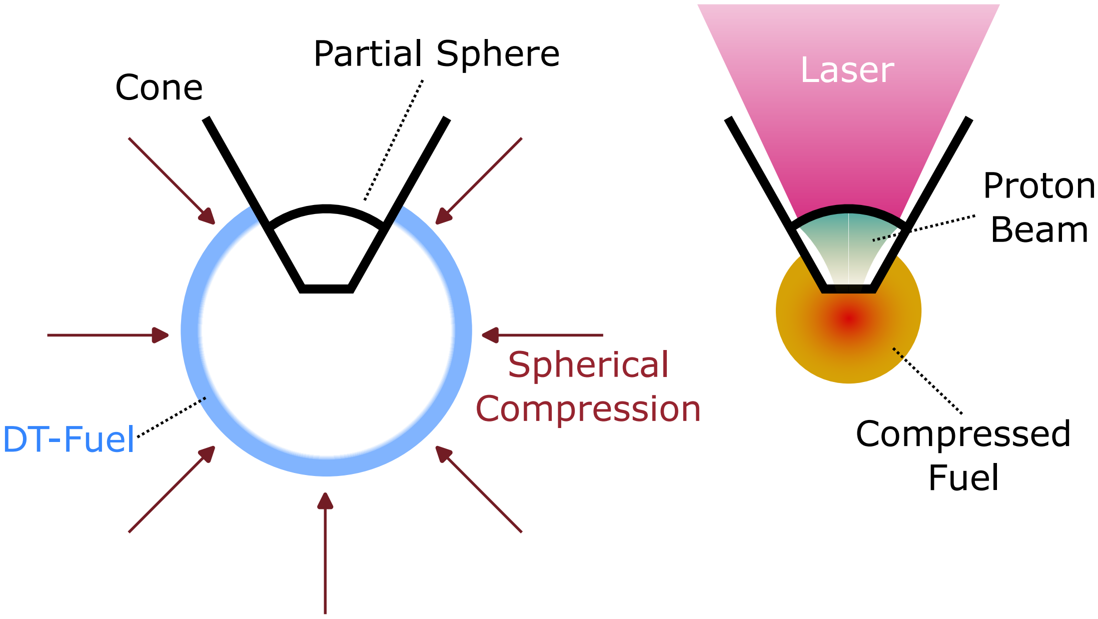

Figure 1.1: Schematic of the concept of Proton Fast Ignition. The hollow Deuterium-Tritium fuel capsule is first compressed spherically by long pulse lasers. In a second step, short pulse lasers drive generate a proton beam from a partial sphere target. This beam is guided within a protecting cone, igniting the pre-compressed fuel.

paraments as well as the shape and structure of the target the ions are accelerated from.

When using partial sphere targets, one of the properties of TNSA is utilized to focus the proton beam: the protons are accelerated normal to the targets surface.

Figure 1.1 depicts a schematic of the process of proton fast ignition, showing the partial sphere target along a collimated proton beam generated from it towards the pre compressed fuel. The truncated cone both protects the interior from the compression beam and helps to guide protons via self-generated electrostatic and magnetic fields towards the central part of the implosion.

Past studies (T. J. Bartal, 2012; S. N. Chen et al., 2012; Kaymak et al., 2019; McGuffey et al., 2020; Offermann et al., 2011; Qiao et al., 2013; Snavely et al., 2007) , researching the focussing of TNSA protons and similar topics, have been comparing very few target configurations, with only tens of shots, often less, limited by the number of available shots on the laser system used. This massively limits the statistical evaluation of the data generated and does not allow for the exploration of various target or laser parameters.

To overcome these limitations, newer, high shot rate facilities as L-Aleph (Wang et al., 2017) , ELI (Gales et al., 2018) or BELLA (Leemans et al., 2014) , now provide medium repetition rates ($\sim$ 1 Hz), allowing for a wider parameter space to be explored. This further results in exciting new opportunities and allows for a statistical evaluation of the data. For past campaigns, partial sphere targets were produced by electroplating single steel balls, laser cutting the sphere and manually assembling the target onto a carrier. This procedure allows for the fabrication of few, high quality targets, which met the demand on low repetition rate systems. High intensity medium repetition rate laser ($\sim$ 1 Hz) facilities, allow large-scale parametric studies crucial for PFI development. However, translating these advanced facilities into practical experiments demands equally advanced approaches to target manufacturing and alignment.

Challenges that arise with the processing of hundreds of targets are plentiful. For the data to be comparable all targets need to be similar and well characterized. The fabrication needs be scaleable, fast and standardized.

Relying on individual metrology for target alignment and quality control requires an automated approach. Furthermore, the alignment needs to be fast, automatic and robust, to allow for a continous operation of the system.

This work outlines the fabrication of batches of partial sphere targets with a diameter of 525 µm, 325 µm and 220 µm, at the time of writing the smallest used in any experimental campaign. Where typically only tens of partial spheres where manufactured, now more than a thousand partial sphere targets have been build and mapped, setting a new benchmark for the fabrication and metrology of complex targets.

To allow for the deployment of the targets, a new alignment procedure has been developed, consisting of a two step approach: a automated pre alignment of sets with 200 targets along four integrated alignment features prior their experimental deployment, followed by a reduced alignment in the experimental chamber, utilizing only the alignment features, greatly reducing the turn-around time between sets, while maintaining high precision alignment.

The fabrication of the amount of partial sphere targets and the development of the alignment procedure was essential for an experimental campaign at the L-ALEPH laser system at the Colorado State University. The experimental campaign provided a systematic study of the beam focusing of TNSA protons from partial sphere targets allowing for future refinement of the ignition scheme. In addition, the developments in target fabrication, metrology and alignment, served to advance proton fast ignition research in future campaigns. This thesis aims to bridge the gap between conceptual target designs and large-scale production needed for advanced PFI studies at medium repetition rate laser systems.

Structure of the Thesis: Chapter 2 provides an brief introduction into the fundamentals of laser plasma interaction that lead to Target Normal Sheath Acceleration, with a detailed discussion of proton focusing by shaped targets given in Section 5.2.

Chapter 3, Section 3.1 presents the application of Radiochromic Film alongside meshes to provide information about protons trajectory. A confocal microscope has been used for the mapping and diagnostic of the targets alongside ISO 25178[2] for standardized documentation, both explained in Section 3.3. This is followed by a brief introduction into electroplating, a process used during fabrication, in Section 3.4.

The main focus of this thesis, the fabrication and alignment of the targets is elaborated in Chapter 4, with Section 4.1 covering a detailed design description, followed by the fabrication procedure in Section 4.2 and evaluation of the finished targets in Section 4.3. Chapter 4 closes with the alignment concept and evaluation in Section 4.4.

The final Chapter 5 covers the setup of the experiment conducted in Section 5.1 and is followed by a discussion of the focusing dynamics of spherical targets, utilizing Particle In Cell (PIC) simulations in Section 5.2. An experimental evaluation, followed by a comparison with the simulations, appears in Section 5.3.

---

[2] ("Geometrical product specifications (GPS) – Surface texture: Areal – Part 2: Terms, definitions and surface texture parameters", 2023; "Geometrical product specifications (GPS) – Surface texture: Areal – Part 3: Specification operators", 2012)

2 Laser Plasma Interactions

Before an ultra-intense laser pulse interacts with a solid target a pedestal or pre-pulse precedes the main pulse by nano to picoseconds. Both usually are of high enough intensity to partially ionize the target surface, resulting in an expanding plasma plume. As a consequence, the most intense main pulse interacts not with a solid, but a pre formed plasma. The next Sections cover the fundamental ionization mechanisms resulting in plasma formation, followed by an overview of basic plasma properties. Next the electron acceleration and heating mechanisms relevant for target normal sheath acceleration are discussed, which is the mechanism relevant for the experiment presented in this work.

2.1 Ionization and Plasma Generation

Though most of the discussion in this chapter revolves around the interaction of intense light with matter in the state of plasma, the initial interaction is one including a solid target. The initial ionization process at the targets surface strongly depend on the current laser intensity and photon energy. Even though the actual process of ionization is not of importance for the acceleration process discussed in Section 2.5, the intensity at which it occurs, is.

One can start with an initial estimation by calculating the field strength of an electron bound to the hydrogen atom (Gibbon, 2016). At the Bohr radius of $a_B = \hbar/me^2 = 5.3 \times 10^{-9}$ cm the electric field strength is given by

$$E_a = \frac{e}{4\pi\epsilon_0 a_B^2} \approx 5.1 \times 10^9\,\mathrm{V\,m^{-1}} \tag{2.1}$$

The corresponding laser intensity is

$$I_a = \frac{\epsilon_0 c}{2} E_a^2 \approx 3.5 \times 10^{16}\,\mathrm{W\,cm^{-2}} \tag{2.2}$$

and is called the *atomic intensity* (Batani et al., 2001; Gibbon, 2005). Once the laser surpasses this intensity any material will be ionized. This is already several orders of magnitude less than the intensity of the laser used in this thesis, but ionization of the target can occur even at magnitudes lower than I_a.

Multiphoton Ionization

Multiphoton ionization happens when an electron bound to a nucleus absorbs enough photons within a sufficiently short period of time ($\approx 1 \times 10^{-15}$ s) for it to overcome the ionization threshold. For photons exciting an electron into an intermediate state this temporal threshold can be far larger ($> 1 \times 10^{-8}$ s). The required amount of photons depends both on the ionization energy of the given electron and the photon energy, with the kinetic energy of the freed electron given by

$$E_f = n\hbar\omega - E_{\text{ion}}, \tag{2.3}$$

with n photons absorbed (Batani et al., 2001; Gibbon, 2005), as illustrated in Figure 2.1 a). Besides the photon energy, this non linear process is strongly intensity dependent. The rate for an n-photon ionization is given by

$$\Gamma_n = \sigma_n I_L^n, \tag{2.4}$$

with the cross-section σ_n for the absorption of n photons, scaling with n. The I_L^n dependency ensures that n-photon ionization will occur given a high enough laser intensity.

Tunnel Ionization

The previous discussion is based on the ansatz that the binding potential remains unaffected by the electric field of the laser. This is no longer true if its intensity approaches the atomic intensity I_a (equ 2.2). At these moderate intensities the electric field of the laser distorts the Coulomb potential $V(x)$ of an atom (Gibbon, 2005). Once the potential barrier becomes sufficiently thin, the probability for the electron to leave the potential via tunneling effect increases. Tunneling describes a quantum mechanical effect of particles passing through a potential, even though they lack the energy to 'overcome' the potential (Batani et al., 2001). This effect is visualized in Figure 2.1 b). A quasi static approach of the involved electric field was first described by Kelysh (Keldysh, 1964) who introduced the adiabatic parameter γ_K

$$\gamma_\mathrm{K} = \sqrt{I_p/2U_p} \tag{2.5}$$

with the undisturbed ionization potential I_p and the ponderomotive potential U_p. The latter, describing the averaged energy acquired by the fast oscillation of the electrons in an electromagnetic wave, is given by (Gibbon, 2005)

$$U_p = \frac{e^2 E_0^2}{4 m_e \omega^2}, \tag{2.6}$$

where E_0 is the amplitude of the laser's electric field. Tunneling dynamics become important for small γ_K or strong fields and long wavelengths, whereas multiphoton ionization becomes dominant for $\gamma_\mathrm{K} > 1$ (Batani et al., 2001). Assuming a classical picture of a stationary homogeneous electric field modifying a Coulomb potential,

$$V(r) = -\frac{Ze^2}{x} - eE_0 r, \tag{2.7}$$

with the nuclear charge state Z, one can estimate the intensity where the field of the laser sufficiently lowers the Coulomb barrier to a point where the electron can escape without tunneling, as seen in Figure 2.1 c). This process is called barrier suppression ionization (Kim, 2023), and the threshold intensity is approximately

$$I_{BS} \approx 4 \times 10^9 \left(\frac{E_\mathrm{ion}}{\mathrm{eV}}\right) Z^{-2}\,\mathrm{W\,cm^{-2}} \tag{2.8}$$

where E_ion is the ionization energy and Z is again the charge state of the nucleus after the electron departs.

For gold (A. Kramida et al., 2023) this value calculates to an intensity of $2.9 \times 10^{13}\,\mathrm{W\,cm^{-2}}$.

Impact ionization

Impact ionization is the process by which the incoming laser heats the target by accelerating free electrons. The accelerated electrons can further ionize bound electrons, if they have gained enough kinetic energy to do so. The resulting additional electrons further contribute to the heating and ionization of the target. Here the electrons only extract energy from the light wave upon impact with other particles. In contrast to the previously discussed multiphoton and tunnel ionization, this mechanism is a two step process requiring free electrons provided by other mechanisms. It is possible to first excite an electron to a higher state and then to

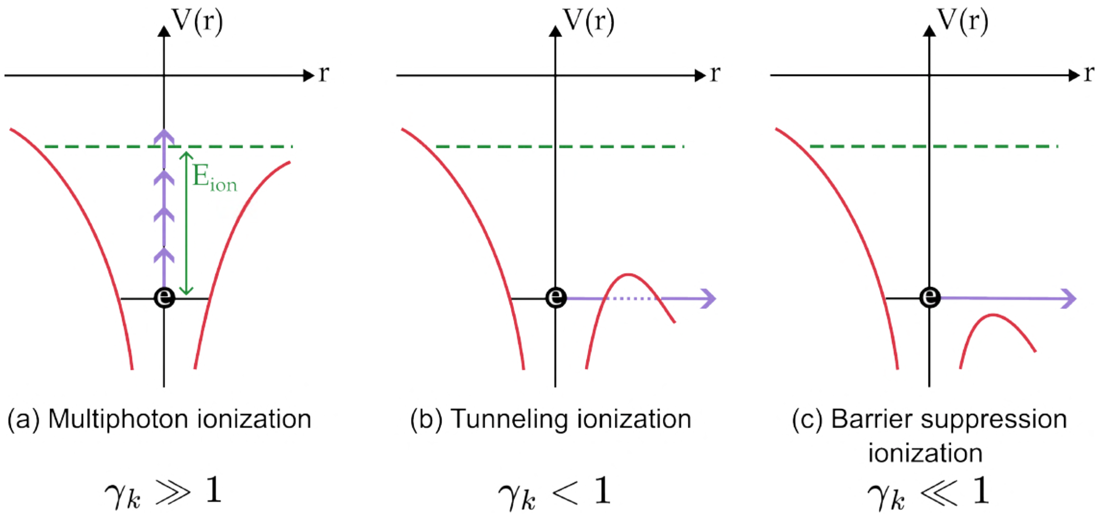

(a) Multiphoton ionization $\gamma_k \gg 1$
(b) Tunneling ionization $\gamma_k < 1$
(c) Barrier suppression ionization $\gamma_k \ll 1$

Figure 2.1: Image based on (Kim, 2023).

free the electron from the ion through a second collision. The amount of energy required is highly dependent on the material and the already existing charge state (C. S. Liu et al., 2020).

In the context of laser-matter interaction, impact ionization becomes significant, once a plasma has formed on the target's surface, because this provides free electrons capable of colliding with the neutral atoms, hence further ionizing the material (C. S. Liu et al., 2020).

To summarize, independently of the specific ionization mechanism involved, a pre-pulse with an intensity $I > 1 \times 10^9\,\mathrm{W\,cm^{-2}}$ is already sufficient to ionize the target surface and create an expanding plasma. Therefore, the main laser pulse interacts with this preformed plasma. In the next Section, the fundamental properties of a plasma are outlined to set a foundation for the discussion of the laser-plasma interaction.

2.2 Plasma Properties

Plasma is the fourth fundamental state of matter, constituting the majority of the visible matter in the universe. It is to varying degrees comprised of charged and neutral particles, which exhibit collective behavior. Macroscopically, a plasma is neutral as local charge variations are quickly screened by the surrounding charged particles. This screening is dependent on the plasma's temperature T_e as well as its electron density n_e. The Debye sphere determines the length where the potential of a point charge is below $1/e_\mathrm{E}$ of it's original value, with e_E as the Euler's number (Gibbon, 2016). The Debye length λ_D is given by

$$\lambda_\mathrm{D} = \sqrt{\frac{\epsilon_0 k_\mathrm{B} T_e}{n e^2}} \tag{2.9}$$

where ϵ_0 is the permittivity of vacuum, k_B is the Boltzmann's constant, T_e the electron temperature and e is the elementary charge(F. F. Chen, 2016).

Using the Debye length as the radius of a sphere, the amount of particles within can be calculated, resulting in the plasma parameter N_D (Piel, 2010)

$$N_\mathrm{D} = n \frac{3}{4} \pi \lambda_\mathrm{D}^3. \tag{2.10}$$

For a plasma to be considered quasi-neutral, the condition $N_\mathrm{D} \gg 1$ must hold, meaning that the number of particles within a Debye sphere should be sufficiently large.

Another fundamental quantity defining a plasma is the electron plasma frequency ω_p, describing the natural oscillation frequency of electrons in a plasma. When an electron is slightly displaced from its equilibrium position, for example by an electric field, the resulting opposing force arising from the charge separation leads to an oscillation around the resting position. The frequency of this oscillation is given by the plasma frequency w_p

$$\omega_\mathrm{p} = \sqrt{\frac{n_\mathrm{e} e^2}{\epsilon_0 m_\mathrm{e}}} \tag{2.11}$$

with m_e as the electron mass(Gibbon, 2016). This frequency is important, as it sets the fastest timescale for different processes in plasma and defines how the plasma reacts to electromagnetic fields, which is discussed in the following Sections. The response time, inversely proportional to the plasma frequency, effectively sets the time scale for the electrons to shield a local charge (Piel, 2010). In contrast to gases where the collisions of particles is the dominating behaviour, plasmas show ranged collective behaviour. Their dynamics are governed by the collective motion of particles interacting through long-ranged electromagnetic fields, rather than by direct particle-particle collisions (Gibbon, 2016).

When an electromagnetic wave travels through a plasma, its ability to propagate depends on the plasma frequency w_p and laser frequency ω. If $\omega_p > \omega$ the dispersion relation $\omega^2 = k^2c^2 + w_p^2$ requires an imaginary k-vector, therefore preventing wave propagation. The density at which $\omega = \omega_p$ is called critical density (Wilks & Kruer, 1997)

$$n_c = \frac{\omega \epsilon_0 m_e}{e^2} \approx 1.1 \times 10^{21}\,\mathrm{cm}^{-3} \left(\frac{\lambda}{\mu\mathrm{m}}\right)^{-2} \tag{2.12}$$

and marks the boundary between an underdense (transparent) and overdense (opaque) plasma (C. S. Liu et al., 2020). For a wavelength of $\lambda = 0.8\,\mu\mathrm{m}$ this corresponds to $n_c \approx 1.7 \times 10^{21}\,\mathrm{cm}^{-3}$. Whether the laser is partially transmitted, reflected or absorbed depends on the local electron density n_e and how it compares to n_c. Therefore the boundary plays a crucial role in the absorption of laser energy into the plasma, for example by resonance absorption, Brunel- and $\mathbf{J} \times \mathbf{B}$ heating.

2.3 Single Electron Motion in an Electric Field

Although the previous Section emphasised the collective behaviour of plasmas, it is necessary to discuss the motion of a single electron within a varying electromagnetic field. This Section derives the concept of the quiver motion of an electron in an oscillating field and explains how gradients in the field give rise to the ponderomotive force, based on the description of Piel (Piel, 2010). These concepts provide a foundation to understand the mechanisms at play for the interaction of high intensity laser pulses with plasma.

The motion of an electron in an electromagnetic field is described by the Lorentz force

$$m\ddot{\mathbf{x}} = -e[\mathbf{E} + \mathbf{v} \times \mathbf{B}] \tag{2.13}$$

where **E** and **B** represent the electric and magnetic fields. Assuming non relativistic electron motion, $v_\mathrm{e} \ll c$ the second term of the equation can be neglected and the movement is governed by the electric field only. This results in an equation of motion

$$\ddot{x} = \frac{e}{m} E(x) \cos(wt) \tag{2.14}$$

with the amplitude of the electric field changing along x. This differential equation requires an evaluation of the instantaneous position x(t) of the electron, where an analytic solution is possible by expanding the problem into a Taylor series:

$$E(x) = E(x_0) + x_1(t)\frac{\mathrm{d}}{\mathrm{d}x}E(x_0) + ... \tag{2.15}$$

The first order solution describes the motion of an electron in a plane electric wave. In this case the motion follows the the oscillating field

$$x_1(t) = -\frac{e}{m\omega^2}E(x_0)cos(\omega t) \tag{2.16}$$

with an amplitude given by the quiver velocity v_{osc}:

$$v_{osc} = \frac{eE(x_0)}{m\omega}. \tag{2.17}$$

The second order term of equation 2.15 results in

$$\ddot{x}_2 = \frac{e}{m}x_1(t)\frac{\mathrm{d}}{\mathrm{d}x}E(x_0) = -\frac{e^2}{m^2\omega^2}E(x_0)\frac{\mathrm{d}}{\mathrm{d}x}E(x_0)cos^2(\omega t). \tag{2.18}$$

Here the electron experiences a fast oscillation with 2ω, as $\cos(\omega)^2 = 0.5(1 - \sin(2\omega))$ which can be averaged, by using $\langle\cos^2\rangle = 1/2$

$$\langle\ddot{x}_2\rangle = -\frac{e^2}{4m^2\omega^2}\frac{\mathrm{d}}{\mathrm{d}x}\left[E^2(x_0)\right] \tag{2.19}$$

This describes a force pushing charged particles away from areas of high field strength

$$\langle F_{\mathrm{P}}\rangle = -\frac{e^2}{4m\omega^2}\frac{\mathrm{d}}{\mathrm{d}x}\left[E^2(x_0)\right]. \tag{2.20}$$

This Force is called the *ponderomotive force* and is relevant for the motion of electrons in high intensity, short pulse laser fields, which offer a high gradient of the electric fields strength. This results in an effective acceleration and relocation of the electrons in the laser generated plasma, as the lighter electrons experience a much stronger force than the heavier ions. Visually, the electron oscillates with its quiver velocity while drifting away towards lower electric field strength (Michel, 2023).

Making use of the quiver velocity v_{osc}, equation 2.17, a dimensionless electric field amplitude can be defined:

$$a_0 := \frac{v_{osc}}{c} = \frac{eE}{m_e\omega c}. \tag{2.21}$$

The previous non relativistic ($a_0 < 1$) assumptions no longer holds true at the intensities of Laser-driven acceleration and relativistic corrections as well as the second term of equation 2.13 has to be taken into account. Under such conditions, the equation of motion can not as easily be solved in the presence of non-linear mechanisms contributing to the acceleration of electrons in a Laser-driven plasma.

2.4 Laser Absorption Processes and Energy Transfer in Overdense Plasmas

As already discussed, a pre-pulse or a pedestal with an intensity $I > 10 \times 10^9\,\mathrm{W\,cm^{-2}}$ preceding the main pulse, is already able to (partially) ionize the target material (M. Schollmeier et al., 2007). As a consequence of this, the high intensity laser pulse interacts with a plasma layer partially below the critical density n_c, expanding into the vacuum at the sound speed (Gibbon, 2005)

$$c_s = \sqrt{\frac{Z * k_B T_e}{m_i}} \tag{2.22}$$

with the Boltzmann constant k_B, the electron temperature T_e and ion mass m_i. In the assumption of an isothermal expansion, it can be shown that the density profile is exponentially decreasing (Kruer, 1988) with a scale length of

$$L_p = c_s \tau_L. \tag{2.23}$$

for a given laser pulse duration τ_L. This scale length can be expected to be $L/\lambda \approx 0.01 - 0.1$ for the 40 fs laser used in the experimental conditions.

In an overdense regime the laser can not pass through the plasma, but can still penetrate into the overdense region up to a characteristic skin depth $l_s = c/\omega_p$ (Gibbon, 2016).
For femto- and picosecond pulses at intensities above $I \gtrsim 1 \times 10^{15}$ W cm^{-2} various collisionless mechanisms dominate over collisional absorption (Gibbon, 2005). The scale length L_p, which is dependent on the target material as well as the shape of the pre-pulse, further determines the importance of the different mechanisms.

During **collisional absorption**, electrons gain energy from the laser and depose it in collisions with ions, therefore damping the laser electromagnetic wave and heating the plasma. This process is also called inverse Bremsstrahlung and is most effective for low intensities, high Z materials and at high densities (C. S. Liu et al., 2020; Gibbon, 2005; Wilks & Kruer, 1997).

The expanding plasma at the target front offers a density gradient. When this gradient is long compared to the laser wavelength ($L_p/\lambda \gg 1$), **resonance absorption** becomes important. In this case, the laser pulse arrives obliquely incident and with p-polarization[1]. The laser propagates through the underdense plasma until it reaches the critical density n_c. Here, a resonant coupling between the laser's electric field and an electrostatic plasma wave, leads to an energy transfer of the laser to the electrons. This process is ineffective in steep density gradients or at relativistic intensities, where non linear effects dominate.

For ultra-short and high-intensity lasers, the plasma has a steep density gradient with a short scale length ($L_P/\lambda \ll 1$) (Gibbon & Bell, 1992). Under these conditions, the **Brunel effect**, also known as vacuum heating, dominates (Brunel, 1987). Unlike resonant absorption, which depends on wave-plasma coupling near the critical density, the Brunel mechanism does not require a plasma wave. Instead, with a p-polarized laser at an oblique incidence (optimal at $\sim 45°$), the electric field of the laser pulls electrons out into the vacuum with each cycle and drives them back into the overdense region, where the laser is unable to penetrate. This process efficiently transfers energy from the electric field to the electrons, with absorption efficiencies reported to $30\,\%$ to $60\,\%$ (Michel, 2023; Wilks & Kruer, 1997). As a result, a substantial amount of hot electron is generated by this mechanism, which therefore plays an important role in processes like laser-driven ion acceleration (Gibbon & Bell, 1992).

Similar to Brunel heating, $\mathbf{J} \times \mathbf{B}$ heating accelerates electrons at a steep density gradient. With intensities above $\gtrsim 1 \times 10^{18}$ W cm^{-2}, electrons reach relativistic velocities during a single laser cycle. Under these conditions, the previously with equation 2.19 assumed approximation of the ponderomotive force is no longer valid and the oscillating factor at 2ω can no longer be neglected. In overcritical plasmas, the ponderomotive force results in a significant ionization and particle displacement, effectively modifying the plasma's response and enhancing the absorption of laser energy. The ponderomeotive force pushes electrons at the critical density into the plasma, which are then pulled back into the vacuum by the charge separation created by the quasistatic ions. Highly accelerated electrons are injected into the target as a result of this back an forth motion at twice the laser frequency as a result of this process.

To summarize, the collisionless absorption mechanisms, Brunel- and $\mathbf{J} \times \mathbf{B}$ heating, provide the driving force of hot electron populations at the targets front, as the scale length is short $L_p < \lambda$. These electrons

---

[1] p-polarization: The electric field has a component normal to the surface.

traverse the target and can establish a large electrostatic field at the rear surface, which in turn accelerates ions to several MeV (Macchi et al., 2013). This process, called target normal sheath acceleration is subject of the following Section.

2.5 Target Normal Sheath Acceleration

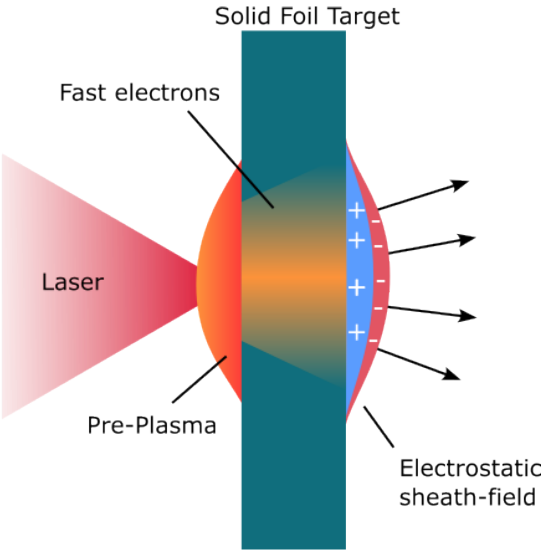

Figure 2.2: Simplified sketch of a laser-irradiated foil target. The electrons are heated in the plasma at the front surface and traverse through the target, forming an electrostatic sheath, accelerating the protons. Based on (Higginson, 2018).

Laser-driven acceleration has received significant attention in the last decades due to its potential applications in various fields, such as proton therapy, nuclear physics and, but not limited to, inertial confinement fusion. Among various laser-based ion acceleration mechanisms, Target Normal Sheath Acceleration (TNSA) has been extensively studied and is considered a robust and straightforward mechanism to achieve energetic ions. Beams generated by TNSA are characterized by a high number of ions ($> 10^{13}$) (Roth et al., 2002; Snavely et al., 2000) directed forward at a low emittance (Cowan et al., 2004), with a duration similar to the duration of the laser (on the order of picoseconds or less) (Macchi et al., 2013; M. S. Schollmeier, 2009; Snavely et al., 2000).

With laser pulses reaching intensities of $10^{18}\,\mathrm{W\,cm^{-2}}$ and beyond the first experiments generating high energy (MeV) ions were possible. Early experiments (Hatchett et al., 2000; Snavely et al., 2000) established that when a high intensity laser interacts with a solid target, a large number of hot electrons are generated and move through the target, resulting in a strong electric field at the rear surface capable of accelerating ions of the target.

The work of Wilks et al. (Wilks et al., 1992, 2001) and Snavely et al. (Snavely et al., 2000) placed the initial foundation for the understanding of TNSA.

As previously mentioned, at laser intensities beyond $10^{19}\,\mathrm{W\,cm^{-2}}$ the laser is not only strong enough to instantly ionize the matter, but also its pre-pulse and pedestal are. The main laser pulse, therefore, interacts with an expanding plasma. The different heating mechanisms described in the previous Section will heat part of the electrons to energies of several MeV.

These hot electrons will traverse the target at a low opening angle of less than 16° for thin ($< 10\,\mu\mathrm{m}$)

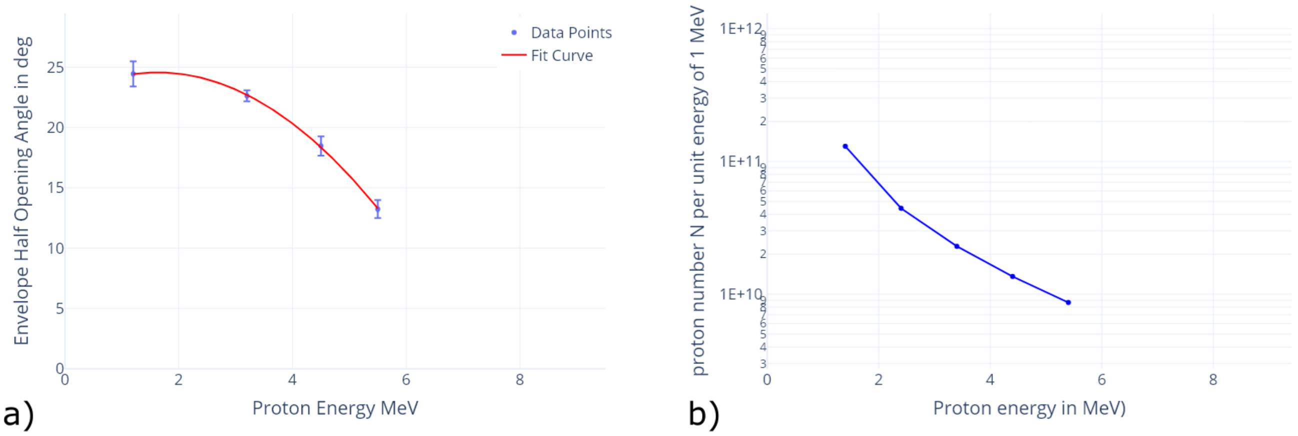

Figure 2.3: a) Proton count per energy bin. b) Half opening angle of the beam envelope per energy bin. Measurements taken from a shot on a $10\,\mu\mathrm{m}$ gold foil.

targets, where collisional scattering can be neglected (M. S. Schollmeier, 2009). Once the electrons reach the rear surface, a strong ($>$ TV m^{-1}) electric sheath field with a thickness in the order of micrometers is formed due to the charge separation introduced by the hot electrons escaping against the inert ions. This field is strong enough to instantly field-ionize the atoms present and can be considered quasi-static, resulting in an acceleration of ions from the rear surface. These accelerated ions are mostly protons, present as contamination from water or hydrocarbons on the targets rear surface, if no special measures, like heating of the target (McKenna et al., 2004), are taken (Cowan et al., 2004; Roth et al., 2002; Snavely et al., 2000). The resulting ion beam has a broad energy distribution of roughly exponential shape with a large amount of low energy ions extending to a cut off energy, highly dependent on laser and target conditions. An example from the experiment conducted during this thesis is shown in Figure 2.3 a). Additionally, the energy dependence of the opening angle is depicted in Figure 2.3 b).

Both of these effects are a result of the shape of the initial hot electron sheath shape, as shown by Carroll et al. (Carroll et al., 2007), whom base their conclusions on Fuchs et al. (Fuchs et al., 2003), who showed that the protons follow the density curves of the sheath field. For targets made from conducting material, this sheath field initially follows the imprint of the laser, usually a Gaussian shape (Fuchs et al., 2003; Romagnani et al., 2005), as sketched in Figure 2.2.

The opening angle decreases with energy (Brambrink et al., 2006; Cowan et al., 2004; Snavely et al., 2000) due to the decrease of the size of the emission region for higher energies (Borghesi et al., 2006; Cowan et al., 2004; Roth & Schollmeier, 2016).

As there is a direct correlation between the spatial laser profile the shape of the resulting sheath and the source size of the higher energy protons, a highly focused laser pulse will result in a beam with a higher divergence. On the other hand, if a low divergence beam is desired, a flat top laser pulse is preferred (Roth & Schollmeier, 2016).

For applications like proton driven fast ignition (Roth et al., 2001) and heating warm dense matter (Pelka et al., 2010) a focused proton beam is required and was first experimentally generated utilizing a curved target by Roth (Roth et al., 2002). In cases like these, the accelerating field is superimposed by the shape of the target, resulting in a, in first approximation, ballistically focused beam.

A more detailed discussion on the focusing properties of different sizes of spherical targets alongside simulations for the geometries used in the experimental campaign can be found in Section 5.2.

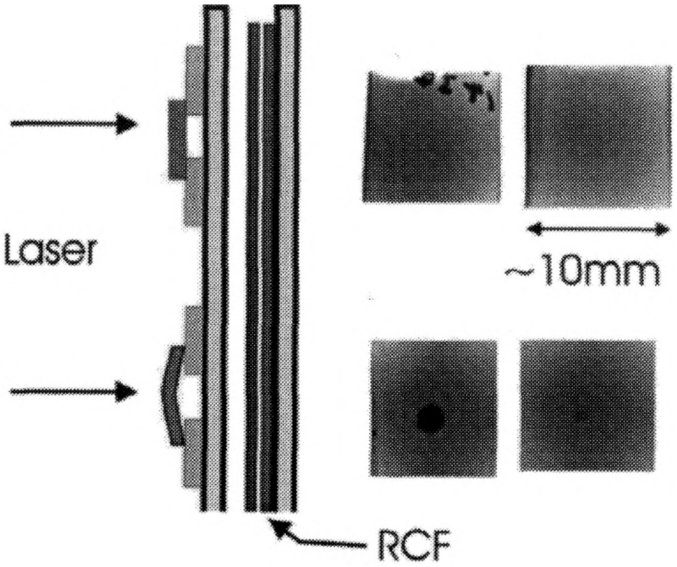

Figure 2.4: Experimental setup for a flat and a $\varnothing 2.5\,\mathrm{mm}$ curved target, irradiated by a laser. The images resulting from the shielded RCF show a focussing of the proton beam (Roth et al., 2002).

3 Methodology

In this chapter, the diagnostic and metrology techniques used to characterize the targets themselves, as well as the laser-driven proton beams generated from them, are presented.

Section 3.1 introduces the concept of radiochromic film (RCF) dosimetry. RCF stacks were used to record the time integrated spatial and energy distribution of the proton beams. Due to the laminarity of the beam, meshes placed between the film and the target can be utilized to gain information about the beam's trajectory. The necessary concepts are introduced here and later utilized in Section 5.3.

In Section 3.2, the XUV diagnostic is described. This imaging system records the thermal emission at $\sim 92\,\mathrm{eV}$, providing a spatially resolved measurement of the surface temperatures of secondary foils heated by the proton beam. By comparing the measured signal intensities with radiation hydrodynamic models, the temperature of the sample can be estimated, thereby complementing the proton beam diagnostics obtained with the RCF stack.

Subsequently, Section 3.3 starts by introducing the concept of confocal microscopy. This is followed by a description of the terminology and standards (ISO 25178) relevant to the analysis of 3D areal surface texture. This sets the foundation for the evaluation of their quality later in Section 4.3.

Finally, Section 3.4 outlines the specific electroplating procedure used to create the three dimensional gold targets studied in this thesis. Specifically, the process for depositing a $10\,\mu\mathrm{m}$ gold layer onto polymer templates.

3.1 Radiochromic Film

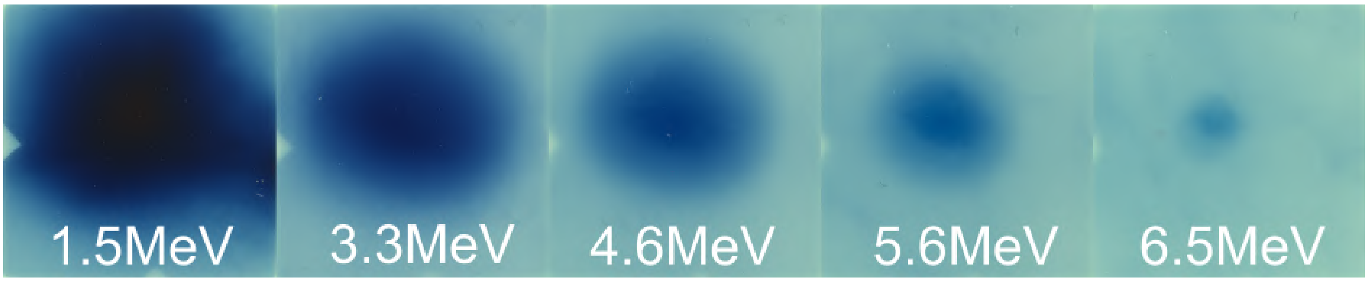

Figure 3.1: RCF layers of the corresponding proton energy. Shot with $19.3\,\mathrm{J}$ on a $\varnothing 525\,\mu\mathrm{m}$ spherical target.

In radiation dosimetry, the change of specific material properties by incoming radiation is used to record the absorbed dose. One passive detector [1] , commonly used in high-energy physics, are stacks of Radiochromic Films (RCFs). They provide a high spatial resolution, can be adapted to different dose and energy ranges and allow for a measurement over a large area. Used for measurements of accelerated ions, they provide information about the spatial and energetic distribution, as well as the fluence (McLaughlin et al., 1991).

The RCFs used in the experiments of this thesis are Gafchromic®HD-V2 commercially sold by Ashland (Ashland, 2021) and consist of an active layer of $12\,\mu\mathrm{m}$ thickness and a supporting polyester layer of $97\,\mu\mathrm{m}$,

---

[1] Passive refers to a detector, that integrates the dose during its use and provides results in a separate readout phase.

as depicted in Figure 3.2. HD-V2 films are sensitive in a range of 10 Gy to 1000 Gy. Other films, like the Gafchromic®EBT3, can include an additional polyester layer making them sensitive in a different dose range.

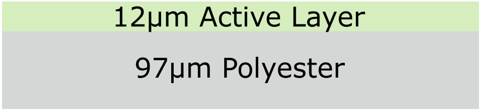

Figure 3.2: Composition of a Gafchromic®HD-V2 (Ashland, 2021) radiochromic film.

The active layer of an RCF undergoes a chemical reaction when exposed to ionizing radiation, causing a change in the optical density (OD) related to the absorbed dose (S. N. Chen et al., 2016). To obtain this relationship RCFs can be calibrated by exposing them to a precisely known dose and measuring the OD. This can be done using synchrotron or cyclotron radiation as shown by (Hicks et al., 2013). Figure 3.3 shows such a calibration curve, with the film digitized using a calibrated scanner. The red channel is fully opaque at a dose of approximately 300 Gy whereas the blue channel is changing its transparency up to a dose of 150 kGy. Considering the sum of the channels the film provides a high dynamic range.

When these fast charged particles pass through matter they deposit part of their energy along their path by interacting with the material, resulting in the previously mentioned reaction in the RCF. The rate of energy deposition or dose increases as the particle slows down due to an increase in the cross section of the involved physical processes (Wilson, 1946). These processes collectively result in a sharp rise in the deposited energy at the end of the particles path, known as the Bragg peak.

To make use of this effect, RCFs are typically used as a stack. Here each layer serves as an individual dosimeter, recording the deposited energy at different depths. Each layer of the RCF is associated with a specific energy range, used to recreate the energy spectrum of the initial beam.

This allows for the reconstruction of the energy distribution using simulations providing the correlation between deposited energy in the layer and the initial particle energy (Schmitz et al., 2024).

Figure 3.4 shows the deposited energy per proton energy for each active RCF layer in a stack consisting of 5 HD-v2 RCFs and an aluminium foil in front. By changing the composition of the stack its energy range and sensitivity can be adapted to the expected characteristics of the beam. For example, thin aluminum foils can be used in front of the stack to filter electrons and attenuate heavier ions, to protect the RCF from laser light and debris, as well as to shift the entire spectrum. Furthermore, additional foils in between the active layers, and different film types (e.g., HD-V2, EBT3) can be selected to adjust the stacks sensitivity to a specific energy range or particle flux. Figure 3.4 shows the spectrum of a stack with a 12.5 µm foil in front alongside a 20 µm foil. The shift in the spectrum towards higher energies for the thicker foil is visible.

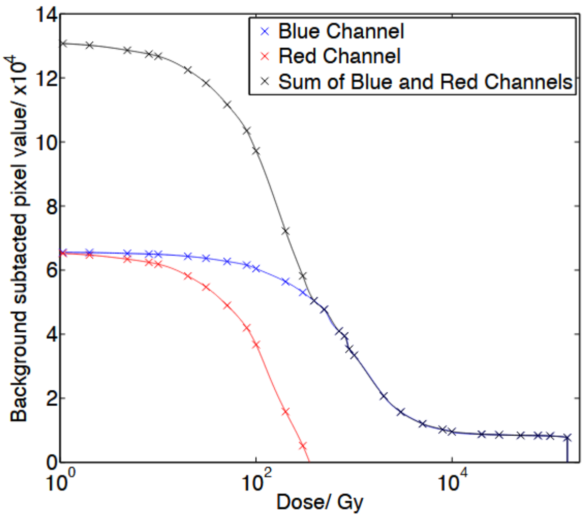

Figure 3.3: Color values for the three color channels corresponding to their dose. calibraition for a HD-v2 film. Higher doses result in less transmitted light. Image from Hicks et. al. (Hicks et al., 2013).

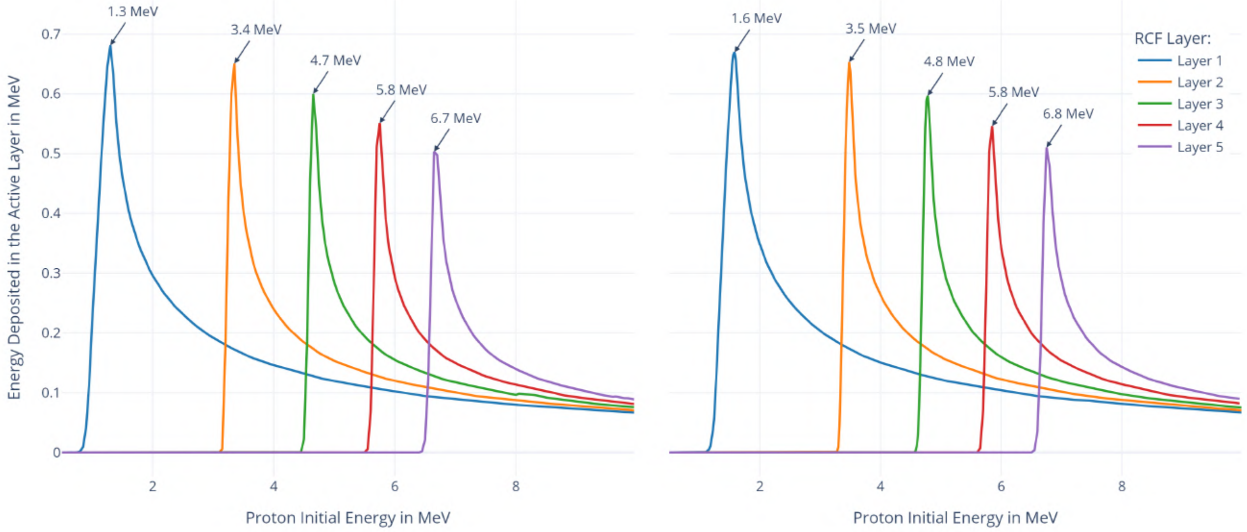

Figure 3.4: Energy deposited in each RCF layer of a HD-V2 stack with a $12.5\,\mu\mathrm{m}$ (left) or $20\,\mu\mathrm{m}$ (right) aluminium foil in front. The protons that deposit the most energy in a given layer are of higher energy for a thicker foil in front of the stack. Particles with less than the energy at the beginning of each trace do not reach that layer.

3.1.1 Application

The RCF stack used in the experiments consistend of 5 HD-v2 layers, wrapped by either 20 µm or 12 µm aluminium foil. This configuration was chosen due to the modest energy cut-off of the ALEPH-L of less than 8 MeV when using the f/25 parabola. To diagnose multiple shots, a large RCF stack (≈ 100 mm × 150 mm), is mounted in a frame featuring a grid of 5×4, 20 mm square openings as depicted in Figure 3.5. Mounted on stages, an unused square can be positioned prior every shot and its distance to the target adjusted, therefore providing the diagnostic for 20 shots in a single frame. To complete the setup, a shield, made from 5 mm Aluminium and 2 mm Copper, featuring a square opening is placed between the stack and the targets and prevents stray ions from depositing energy onto another position than the intended section.

Based on the simulations described in Section 5.2, conducted prior the experiment, the RCF Stack has been placed at a distance of 20 mm relative to the primary target.

For the previously discussed reconstruction of the initial proton beam energies and spatial distribution the tool for the ”Automated Reconstruction of the Initial Distribution of Laser Accelerated Ion Beams from Radiochromic Film (RCF) Stacks” by Benedikt Schmitz et al. (Schmitz et al., 2024) has been utilized. This Python-based algorithm uses different image processing techniques to separate the ion signal from parasitic signals generated by gamma rays or electrons.

For this experiment it has been used to efficiently and reproducibly evaluate 490 RCF scans resulting from 98 shots. An example energy distribution a proton beam generated from a ∅325 µm spherical target is shown in Figure 3.6 alongside the envelope half opening angle.

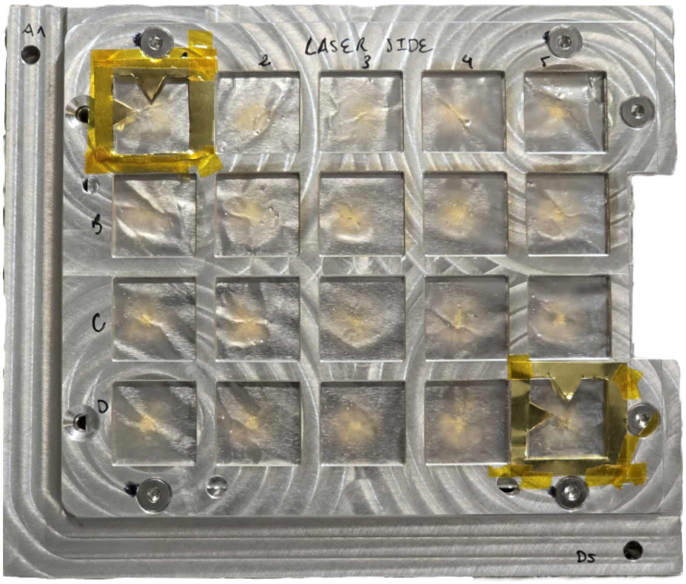

Figure 3.5: RCF stack mounted in a frame to separate it into multiple smaller segments. Aluminum foil in front to shield the RCF from electrons and debris. Alignment notches (top left and bottom right) placed as a redundant alignment tool for the RCF layers for post processing. A deposition of gold debris is visible at the center of each square.

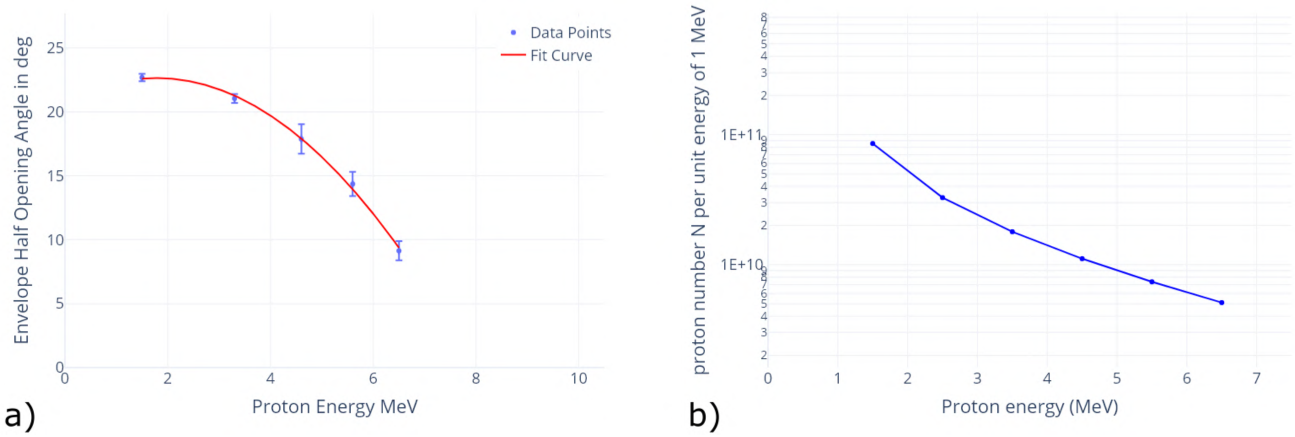

Figure 3.6: a) Proton count per energy bin. b) Half opening angle of the beam envelope per energy bin. Measurements taken from a shot with $19.2\,\mathrm{J}$ on a $\varnothing 325\,\mu\mathrm{m}$ target.

3.1.2 Mesh Magnification and Ray-tracing

To better understand the spatial characteristics of laser driven proton beams from spherical targets and compare different primary target diameters, the virtual focus position and size of the proton beam can be determined. The virtual focus is an *apparent point source* from which the protons seem to originate, when assuming ballistic path (straight-line) trajectories. This subsection describes the method of mesh magnification and ray-tracing to characterize the proton beams, with the corresponding experimental evaluation discussed in Section 5.3.

Imprinting the shadow of a thin object onto a proton beam and has been used in several experiments by placing grids (T. Bartal et al., 2012; Borghesi et al., 2002, 2004; Romagnani et al., 2005), lines (Kar et al., 2004) or other shapes (T. Bartal et al., 2011) into the beam's path, and then detecting the resulting pattern using radiochromic film. Even though the object placed in the beam is thin enough to neglect collision stopping, its divergence is increased due to multiple small-angle scattering interactions resulting in an effective local attenuation of the proton beam (D West & A . C. Sherwood, 1972).

A basic experimental setup using a flat foil is illustrated in Figure 3.7, showing a laser generated proton beam passing through a thin mesh and into the RCF stack. In the experiment copper meshes with a grid spacing of $42.3\,\mu\text{m}$ (600lpi[2]) and $63.5\,\mu\text{m}$(400lpi) were used.

For meshes closer to the source the magnification increases and the proton beam covers fewer grid lines. To counteract this and to provide a sufficient amount of grid lines to measure from, the higher grid spacing of $42.3\,\mu\text{m}$ (600lpi) is used for distances below $450\,\mu\text{m}$. This effect can be seen in Figure 3.8, where an imprint on the RCF with a mesh placed at $(646 \pm 25)\,\mu\text{m}$ and $(966 \pm 25)\,\mu\text{m}$ behind the apex of a $\varnothing 325\,\mu\text{m}$ spherical target is depicted, with the latter showing a wider grid spacing. The RCF layer depicted corresponds to a proton energy of $4.5\,\text{MeV}$.

The clear mesh pattern observed in Figure 3.8 indicates a laminar flow of the protons, similar to the image expected from protons emitted by a point source. To determine the position of this virtual source, the mesh magnification technique based on the averaged grid period measured from the image on the RCF is deployed, first established by M. Borghesi et al. (Borghesi et al., 2004).

The magnification M is calculated using the average grid spacing measured on the RCF g_{RCF} and the known grid spacing of the mesh g_{mesh}:

$$M = \frac{g_{RCF}}{g_{mesh}} \tag{3.1}$$

To obtain the RCF grid spacing g_{RCF}, the distance between neighboring grid points is measured and averaged. The uncertainty Δg_{RCF} is determined from the standard deviation of these measurements.

The resulting virtual focus position z_{focus} based on the mesh magnification requires knowledge of the position of the mesh and the RCF and assumes a purely ballistic trajectory of the protons:

$$z_{focus} = z_{mesh} - \frac{g_{mesh} \cdot (z_{RCF} - z_{mesh})}{g_{RCF} - g_{mesh}} \tag{3.2}$$

With the positions z_{mesh} and z_{RCF} and the proton emitting side of the target at $z_{apex} = 0$. The uncertainty in the mesh position Δz_{mesh} relative to the primary target originates from measurements of the targets following their manufacturing (see Section 4.3.2). Meanwhile, the nominal mesh grid spacing g_{mesh} is assumed to be exactly $63.5\,\mu\text{m}$ (400lpi) or $42.3\,\mu\text{m}$ (600lpi). However, the imprint on the RCF can deviate from this ideal spacing, leading to a grid spacing uncertainty Δg_{RCF}. This deviation is determined from the standard

---

[2] lines per inch

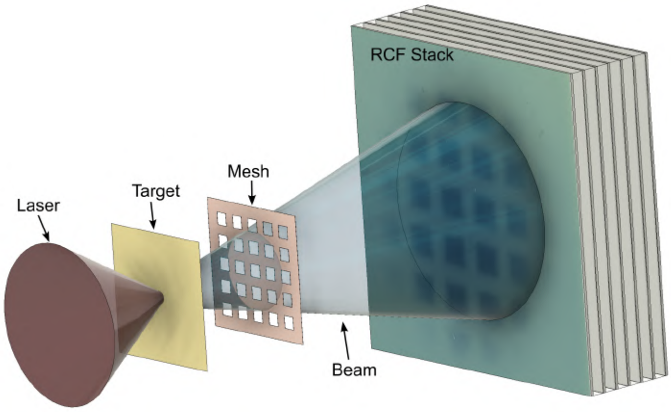

Figure 3.7: Schematic of the experimental setup showing the proton beam passing through a mesh and onto a RCF stack.

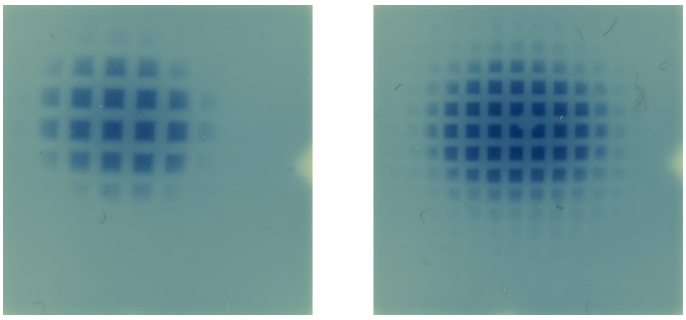

Figure 3.8: The RCF layer corresponding to a proton energy of $4.6\,\mathrm{MeV}$ for two different shots. Both on a $\varnothing 325\,\mu\mathrm{m}$ spherical target, but with a mesh (400 lpi) placed at $648\,\mu\mathrm{m}$ (left) and $958\,\mu\mathrm{m}$ behind the apex. The higher magnification for the mesh closer to the apex is clearly visible. For meshes even closer to the apex a finer mesh (600 lpi) is needed.

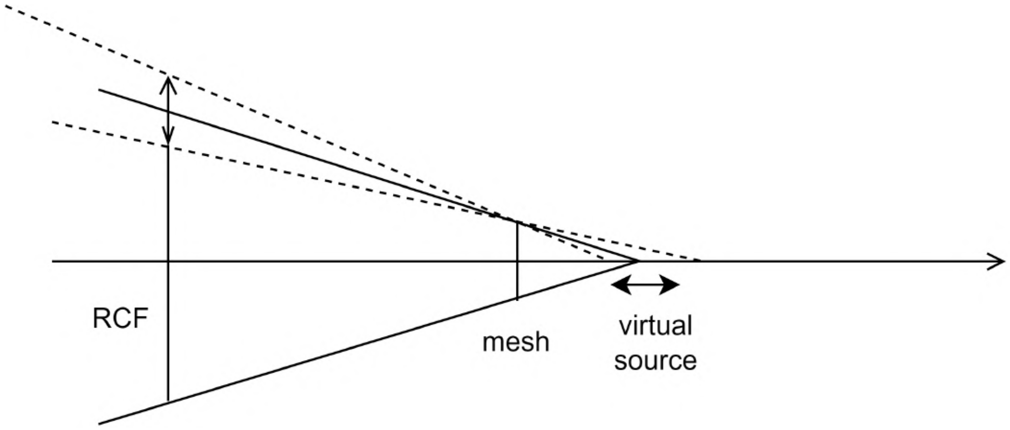

Figure 3.9: Sketch of the arrangement of the RCF and Mesh for the calculation of the mesh magnifiaction. An error in the grid spacing g_{RCF} results in a large error in the position of the virtual source z_{focus} due to the low gradient of the hypotenuse.

deviation of measured grid points, accounting for both potential non-uniformities in the physical mesh and the measurement accuracy of each point.

Among all uncertainty contributions in determining the virtual focus position z_{focus}, Δg_{RCF} is the dominant term. The overall uncertainty in z_{focus}, denoted Δz_{focus}, can be estimated via standard error propagation:

$$\Delta z_{focus}^2 = \left(\frac{\partial z_{focus}}{\partial g_{RCF}} \Delta g_{RCF}\right)^2 + \left(\frac{\partial z_{focus}}{\partial z_{mesh}} \Delta z_{mesh}\right)^2 + \left(\frac{\partial z_{focus}}{\partial z_{RCF}} \Delta z_{RCF}\right)^2 . \tag{3.3}$$

Across the evaluated targets, the first term typically contributes on the order of $10\,\mu\text{m}$ to $90\,\mu\text{m}$, whereas the other terms remain below $1\,\mu\text{m}$. Figure 3.9 provides a visual explanation for why the RCF grid spacing Δg_{RCF} most strongly affects z_{focus}.

As an alternative approach, a ray tracing method can be used to calculate the virtual focus position. By correlating the image mesh intersection points of the RCF to the mesh placed behind the target, the ballistic proton trajectories can be calculated. For this a graphical applet has been developed, which is depicted in Figure 3.10.

Each ray passes through its point on the mesh at z_{mesh} and its corresponding image point on the RCF at z_{RCF}. These lines still resemble a purely ballistic trajectory of the protons. By projecting the rays backward, their intersection with a plane parallel to the target surface at different z positions can be calculated. At each plane, the diameter of an enclosing circle can be obtained, which is correlated to the local beam diameter. By plotting the beam diameter as a function of the x position, depicted in Figure 5.6, the position of the minimal diameter of the enclosing circle can be found. This minimum indicates the location of the virtual source.

As shown later in the evaluation of the experiment in Section 5.3, both calculations, mesh magnification and ray-tracing, deliver similar results well within the margin of error.

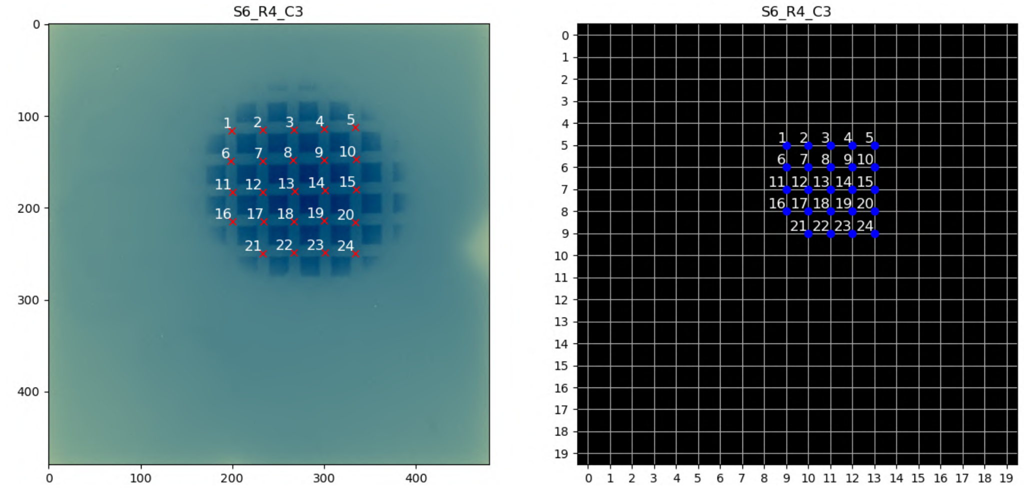

Figure 3.10: Applet used to correlate the RCF mesh intersection points position. The proton image on the RCF might have unusable data points or gaps due to disturbances.

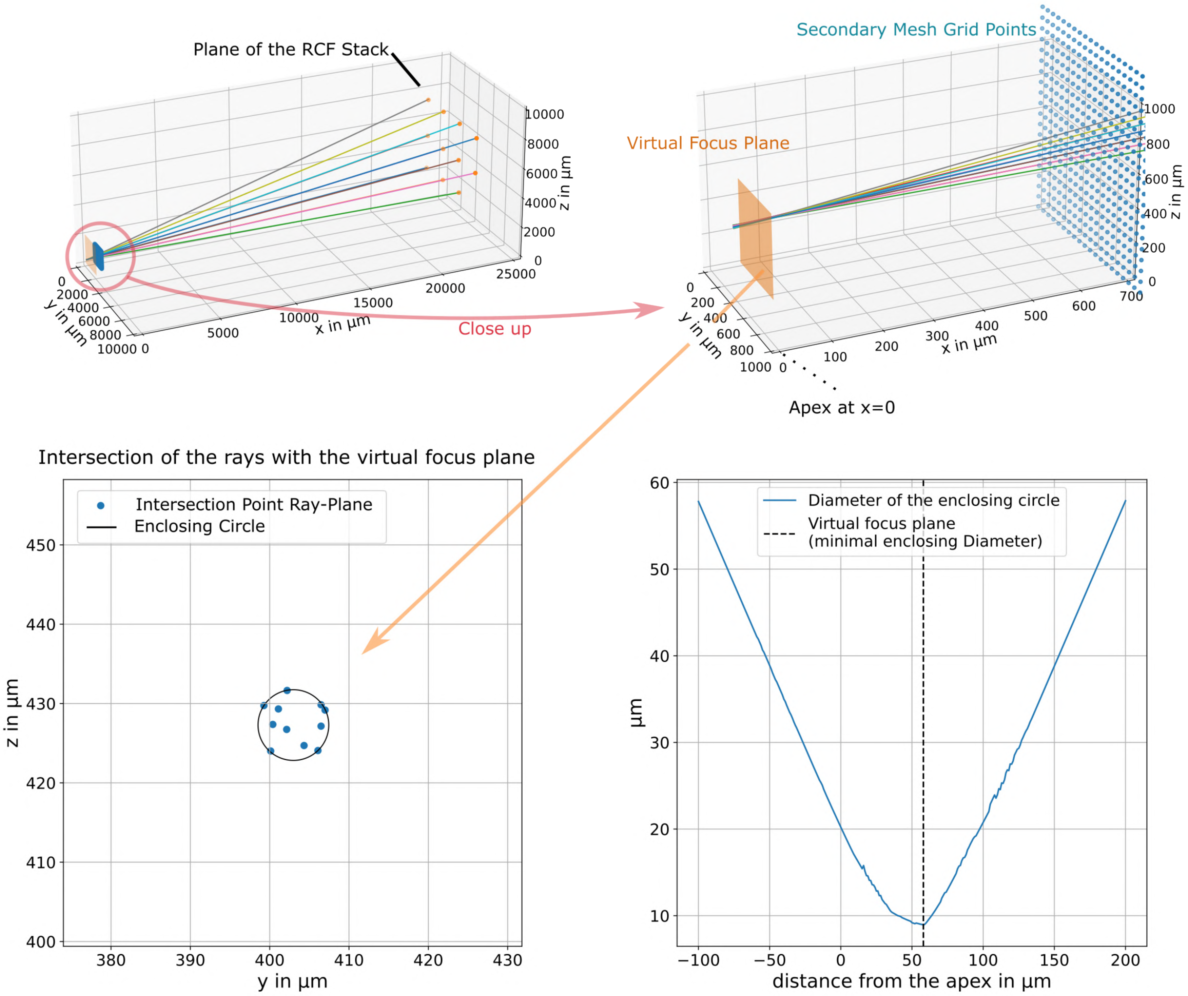

Figure 3.11: The procedure of raytracing the grid intersection points to derive the virtual focus position. Example from a $\varnothing 325\,\mu\mathrm{m}$ partial sphere target with the mesh placed at $x = 690\,\mu\mathrm{m}$ from the concave apex at $x = 0$ and the RCF layer corresponding to $3.4\,\mathrm{MeV}$. The points on the RCF are correlated to the grid points, then calculated to rays, depicted as the lines in the first row. The bottom left plot depicts the intersection points of the rays with the virtual focus plane. On the bottom right, the diameter of the smallest enclosing circle is plotted against the location of the intersection plane.

3.2 XUV Imaging

In addition to the RCF diagnostics, a second diagnostic configuration, based on a XUV imaging system was deployed to probe the thermal emission generated by the protons isochorically heating secondary foils. This diagnostic provides time integrated spatially resolved imaging of the thermal emission at $\sim 13.5\,\mathrm{nm}$ ($\sim 92\,\mathrm{eV}$), which makes it sensitive to the temperatures of near solid density plasmas in the range of tens of electronvolts. The evaluation and calibration of the XUV imager were carried out by collaborators and are therefore not part of the work undertaken by the author of this thesis. The imaging system depicted in Figure 3.12 consists of a single spherical mirror and two flat mirrors. All mirrors are coated with a Silicon / Molybdenum multilayer, with the flat mirrors optimized for an angle of incident (AOI) of 45° and the spherical mirror at 5° with a radius of curvature of $R_c = 50\,\mathrm{cm}$. To reduce the spurious intense emission at low energies and lower the noise level, the XUV beam passes through a $5 \times 5\mathrm{mm}^2$ set of custom-made thin film filters consisting of $100\,\mathrm{nm}$ silicon carbide and $75\,\mathrm{nm}$ molybdenum. Due to the mounting frame's size, carrying 200 targets, in combination with the low AOI of the spherical mirror, one flat mirror was required to redirect the emitted light. An additional flat mirror is necessary to redirect the optical path towards the XUV imager, whose mounting is constraint by the chamber geometry. The total magnification of the system was 10, resulting from a compromise between the expected limited proton spot size predicted by PIC simulations ($< 25\,\mu\mathrm{m}$) and experimental constraints.

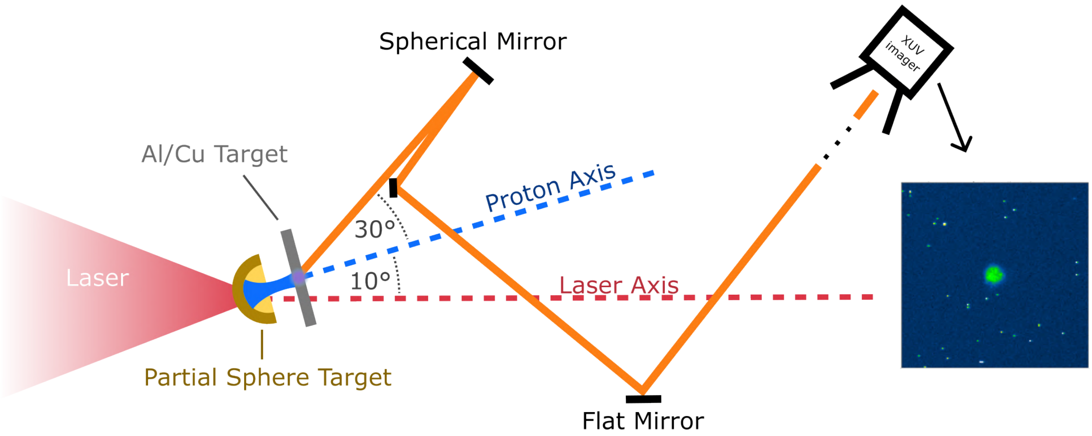

Figure 3.12: Schematic layout of the XUV imaging setup. The XUV imager is mounted outside the chamber. The graphic on the right depicts a XUV image observing the heating of a $2\,\mu\mathrm{m}$ Copper foil mounted $160\,\mu\mathrm{m}$ away from from the apex, with the proton beam generated from a $\varnothing 220\,\mu\mathrm{m}$ partial sphere target.

The XUV signal is detected by a back-illuminated Andor IKon-L X-ray camera outside the vacuum chamber and collected the signal from the rear surface of the heated planar foils (Aluminium $5\,\mu\mathrm{m}$ or Copper $2\,\mu\mathrm{m}$) mounted at distances of $160\,\mu\mathrm{m}$ to $320\,\mu\mathrm{m}$ from the concave apex of the partial sphere primary targets.

The thermal XUV emission is assumed to originate from a blackbody surface at near-solid density. Due to the high opacity of Aluminium and Copper at $92\,\mathrm{eV}$, the emission depth is limited to the first few nanometers of the target surface (Henke et al., 1993). A forward analysis is used to estimate the temperature. First, the emission of the sample is calculated using the one dimensional radiation hydrodynamic code ESTHER (Colombier et al., 2005), assuming isochoric heating and an optically thick sample. This latter assumption was verified using the FLYCHK (Chung et al., 2005) code . Second, this emission is convolved with the transmission of the mirrors, the filter transmission and the response of the X-ray CCD to obtain a relation between the sample temperature and the number of counts. With these results, the temperature of the sample is retrieved on every shot from the peak number of counts. For this experiment the setup enabled the observation of the heating of 88 secondary foils, with an example of a XUV image a foil heated by the protons generated from a ∅220 µm partial sphere target depicted in Figure 3.12.

3.3 Metrology

3.3.1 Confocal Measurement

For the reliable manufacturing of small structures, precise metrology tools are required. During the manufacturing and mapping of the targets produced in this thesis, two devices utilizing the principle of confocal measurement were used.

This technique was first described by Minsky in 1957 (Minsky, 1961) and has since become an important and robust tool in surface metrology for research and industry, particularly with the advent of digital surface characterization tools (Jordan et al., 1998). Figure 3.13 depicts the basic principle of confocal microscopy. A point source, typically a narrow pinhole, emits monochromatic light that is transmitted onto the focal plane of the objective. This results in a high and localized flux at the focus.

If the specimen is at the focal position, the light will be scattered back through the objective, then reflected by a semi-transparent mirror, and focused through another pinhole onto a detector. Light emitted from a plane other than the focal plane will not be focused through the pinhole and therefore, though not fully suppressed, transmits only a small amount of light. Furthermore the initial flux of this plane is much lower than the focal plane, additionally decreasing the signal on the detector (Jordan et al., 1998).

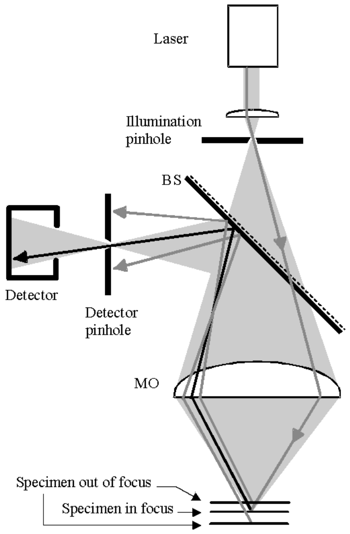

Figure 3.13: Basic principle of confocal microscopy. Image from (Jordan et al., 1998).

The confocal sensor requires a depth scan to measure distances. Chromatic confocal microscopy extends the functionality of confocal measurement and allows for distance measurements without moving parts. This method uses polychromatic light focused along the optical axis of the objective. Depending on the distance of the object, only a narrow bandwidth of light is reflected back from the object's plane into the detector, which now includes a spectrometer allowing to map the distance to a small bandwidth (Lucke et al., 2005).

3.3.2 Confocal Scanning Microscope

Confocal scanning microscopes offer the possibility of quickly scanning the focus point in a plane over the probe instead of the physically moving the probe relative to the sample to generate a 3D scan. Typically the focal point is rastered and the pixels of a CCD serve as the required pinhole. Only the section of the surface that are in the focus plane are therefore imaged on the CCD with a high signal strength. By axially scanning, a 3D surface can be constructed. The lateral resolution of a confocal microscope is superior compared to a wide field microsope, provided a diffraction limited system. The best resolution that theoretically obtainable is $\approx 0.2\,\mu\text{m}$ laterally and $\approx 0.6\,\mu\text{m}$ axially, given by the following equations (Elliott, 2020)

$$R_{lateral} = \frac{0.4\,\lambda}{NA} \tag{3.4}$$

$$R_{axial} = \frac{1.4\,\lambda\eta}{NA^2} \tag{3.5}$$

with λ as the emission light wavelength, the refractive index of the mounting medium η and the numerical aperture NA. For a more in depth discussion of the limits of confocal microscopes and adjustable parameters refer to (Cox, 2012) and (Leach, 2011) for a technical discussion.

3.3.3 Analysis of a 3D areal Surface Texture

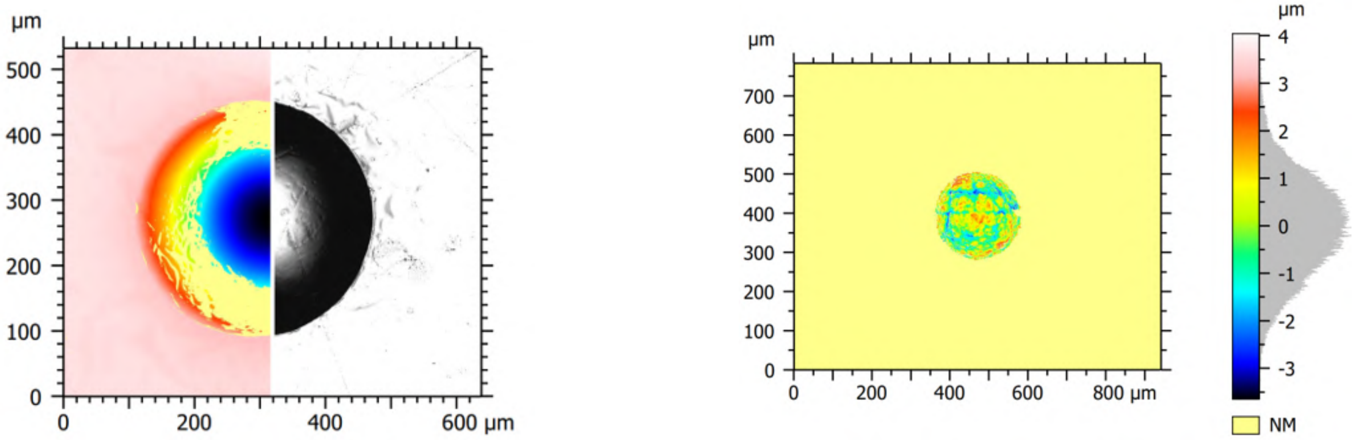

Figure 3.14: Primary surface of a $\varnothing 325\,\mu\text{m}$ spherical target, obtained with a 50x lens on the left. S-F Surface of the evaluation area on the right, with the height density curve on the far right, depicting the density of points relative to the nominal surface.

The quality of the experimental results are critically dependent on the quality of the manufactured targets. By using an international standard, a comparison with targets of other researchers or for future experimental campaigns is possible. That comparability of measured results is independent of specific devices and measurement methods. Calculating surface parameters allows for a objective reference during the developmental phase of a manufacturing process as well as a quality threshold for targets.

In the following subsection, the basic vocabulary used for surface texture analysis is described alongside the operators and surface parameters utilized in the evaluation of the fabricated targets in Section 4.3, based on ISO 25178-2 ("Geometrical product specifications (GPS) – Surface texture: Areal – Part 2: Terms, definitions and surface texture parameters", 2023). The Workflow for the evaluation of the manufactured targets is based on ISO 25178-3 (“Geometrical product specifications (GPS) – Surface texture: Areal – Part 3: Specification operators”, 2012) and described in Section 4.3.1, followed by a discussion of the field parameters obtained.

Basic Vocabulary

- **Skin model**: model of the physical interface of the workpiece with its environment.
- **Electromagnetic surface**: surface obtained by the electromagnetic interaction with the skin model of a workpiece.
- **Primary Surface**: The measured surface after application of an S-filter with a **nesting index** $\mathrm{N_{is}}$ to remove unwanted short-wavelength components (noise).
- **S-F Surface**: The surface obtained after removing form components (**F-operation**) from the primary surface, allowing investigations of deviations from the ideal shape.
- **Evaluation Area** $\tilde{A}$: The specific area of the surface selected for analysis.
- **Field parameters**: Parameters defined from all points of a *scale limited surface*. Detailed in the corrsponding paragraph.

To isolate surface features and remove unwanted components, surface filters are required, yielding a scale-limited surface:

- **S-Filter** (Short-Wavelength Filter): Removes high-frequency components from the measured surface data. A common choice is a Gaussian filter with a specified nesting index N_{is}.
- **L-Filter** (Long-Wavelength Filter): Removes low-frequency components from the surface data, isolating roughness features.
- **F-Operation** (Form Removal): Removes the nominal form from the surface data to analyze deviations from the ideal shape. This is typically done by fitting a geometrical shape (e.g., a sphere) to the surface data and subtracting it.

Geometrical Parameters

Geometrical parameters provide quantitative information on the distribution of material and geometric features over a given surface area. The following list introduces geometric parameters used for analysing spherical targets.

- **Areal Material ratio (curve)**: The ratio of the material portion to the total cross-sectional area of the surface at a specific cut level.
- **Height density curve**: Shows how frequently each surface height occurs within the evaluated area. Depicts if the surface is dominated by specific height ranges (e.g., many peaks around a certain level) or exhibits a broader distribution of elevations (indicating a more irregular texture).
- **Autocorrelation function**: The autocorrelation function (ACF) measures how a surface correlates with itself when shifted laterally by a certain distance. An ACF that decays quickly to zero indicates a more random surface structure, whereas a slowly decaying ACF (or one that exhibits periodic peaks) suggests repetitive features or periodic textures.

Field Parameters

Field parameter offer a numerical descriptor computed from all points of a scale-limited surface. These parameters can be grouped into three categories: height, spatial and hybrid parameters. Height parameters characterize vertical dimensions of the surface texture. Spatial parameters quantify lateral aspects of the surface topography, such as spacing, periodicities and dominant wavelengths. Though not used for the evaluation of spherical targets, they play an important role in the characterization of machined surfaces. Hybrid parameters combine height and lateral information, offering additional, more complex information. While the statistics field parameters provide allow for a direct comparison between surfaces, the usefulness and informational value has to evaluated in the context of the specific features of a scale-limited surface and the filters used to obtain it.

Height Parameters

- **Sq (Root Mean Square Height)**: This parameter is the root mean square of the height distribution relative to a reference plane. It provides a measure of the overall amplitude of surface irregularities, with higher Sq indicating more pronounced peaks and valleys.

$$S_q = \sqrt{\frac{1}{A}\int\int_{\tilde{A}} z^2(x,y)dxdy} \tag{3.6}$$

- **Skewness (Ssk)**: Skewness characterizes the asymmetry of the height distribution. Negative skewness indicates that the surface has deeper valleys relative to its peaks, whereas positive skewness signifies the presence of more pronounced peaks. Surfaces with near-zero skewness exhibit a more symmetrical distribution of heights.

$$S_{sk} = \frac{1}{AS_q^3}\int\int_{\tilde{A}} z^3(x,y)dxdy \tag{3.7}$$

- **Maximum peak height Sp / Maximum pit depth Sv**: Describes the height limits of a scale-limited surface and can be used to calculate maximal height $Sz = Sp - Sv$. Relevant for identifying localized defects of the spherical targets.

Hybrid Parameter

- **Sdq (Root Mean Square Gradient)**: Sdq indicates the average slope of the surface. It is computed as the root mean square of local height gradients and therefore captures how steep surface features are across the evaluated area. Surfaces with high Sdq might exhibit steep transitions or sharp features. The root mean square gradient is used as a tool to flag corrupted targets, in detail discussed in Section 4.3.1.

3.4 Electroplating

Electroplating is a process of depositing a metal coating onto an electrically conducting substrate by using electrolysis. In this process, the surface to be plated is placed in an electrochemical cell as the cathode alongside an anode often made from the metal to be deposited or an inert material like platinum or titanium. The cell contains an electrolyte, rich in metal ions of the plating material, alongside other additive ions to influence the plating characteristics (Dufour, 2006; Wilkinson, 1986).

Electroplating is widely used to enhance surface properties for various applications, including aesthetics in jewelry, corrosion protection, wear resistance, lubrication in industrial components, electrical conductivity in electronic devices, and reflectivity in optical applications (Gugua et al., 2024).

In this thesis, electroplating was used to create arrays of gold targets with a thickness of $\sim 10\,\mu\mathrm{m}$ for laser-driven proton acceleration experiments. This brief explanation focuses on the chemicals and processes used for this specific application, drawing information from Paunovic and Schlesinger's "Modern Electroplating" (Paunovic, 2010). Generally, the bath's composition, metal-ions and supporting electrolytes, along temperature, pH, current density and agitation largely decrement the quality of the deposit.

Potassium dicyanoaurate, $K[Au(CN)_2]$, the most commonly used gold complex ion to deposit gold, was used along a titanium anode in an alkaline bath at a temperature of $70\,^{\circ}\mathrm{C}$ and a current density of $2\,\mathrm{mA\,cm^{-2}}$ to $5\,\mathrm{mA\,cm^{-2}}$. The titanium anode serves as an inert electrode, while the gold ions in the electrolyte are reduced and deposited onto the cathode substrate.

To deposit a metal layer of a desired thickness, the following considerations must be taken into account. Faraday's first law states that the mass w of a substance deposited or liberated at an electrode is directly proportional to the total electric charge Q passing through the electrolyte (Encyclopaedia Britannica, 2024; Wilcox & Gabe, 1992). This relationship can be expressed as:

$$w = ZQ$$

with Z as the electrochemical equivalent.

The electrochemical equivalent Z can be obtained by using the Faraday constant, which equals the amount of charge of one mole of electrons:

$$F = N_{\mathrm{A}} \cdot e = (6.0225 \times 10^{23}) \cdot (1.6021 \times 10^{-19}) = 96.487\,\mathrm{C\,mol^{-1}}$$

with the Avogadro number N_{A} and the elementary charge e. For a reaction involving the exchange of n electrons per deposited ion, the electrochemical equivalent Z calculates to

$$Z = \frac{A_{wt}}{nF}$$

with the atomic weight A_{wt} of the metal deposited. The equation for the relationship between the deposited thickness h over a surface a as a function of the current I and time t for a material with the density ρ can be derived as follows:

$$h = \frac{w}{a\rho} = \frac{ZQ}{a\rho} = \frac{ZIt}{a\rho} = \frac{ZJt}{\rho} \tag{3.8}$$

where w is the mass deposited, $Q = It$ the total charge passed, and $J = I/a$ the current density. This derivation assumes an efficiency of 100%.

An *Auruna 552®* bath, containing Gold Cyanide and manufactured by Umicore (Umicore Galvanotechnik GmbH, 2009), was operated at a current density of $J = 25\,\mathrm{mA\,mm^{-2}}$ based on the manufacturer's recommendation. On a surface of $400\,\mathrm{mm^2}$, this requires a current of $I = J \times a = 1\,\mathrm{A}$. Then the electrochemical equivalent Z for gold is calculated as:

$$Z = \frac{197\,\mathrm{g\,mol^{-1}}}{1 \cdot 96\,487\,\mathrm{C\,mol^{-1}}} \approx 0.002\,\mathrm{g\,C^{-1}}$$

using the atomic weight of gold $A_{wt} = 197\,\mathrm{g\,mol^{-1}}$ and the number of electrons per ion exchanged of $n = 1$.

The required time t to deposit a gold layer with a thickness $h = 10\,\mathrm{\mu m}$ is calculated as:

$$t = \frac{h\rho}{ZJ} = \frac{0.01\,\mathrm{mm} \cdot 0.0193\,\mathrm{g\,mm^{-3}}}{0.002\,\mathrm{g\,C^{-1}} \cdot 25 \times 10^{-6}\,\mathrm{A\,mm^{-2}}} = 3860\,\mathrm{s} \approx 1\,\mathrm{h}\,4\,\mathrm{min} \tag{3.9}$$

4 Arrays of Partial Sphere Targets

In this thesis a batch fabrication method for partial sphere targets has been developed. 1050 partial sphere targets have been manufactured and thoroughly characterized for an experimental campaign to deepen the understanding of proton focusing from spherical targets for Proton Fast Ignition. In addition, a procedure to precisely align hundreds of targets rapidly and precisely on the experimental site has been developed and successfully implemented in an experimental campaign, with its reliability validated and quantified.

These developments are motivated by recent advances in high-repetition, high-intensity laser systems such as the Colorado State University ALEPH-L (Wang et al., 2017), the ELI-Beamlines High-Repetition-Rate Advanced Petawatt Laser System (HAPLS) (Borneis et al., 2021), the Berkeley Lab Laser Accelerator (BELLA) (Nakamura et al., 2017), and the National Institutes for Quantum Science and Technology J-KAREN-P (Nishiuchi et al., 2017), which bring new challenges and opportunities for diagnostics and target fabrication. Experimental campaigns operating with repetition ranges of seconds instead of hours generate extensive data for statistical analysis in a short time and allow the exploration of multiple parameters within a single experimental campaign.

To support the high throughput campaigns targets need to be produced with a consistent quality, efficiently, and their on-site alignment must be fast, yet reliable, with an automatic target placement system.

While there is no universal solution to the previously mentioned challenges, various target options are available depending on specific experimental requirements. One option to provide foil targets, even at higher repetition rates, is the use of tape targets. In this setup, a thin foil tape is continuously driven through the interaction point. This approach enables a high repetition rate and a large number of shots, but comes with a more limited selection of target materials and configurations, as well as relatively complex hardware (Ehret et al., 2023; Xu et al., 2023).
Another solution is to place a foil within a frame, sectioning it into smaller areas, which are then sequentially positioned in the lasers focal position, known as the interaction point (IAP), for each shot. In this setup, the number of shots is limited by the frame's size constraints, typically accommodating only a few hundreds of targets at the benefit of less limitations on the target material and a simpler mounting of secondary targets. It is important to note that the targets must be kept at a distance and shielded from one another due to shockwaves, shrapnel, stray laser light and plasma produced from the joules of energy that are deposited onto the target during the laser-matter interaction. Due to imperfections in the mounting and geometry of the target frame, the foil within, and the positioning stages, the accuracy of the placement in the IAP might be compromised. One option to counteract positional errors along the target normal is to place a confocal sensor (see Section 3.3.1) along this axis. By calibrating the sensor to the IAP and then pre-positioning the target foil, deviations from the expected placement of the foil can be measured and corrected. In contrast to the target normal error the radial position errors are of minor importance for foil targets because their surface area typically exceeds the laser spot size by an order of magnitude, making them less sensitive to such misalignments. While these setups allow for a fast and efficient placement of simple foil targets, more complex targets like spherical targets require precise alignment in all dimensions. Alignment of such targets is usually done prior each shot, which is acceptable for laser systems which allow for only a few shots per day.

The campaign later discussed in Chapter 5 at the L-ALEPH laser requires an automatic, fast and precise method of placing the targets in the IAP to allow for a fast succession of ($\sim 0.2\,\mathrm{Hz}$) shots needed to statistically cover the larger parameter space the campaign aims to explore.

In the following, the fabrication and validation process of these partial sphere targets are detailed in Section 4.2 and Section 4.3, with the challenges of their alignment along with the methods to overcome them presented in Section 4.4.1. The performance and reliability of this target alignment procedure is the evaluated in Section 4.4.2.

4.1 Design Description

The experiment investigates the focusing properties of different sizes at different relative illuminations of spherical targets and compares the results to simulations. To achieve this, two different types of secondary targets are positioned behind the spherical target at distances of approximately $275\,\mu\text{m}$ to $1000\,\mu\text{m}$. A thin foil, in combination with an XUV image is used to detect the proton heating at the given location. Additionally, in different shot sequences, the secondary metallic sample is replaced by a mesh placed in front of a RCF stack. This configuration allows a measurement of the energy distribution and trajectories of the accelerated protons. Figure 4.1 shows a schematic of the experiment conducted, depicting the primary spherical target along the secondary target. A total of 42 different target configurations were manufactured for this campaign, amounting to 1650 targets in total. These configurations consist of four groups of primary targets: three spherical targets with diameters of $220\,\mu\text{m}$, $325\,\mu\text{m}$ and $525\,\mu\text{m}$ and flat foils, which are listed as targets of $\varnothing 0\,\mu\text{m}$.

Three groups of secondary targets were built:

- Flat Foils: The first group comprises flat foils made from $2\,\mu\text{m}$ copper (Goodfellow, 2023b) and $5\,\mu\text{m}$ aluminum (Goodfellow, 2023a). These flat secondary targets interact with the proton beam, allowing for diagnostic measurements such as thermal radiation in the visible and XUV ranges.
- Copper Meshes: The second group consists of copper meshes with line densities of 400lpi (AgarScientific, 2024a) and 600lpi (AgarScientific, 2024b). These meshes are used in conjunction with radiochromic films (RCFs) to provide information about the protons' trajectory, as discussed in Section 3.1.2. Secondary targets were mounted at distances ranging from as close as $160\,\mu\text{m}$ up to $960\,\mu\text{m}$ from the primary target.
- No Secondary Target: Finally, shots conducted without any secondary target allowed for measurements of the spatial energy distribution and conversion efficiency using RCFs, as previously discussed in Section 3.1.

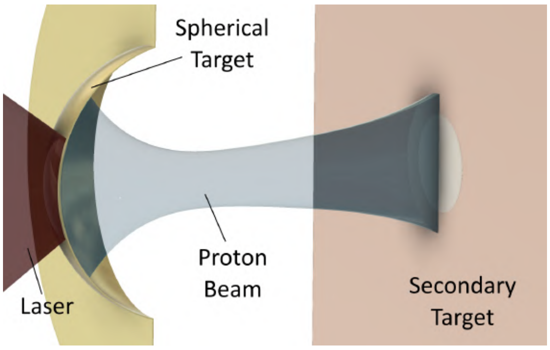

Figure 4.1: Schematic of the experiment conducted. Primary partial sphere target on the left. Secondary target for heating on the right.

Figure 4.2 depicts a schematic of the different features of the partial sphere targets, whose manufacturing is described in the following Section 4.2. The fabricated geometry results from the constrains dictated by the manufacturing and the experimental requirements for the acceleration and focusing of protons using the ALEPH-L laser system. The partial sphere target can be separated into four sections, depicted in Figure 4.2 with the most important one being the *region of interest* (ROI), where the laser interacts with the target and the protons are accelerated from. The size of this area stems from the laser's pointing stability – the consistency of the laser in delivering pulses in the same direction – and its FWHM focus diameter, which in turn correlates to the range at which the protons are emitted from (M. Schollmeier et al., 2007). Therefore special emphasis was set on the quality of this area, with a defined size of $d_2 = 100\,\mu\text{m}$.

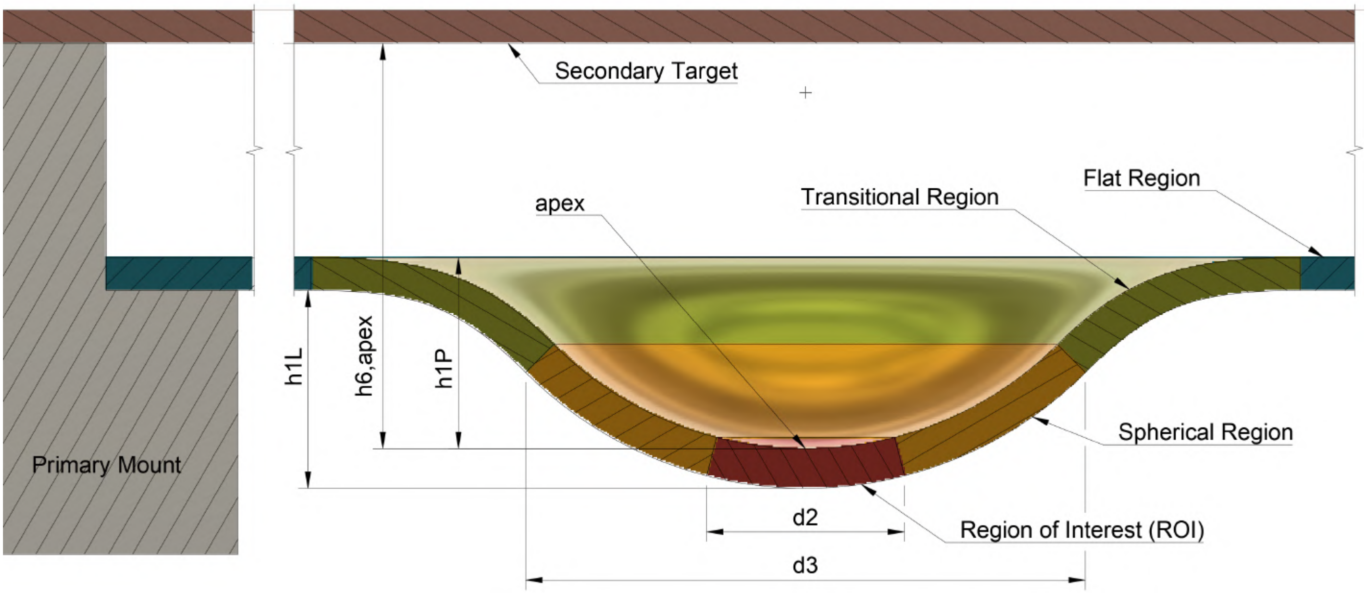

Figure 4.2: Sketch of a partial sphere target and a secondary target. Features exaggerated. Description in the text.

In contrast to the ROI which has a fixed size for all three diameters, the *spherical region* varies with the size of the targets. This region is defined as the area where the surface maintains a consistent spherical shape, with deviations similar to those within the ROI. Though this region slightly varies between the individual targets of a group its diameter has been conservatively set to $d_{3,\,240} = 130\,\mu\text{m}$, $d_{3,\,340} = 220\,\mu\text{m}$ and $d_{3,\,540} = 300\,\mu\text{m}$. Moving outwards follows a transitional region and then a flat region. The distance between the apex and the flat region, h_1, slightly varies between batches of targets and had to be accounted for during the mounting of the targets in an effort to keep the distance h_6 between the apex and the secondary target as consistent as possible. This h_6 is of major importance for the experiment, as the proton beam continuously changes along its direction of propagation. Therefore, the reliability and accuracy of the information obtained from different secondary target configurations, heavily depends on an accurate placement and well-characterized uncertainties.

The target configurations described above were manufactured and assembled into grids of 5×5 targets, with a spacing of 3 mm between them – the minimal distance required to prevent the destruction of neighboring targets during the experiment. These 5×5 grids are integrated into two aluminum mounts: one mounting the partial sphere targets in the carrier foil, and the other mounting the secondary targets. Each group of 25 targets typically contains a single configuration, defined as a specific combination of primary and secondary targets, with the exception of mesh targets, where multiple configurations may be included within the same

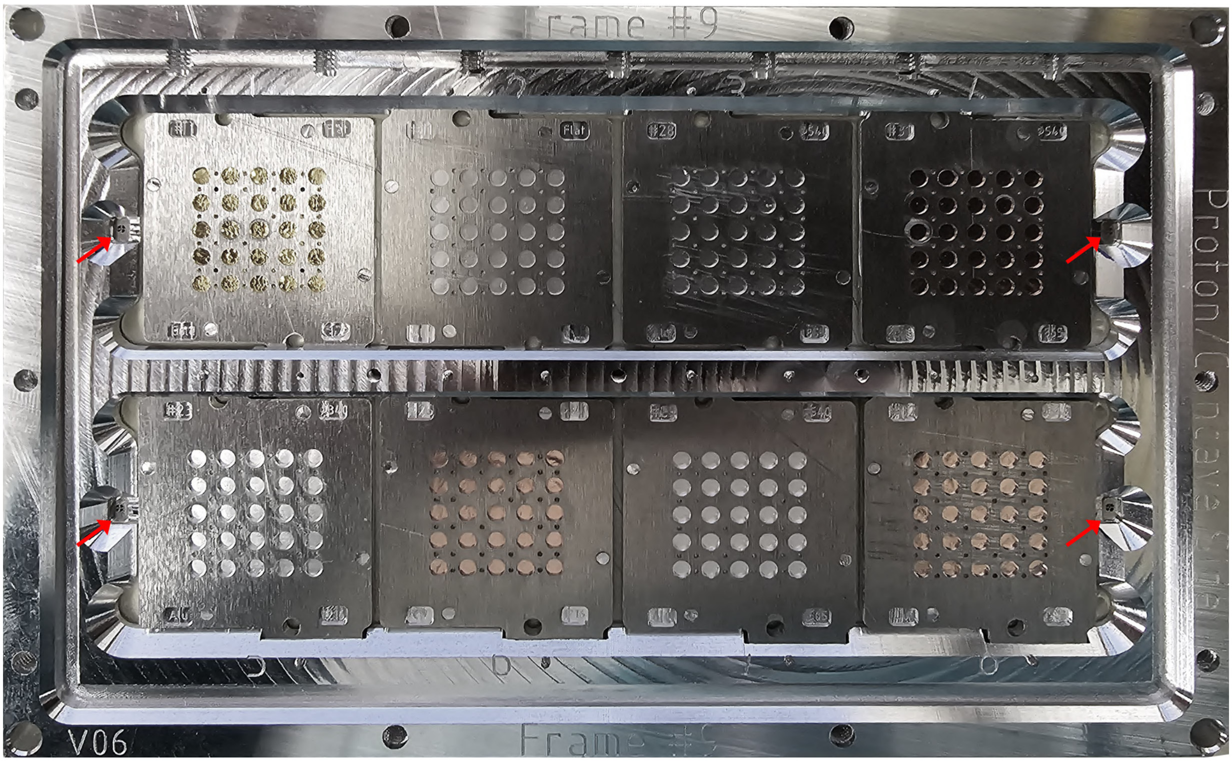

Figure 4.3: Frame 9 displaying various target configurations, including those without secondary targets (gold, top left) and with copper and aluminium foils. Red arrows indicate the alignment features used in the alignment process described in Section 4.4. View onto the proton emitting side.

group to accommodate different mesh distances.
These assembled grids are then mounted into a larger frame that holds 2×4 groups of 25 targets, totaling 200 targets per frame. In total nine frames, one being shown in Figure 4.3, were manufactured for the experiment, providing a substantial number of targets to support high-repetition-rate laser operations.

4.2 Fabrication of Spherical Targets

For the experiment discussed in this thesis 1050 partial sphere targets were produced. To achieve this, a refined workflow fabricating 5×5 arrays of spherical targets was developed, detailed in the following paragraphs. A major focus during the fabrication of the targets has been their curvature, especially in the central region of interest, as this has a major influence on the focusing properties of the proton beam, as later discussed in Section 5.2.

Additionally, achieving a high surface quality on the proton emitting concave surface was crucial. To more specifically quantify this, field parameters have been evaluated in the following Section 4.3.

Flat foils of the desired target thickness of $10\,\mu\mathrm{m}$ are commercially available. Their reshaping into spherical targets has been experimentally explored by directly forming the material using a custom die. These dies were familiar in design to those used in the process discussed in the following paragraphs and shown in Figure 4.4. This process did not result in usable targets: When stretch forming, the gold foil needs to be extended further than the yield point to then take the desired shape. As the desired shape is spherical the die needs to be slightly elliptical to stretch the foil sufficiently (Altan & Tekkaya, 2012, Chap 6.5) . Fabricating dies in the desired shape and quality was beyond the available machining capabilities of the laboratory. Using a spherical

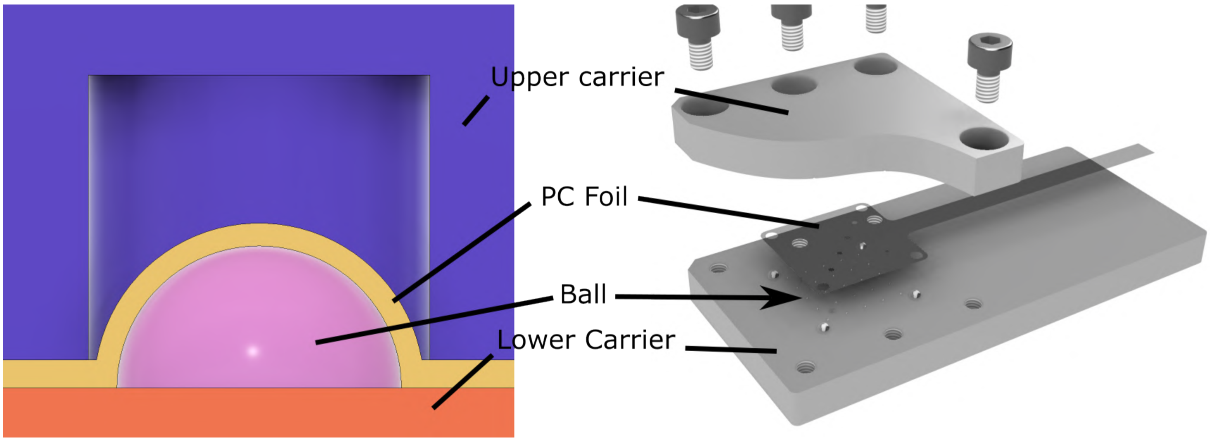

Figure 4.4: Pressing of the Polycarbonate. (Left) Close up sketch of the deformed PC foil in between the two dies. (Right) Render of the setup used to mount and guide the two dies.

die resulted in a flattened apex of the formed target, an issue most present at the important *region of interest*. Additionally the foil is stretched during this procedure, resulting in an uneven reduction of the thickness of the foil and stretch marks at areas of high stress (Todd et al., 1994, p.315). Finally, the quality of the concave surface depends on the initial quality of the foil as well as the surface of the die and therefore the balls used in its assembly. Measurements of the surface of targets fabricated using this method showed inferior quality compared to the method described in the next paragraphs.

While direct forming of the targets grants the benefit of reduced cost and high volumes for large quantities of targets, shaping foils in the order of $10\,\mu\mathrm{m}$ is still a relatively unexplored field in engineering (Altan & Tekkaya, 2012). To address this for future campaigns, a cooperation with the *Institute for Production Engineering and Forming Machines* (PTU) in Darmstadt has been established. Initial simulations are being conducted to explore deep drawing and hydro forming techniques for the production of spherical targets.

Faced with the previously mentioned issues a different process has been developed, involving the production of a stencil, which is then electroplated and dissolved. Instead of directly forming the gold foil, a $20\,\mu\mathrm{m}$ polycarbonate (PC) foil, previously laser cut to shape, is formed by placing it in between two dies. As shown in Figure 4.4, the lower die contains an array of 25 stainless balls with a diameter of $200\,\mu\mathrm{m}$, $300\,\mu\mathrm{m}$ and $500\,\mu\mathrm{m}$, corresponding to the different target sizes. On the opposing side of the workpiece, the upper die offers cylindrical cups with diameters of $240\,\mu\mathrm{m}$, $340\,\mu\mathrm{m}$ and $540\,\mu\mathrm{m}$. To precisely guide the two tools relative to each other, balls of $\varnothing 800\,\mu\mathrm{m}$ are inserted into matching holes.

The two parts are then pressed together and the polycarbonate is briefly heated beyond its glass temperature of $T_{g,\mathrm{PC}} \approx 150\,^{\circ}\mathrm{C}$ (Mark, 1999) by placing the assembly on a heated plate for $2.5\,\mathrm{min}$, followed by conductive cooling. This procedure allows the polycarbonate to ’flow’ or ’relax’ into the new shape. While the concave surface inherits the surface structure of the die it is pressed with, the resulting convex surface is smooth, as smaller imperfections on the balls surface are mitigated by the softening polymer.
Next, the new polycarbonate stencil is mounted into an aluminium mount with a mask covering all but the surfaces to be electroplated. The masked stencil is then placed into a sputtering device, selectively disposing a thin layer of gold onto the exposed areas of the polymer.

This conducting surface provides a base layer for the electroplating, then increasing the thickness of the layer to the desired $10\,\mu\mathrm{m}$. During the electrochemical deposition, the PC stencil is placed in a polytetrafluoroethylene (PTFE) mount to hold it in place and to prevent warping of the object due to the changes in temperature. After thorough cleaning, the PC is then dissolved in dichloromethane (CH_2Cl_2) and the remaining gold foil containing the spherical targets is retrieved, cleaned and prepared for mounting. This method yields superior surface quality on the proton-emitting concave side, albeit at the cost of a more complex manufacturing process. However, the convex side facing the laser exhibits lower surface quality due to the imperfect electroplating process, and it remains uncertain whether this adversely affects laser absorption or the TNSA mechanism. An more detailed analysis of the targets quality follows in Section 4.3.

Assembly of the Secondary Targets

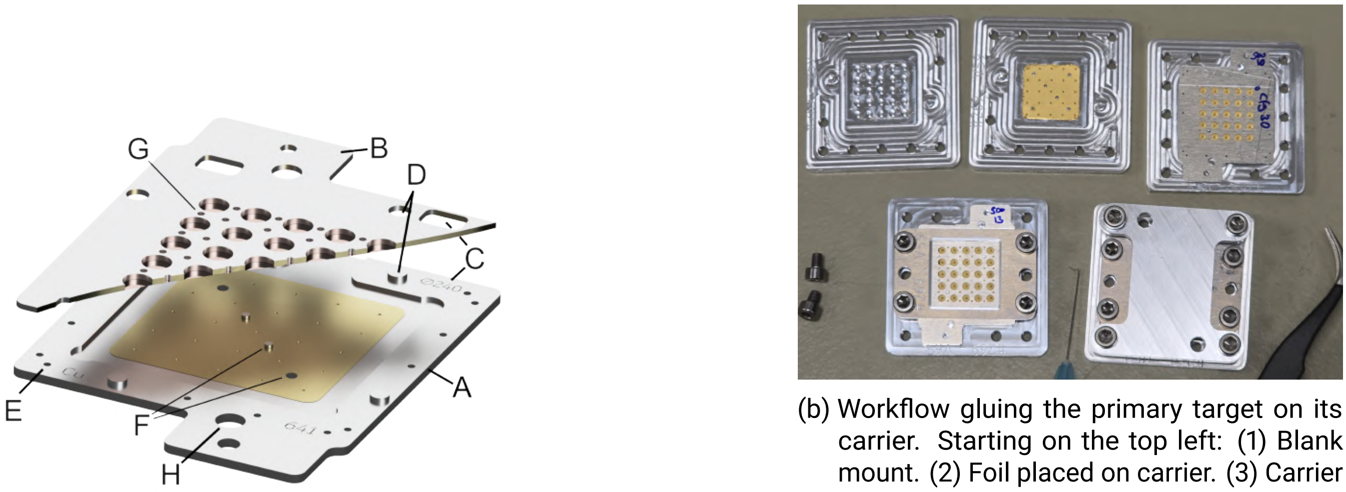

(a) Primary target carrier (bottom) and secondary target carrier (top, sectioned).

(b) Workflow gluing the primary target on its carrier. Starting on the top left: (1) Blank mount. (2) Foil placed on carrier. (3) Carrier placed on top. (4) Attachment added, glue is applied. (5) additional part presses the carrier onto the foil.

Figure 4.5: Secondary Assembly

After the fabrication of the spherical gold targets, the next step involves assembling them with the secondary targets to create a complete set of targets. Once the gold foil containing 25 spherical targets is cleaned it is carefully placed on a machined mount, depcited in Figure 4.5a which provides two long studs passing though two of the foils alignment holes (I). Then the primary carrier (A) is placed on top, also guided by the studs, and pressed against the foil using an additional top piece. Next, epoxy glue is applied in the $\varnothing 400\,\mu\mathrm{m}$ holes (G, not visible on primary carrier in Fig 4.5a), permanently connecting targets and carrier while making sure that the glue cannot flow between the foil and carrier in a way that would lift or misalign the foil.

Prior mounting, each target is mapped using a confocal microscope (Section 3.3.1). This step is crucial because it provides the distance between the laser side apex and laser side flat region, $h1L$ (Figure 4.2). Since the value varies between targets, its average across the 5×5 array is used to tailor the depth of the pocket in the primary mount (A) to each individual set. This customization minimizes the variation of the distance between the targets apex and secondary target, greatly reducing the uncertainty in the experimental results. The secondary gold and copper foils are mounted on secondary carrier in a similar fashion to the primary target, but do not require any individual compensations. The primary target carrier (A) is placed on top of the secondary target carrier (B), with the alignment assured by the four alignment studs and corresponding holes (D). They are then permanently fixed by inserting epoxy glue into the designated holes (E) while maintaining constant pressure on the two parts.

Each primary carrier is engraved with the type of primary and secondary target, its configuration number and the pocket's designed depth (C). This labeling allows for an easier identification and ensures correct assembly of the target configurations.

Because the distance between primary and secondary targets varies among configurations, the total thickness of the carrier changes accordingly.

Its design along with the primary and secondary mounts has been constrained by the alignment procedure described in Section 4.4. Here a confocal microscope with a 20x lens with a working distance of 1 mm is used, limiting the depth of the primary target inside the frame relative to its top. To limit the movement of the axis in the experiment and the scanning range required by the microscope, all apexes of the primary targets should be mounted in a single plane.

Therefore the 4×2 carrier holding frame must accommodate these variations, therefore linking the carrier's mounting depth to each configuration.

As an additional constraint on the frame's design, the space allocated for targets and alignment features—discussed in the following section—is limited by the stage's range of motion.

4.3 Manufacturing Evaluation

4.3.1 Spherical Targets

Procedure The evaluation of the quality of the spherical targets follows the recommendations for the evaluation of an *electromagnetic surface* as per ISO 25178-3:2012(“Geometrical product specifications (GPS) – Surface texture: Areal – Part 3: Specification operators”, 2012), utilizing the terminology of ISO 25178-2:2023(“Geometrical product specifications (GPS) – Surface texture: Areal – Part 3: Specification operators”, 2012), indicated by an italic font. The methods are introduced in Section 3.3.3.

One of the goals of the measurements of the partial sphere targets is to quantify important *field parameters* to verify the quality of each target for proton focusing experiments. Additionally, this offers a benchmark for future experiments. To achieve detailed verification, the proton emitting concave side of 129 targets has been mapped prior mounting. Furthermore, the convex laser side of all mounted targets was scanned using a mostly automatic approach. These scans serve not only for quality assessment and flagging of defect targets, but are crucial for the alignment procedure described in Section 4.4. Once all targets of a frame are assembled and mounted they are placed at a precise position on the stage of an optical profilometer (Sensofar S-NEOX) using a custom mount. Due to the comparatively large spacial expansion of the targets and alignment features of $124\,\mathrm{mm} \times 81\,\mathrm{mm}$ and the high resolution required of each single target it is unpractical to scan the entire frame in a high resolution, instead a two step procedure is used to find and map the targets:

- **pre-alignment**: using a 20x lens with a field of view (FOV) of $885\,\mu\mathrm{m} \times 707\,\mu\mathrm{m}$ all targets are sequentially scanned at their expected position in the frame and the position of the sphere is stored.
- **precise mapping**:
  - The **alignment features** are manually found and their position is stored.
  - A **high resolution scan** using the 50x lens with a FOV of $338\,\mu\mathrm{m} \times 283\,\mu\mathrm{m}$ of all targets is made using the improved positional data obtained in the previous step. If the target is a $\varnothing 525\,\mu\mathrm{m}$ target, a 2×2 image stitching is used.
  - Finally the **alignment features** are mapped again to confirm that the frame has not shifted in its mount.

An example of the resulting 3D scan of a convex surface of a $\varnothing 325\,\mu\mathrm{m}$ target is shown in Figure 4.6b. Here a limitation of the system becomes visible: the maximum measurable surface slope is limited. The 50x lens allows measurements of up to $53\,\mathrm{deg}$ under ideal conditions on a smooth surface. Slopes beyond this limit are no longer detectable, resulting in an incomplete surface for the characterization.

By fitting a sphere to the highest part of the 3D scan, the positions of all (convex) apices is now know in the coordinate system of the profilometer along with positions of the four alignment features. Which lays the foundation for the alignment procedure discussed in Section 4.4.

While all targets have their convex side scanned, the concave surface of 129 targets has been mapped to quantify the quality of the manufacturing. The limitation on the detectable slopes also results in an incomplete high resolution image of the concave spherical target, which is acceptable, as evaluation is only focused on the central *evaluation area* of $\varnothing 100\,\mu\mathrm{m}$ around the apex, approximated by the central *pit* of the surface.

To quantify the surface a *S-F surface* (form removed surface) is calculated, by applying surface filtering techniques. Specifically, a total least square sphere (TLSSP) fit with a diameter of $220\,\mu\mathrm{m}, 325\,\mu\mathrm{m}$ or $525\,\mu\mathrm{m}$ is used as the *F-operation* to remove the nominal form from the surface data. These diameters are the expected diameters of the concave surface of the PC. A more complete scan can be obtained by using a lower magnification lens, which provides information about the entire target. A *nesting index* $N_i = 0.8\,\mu\mathrm{m}$ is applied as the *S-filter*, based on the ISO25178-3:2012 (“Geometrical product specifications (GPS) – Surface texture:

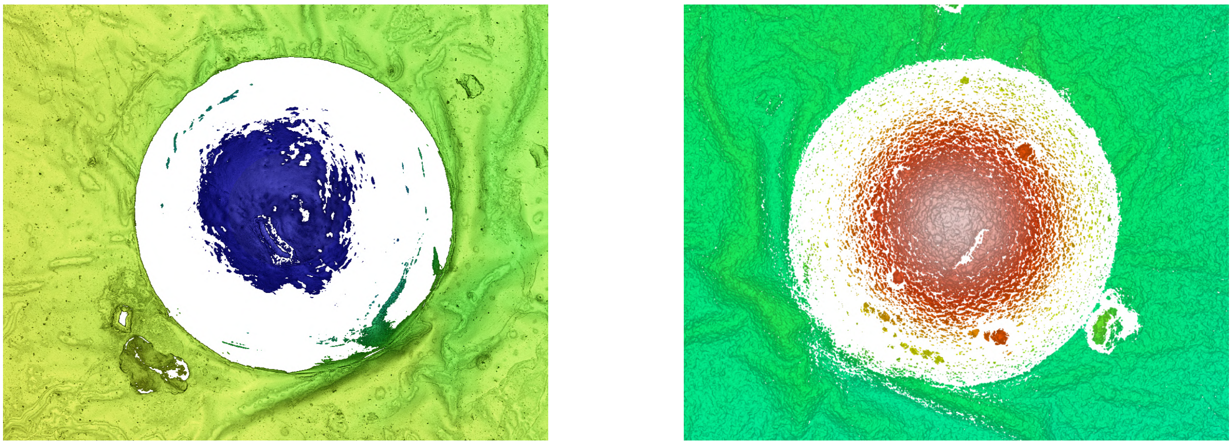

(a) Concave side of a $\varnothing 325\,\mu\mathrm{m}$ target.

(b) Convex side of a $\varnothing 325\,\mu\mathrm{m}$ target.

Figure 4.6: When comparing the convex and concave side of the same target, the central defect is clearly visible. The higher roughness of the surface averted from the polycarbonate is also clearly visible.

Areal – Part 3: Specification operators”, 2012) recommendations for the sampling distance of 0.28 µm of the used system and with a Gaussian filter. This process yields the surface parameters presented in Table 4.1.

Discussion Different proton acceleration experiments have shown that the proton beam accelerated from rear surface of a TNSA target inherits features present on that surface. For example Cowan et al. (Cowan et al., 2004) used 200 µm deep micro machined grooves of periodic and asymmetric shapes to directly measure the source size of the beam for different proton energies.

These experiments where motivated by observations of Roth et al. (Roth et al., 2002) who observed features from the targets rear surface imprinted in the proton beam onto the RCF. Based on this they concluded that the protons are accelerated from a cold unperturbed surface and result in a highly laminar beam.

From these experiments it can be concluded that surface features with a size smaller than the thickness of the sheath, usually in the range of micrometers (M. S. Schollmeier, 2009), result in a local modulation of the proton beam changing the intensity localized, as seen in Figure 4.7.

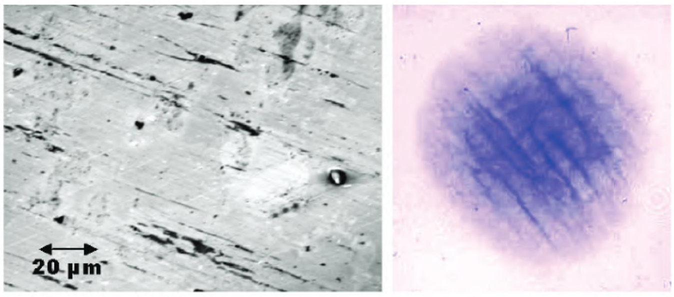

Figure 4.7: Surface imaged by accelerated protons. The structures at the targets rear surface (left) were imaged by the proton beam onto the detector (right). Image from Roth et al. (Roth et al., 2002).

As previously discussed in Section 2.5, the divergence of an TNSA beam primarily stems from the shape of the electron sheath, which is usually of Gaussian shape. The protons follow the density curve of that sheath. By shaping the target on a macroscopic scale, the direction of the protons emitted from the targets rear surface can be manipulated. For example a partial sphere target can be used to focus the beam towards the geometrical center of that sphere. Seeing the direction of acceleration of the protons as a superposition of the targets surface and a Gaussian shape, it becomes clear, that undesired deviations from the form of the target result in an unwanted modulation of the proton beam.

From these observations it can be concluded that variations of the targets gradient significantly affects the resulting beam, either microscopically by modulating the initial angle the protons leave the targets surface prior acceleration to the electron sheath or by modulating the entire sheath.

Therefore, from a manufacturing quality perspective, height parameters as a quantification metric do not offer a direct information about the surfaces quality in regard to proton acceleration. As seen in Figure 4.8, the height parameters of the three example surfaces are similar, even though the beam resulting from them will differ, as their surface normals are different.

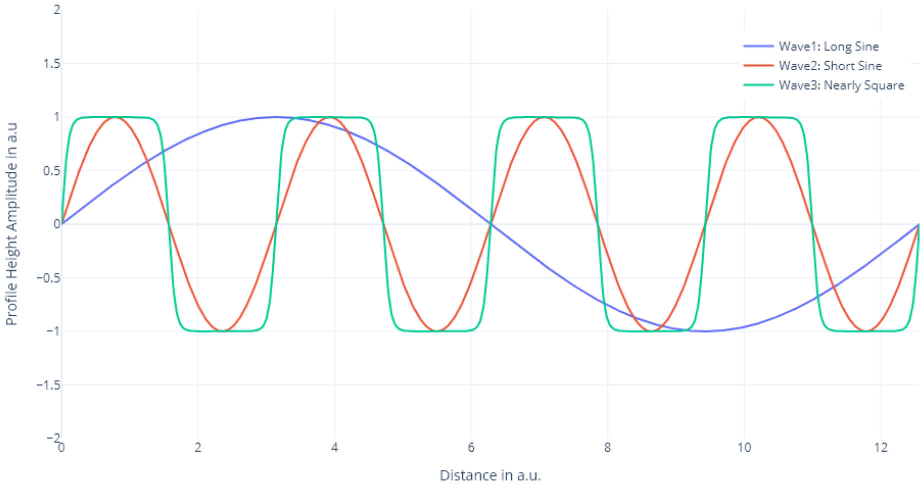

Figure 4.8: In this example the three sample profiles show an Sq of 0.7, 0.7 and 1. Sz is identical for all three. Sdq calculates to 0.35, 1.4 and 2.9. Given the right filters, Sdq could therefore be used as an indicator of the surface quality in regard to the acceleration of a proton beam. It is important to remark that this example shows the field parameters of a surface profile texture, not an areal profile texture.

In contrast to the simple height parameters like Sq and Sz, the root mean square gradient Sdq provides different values, allowing for a more applied information about a targets surface, especially in conjunction with correspondingly chosen surface filters.

Being of square nature, the Sdq parameter weights localized surface imperfections, like dents or contaminations. Therefore making it an effective tool for quality control in target manufacturing, as surface gradients strongly affect beam uniformity. Examples of different defects can be seen in Figure 4.9 a) and Figure 4.6.

These imperfections can be the result of:

- Imperfections in the polycarbonate surface: Irregularities on the surface on the PC surface present prior or post the deformation process. These can be scratches present in the stock foil, marks from misalignment of the dies or dust and particles on the to be sputtered surface. These translate to an undesired electroplated surface, as it can be seen in Figure 4.6b.

- Contaminations on the finished target: Besides dust particles, remnants of PC can remain on the concave

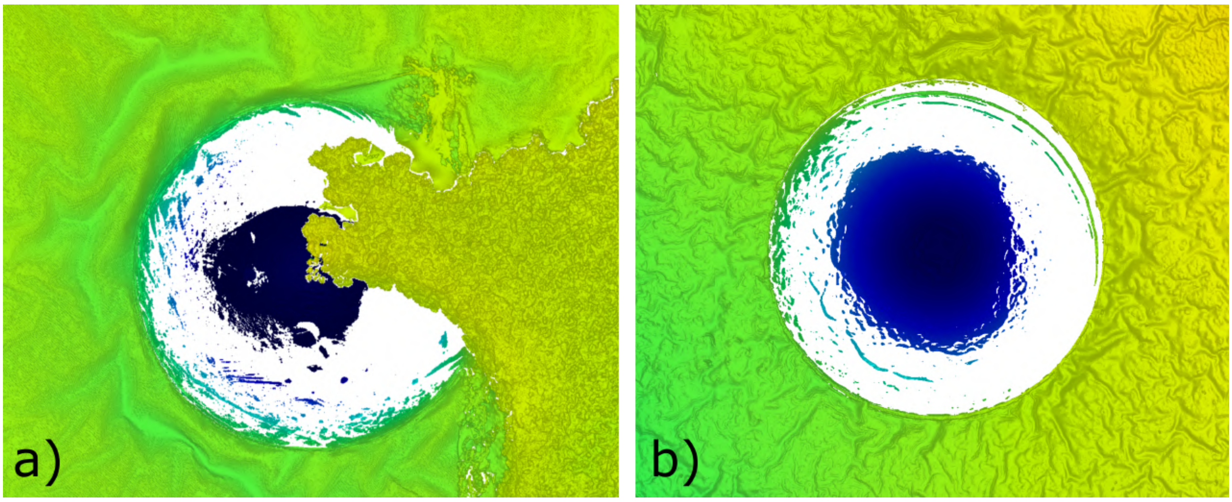

Figure 4.9: a) $\varnothing 325$ µm target with contamination on its concave side. b) $\varnothing 325$ µm target with no imperfections.

surface as well as flakes of gold, with an example shown in Figure 4.9 a).

- Issues during the electroplating or following handling: During the electroplating the emerging foil can locally detach from the polycarbonate. Premature local detachment during the dissolvement of the PC can also result in wrinkles. Furthermore the manual handling and mounting of the foil can occasionally damage the targets.

When deforming the polycarbonate during the drawing process, its thickness is reduced from 20 µm to approximately 10 µm to 12 µm due to the increase in the surface area, resulting in the TLSSP fit radii of $r_{TLSSP} = r_{Ball} + 10$ µm to 12 µm. In contrast to the larger two diameters, a $h1P_{240,avg} = 89$ µm (Figure 4.12) indicates that the concave side of the PC has nearly been fully deformed to a half sphere. Measurements of the used dies indicate that the mounted $\varnothing 200$ µm balls are sticking relatively further out from the surface than the $\varnothing 300$ µm and $\varnothing 500$ µm balls.

It can be argued, that the larger relative thickness of the polycarbonate compared to the depth of the deformation (ball radius) results in a less consistent distribution of the polycarbonate resulting in a larger deviation from the ideal sphere on the polycarbonates convex side.

Parameter / TLSSP fit	220	325	525	unit
Sq	0.54	0.22	0.24	µm
Sdq	5.94	3.13	3.58	deg
Sz	3.72	1.47	1.89	µm

Table 4.1: Field parameters obtained from the *S-F surface* of the concave side of the spherical targets

Indeed, when comparing the field parameters Sq and Sz of table 4.1, it becomes evident that the $\varnothing 220$ µm targets exhibit larger deviations from the ideal spherical shape. This can, besides the previously mentioned slightly different dies, be attributed to the challenges caused by their smaller size. As the *evaluation area* of $\varnothing 100$ µm is consistent for all three sizes, it covers a wider range of curvature of the sphere, increasing the influence of the deviation of the *F-operations* set radius to the actual radius of the sphere, which is depicted in Figure 4.10. Effectively the influence of a relatively larger *transitional region* might influence the quality at the *evaluation area*. This effect manifests in the wider distribution of the averaged *height density map* for

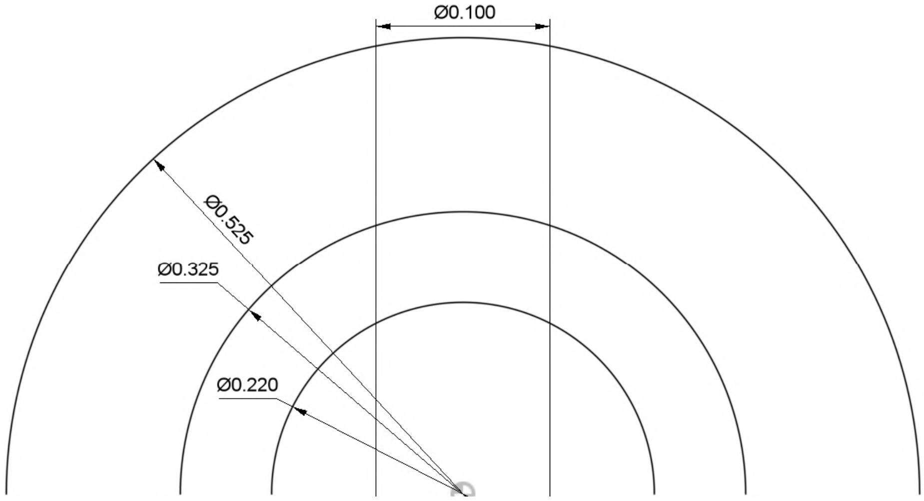

Figure 4.10: Sketch of the three spherical target sizes. The central evaluation of $\varnothing 100\,\mu\mathrm{m}$ is similar for all three sizes, but the curvature it covers differs.

$\varnothing 220\,\mu\mathrm{m}$ targets shown in Figure 4.11, resulting primarily in a larger values for the field parameter Sq.

Nearly all the defects are visible in measurements of both sides of the finished targets. Only surface contaminations like residues or dust particle are only detectable on their respective side. While the concave, proton emitting side is critical for the experiments, the convex, laser facing side is visible in mounted targets and is therefore the only one that can be scanned after the assembly. Due to time constraints during the manufacturing, only a subset of the targets from different batches have been evaluated on their concave side. Nevertheless, the *field parameters* Sq and Sz obtained from the convex side allow for the same quality verification as the data obtained from the concave side in all regard but the contamination. In contrast Sdq can not be used due to the high roughness of the electroplated surface with a dominant spatial wavelength in the order of $\lambda_{Ssw} = 2\,\mu\mathrm{m}$.

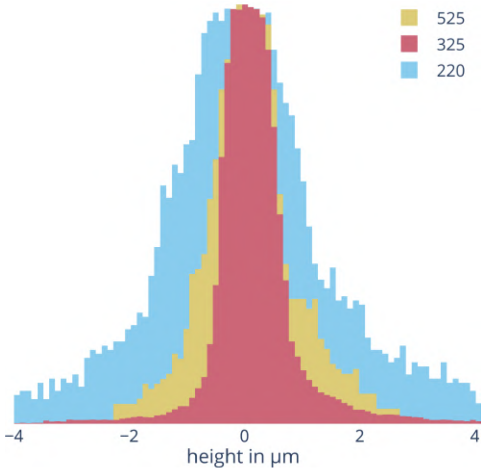

Figure 4.11: Averaged height density map, depicting the distribution of deviations from the nominal sphere. For the reasons stated in the text, the $\varnothing 220\,\mu\mathrm{m}$ targets show a wider distribution.

4.3.2 Assembly

Following the evaluation of the spherical targets shape and quality, this section discusses the assembled 5×5 sets of primary and secondary foil. The average distance of the apex relative to the carrier foil plane, denoted as $h1_P$, is required to calculate the custom depth h_6. $h1_P$ is measured for each target configuration to ensure a precise assembly by tailoring the primary mount to each batch of targets. The value changed for this, h_6, is obtained by the following calculation based on the dimensions shown in Figure 4.12:

$$h_6 = h_{6,\mathrm{AP}} - h_{1,\mathrm{P}\varnothing} - t_{\mathrm{primary}} + h_5. \tag{4.1}$$

with h_6: the thickness of the primary mount; $h_{6,\mathrm{AP}}$: nominal distance of the primary to secondary target; $h_{1,\mathrm{P}}$: laser sided averaged apex height above the foil; t_{primary}: thickness of the primary target; $h_5 = 400\,\mu\mathrm{m}$ defined base thickness. The apex-carrier foil distance has been measured to $h1P_{240} = 89\,\mu\mathrm{m}$, $h1P_{340} = 114\,\mu\mathrm{m}$ and $h1P_{540} = 205\,\mu\mathrm{m}$.
Once assembled, the distance of the laser side apex, $apex_L$, to the secondary targets rear side was measured for 150 patial sphere targets of three configurations. These measurements have been conducted using a dual confocal sensor setup with a high repeatability of $\approx 3\,\mu\mathrm{m}$. The results are shown in Figure 4.13, depicting the nominal and measured distance of six 5×5 target arrays. The bottom section displays the difference between the nominal and measured distance, revealing an average offset of $-44\,\mu\mathrm{m}$ along a standard deviation of $25\,\mu\mathrm{m}$.

This negative average offset shows that the actual distance is shorter than intended. A consistent distance of the primary and secondary targets are of great importance to minimize the error in the experimental data. For instance, the calculation of the virtual focus position is affected by this discrepancy, with the importance of the correction of $h1P$ discussed in Section 3.1.2.

The most likely causes of the deviation from the nominal distance $h_{6,AP}$ include:

- Glue intrusion: The adhesive (epoxy glue) might have intruded in between the foils and their mounts during the assembly, therefore adding an unwanted layer, pushing primary and secondary closer together.
- Machining tolerances: inaccuracies in the machining of the mounting system could result in an deviation from the nominal h_6 value

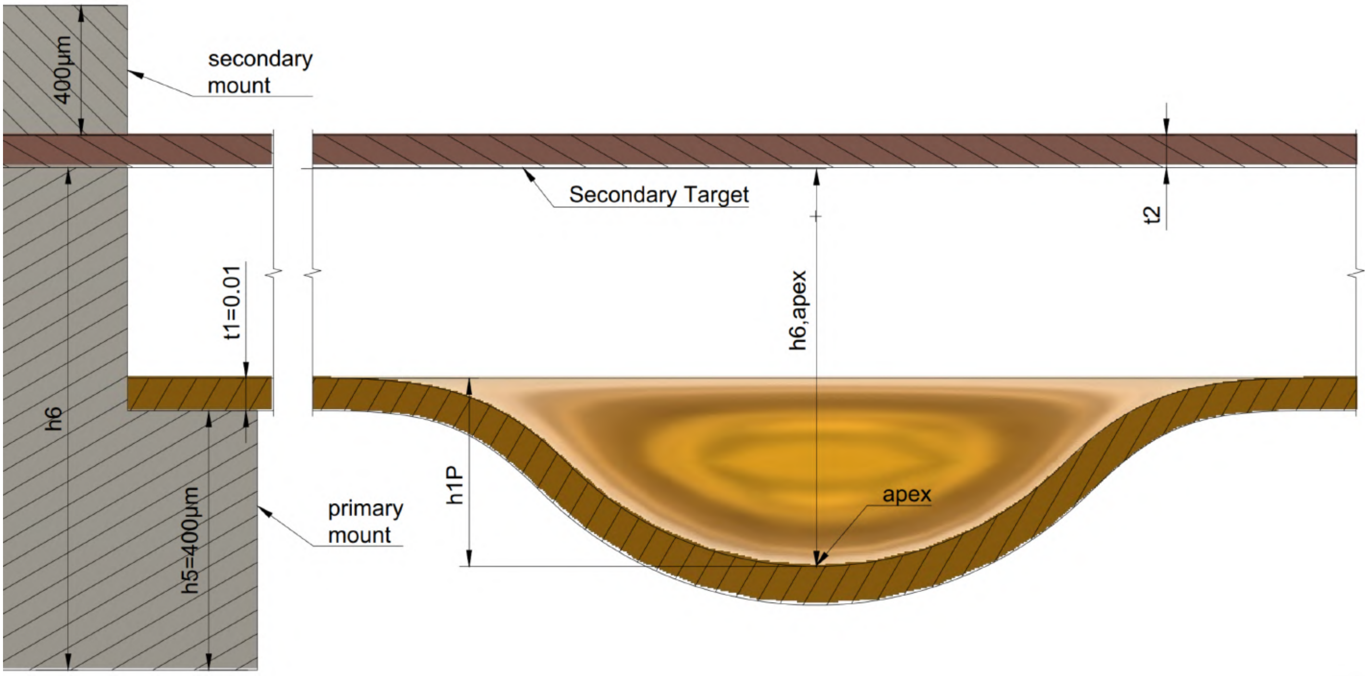

Figure 4.12: Schematic of the primary - secondary target assembly. Features are exaggerated and the dimensions are not to scale.

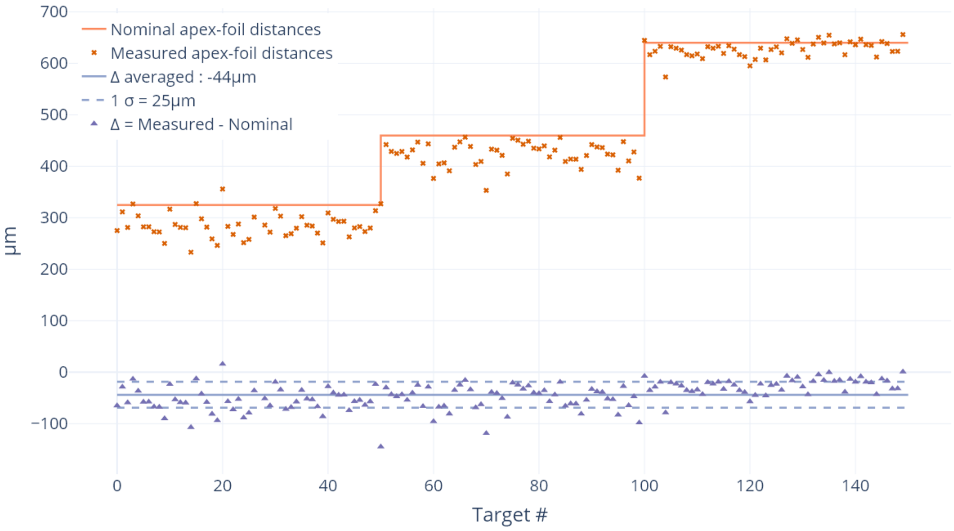

Figure 4.13: Measured distances between the laser-side apex and the secondary target's rear side for 150 targets across three configurations and six sets. The bottom plot shows the deviation between nominal and measured distances, with an average offset of $-44\,\mu\mathrm{m}$.

Issues with glue intrusion should have been prevented by using the mounts shown in Figure 4.5b, which press the secondary mount onto its foil while the glue is applied and hardens. Additionally, the mounted secondary foil extends beyond the pocket of the primary mount and is supported by the alignment studs (labeled ’F’ in Figure 4.5a), conceptually preventing the foil from moving below the top surface of the primary mount.
To ensure dimensional accuracy the depth of the pocket $h_6 - h_5$ has been manufactured to a tolerance of $10\,\mu\mathrm{m}$. Each mount had this dimension inspected at eight positions using a coordinate measurement machine.

Additionally, the primary target carrier foil may contribute to the observed deviation. After mounting the primary mount using glue mounts similar to the secondary one, there is no mechanical force applied onto this foil once it is removed from the fixture. The primary carrier foil is not completely flat, but displays some wrinkles, indicating internal stress. This stress could result from the thermal contraction of the polycarbonate after removal from the $70\,^{\circ}\mathrm{C}$ electrochemical bath, potentially resulting in the bulging of the foil.

While these factors may contribute to the discrepancy, the exact origin of the observed offset from the nominal distance cannot be pinpointed. Nonetheless, the assembled targets showed a consistent deviation from their nominal apex-secondary distance, with a standard deviation of $\sigma = 25\,\mu\mathrm{m}$. The manufacturing process followed an inline procedure, machining new mounts and forming PC on demand, which allowed for iterative improvements in the overall fabrication process. However, the apex-secondary distance $h_{6,AP}$, has only been sampled after the production of all targets and thus remains uncorrected. For future runs of similar target assemblies, it will be necessary to monitor this parameter during the production to implement corrective measures.

4.4 Target Alignment

Precise alignment of targets relative to the laser focal spot and diagnostic equipment is crucial in high-intensity laser experiments, as misalignments can significantly affect experimental outcomes. While standard alignment procedures suffice for simple targets like flat foils, the introduction of more complex targets , such as arrays of partial sphere targets with secondary components, alongside medium repetition lasers, necessitates the development of more advanced alignment methods.

A conventional scenario in the context of laser driven acceleration is the alignment of flat foils mounted in an array, possibly with a secondary target. Typically, an alignment pin is placed at the desired interaction point (IAP) to teach a camera system, which in turn allows for the adjustment of the laser to this reference position. For the alignment of the different diagnostics the laser or other light sources might be used in conjunction with the alignment pin. To not damage the camera, the beam can be attenuated or only the amplified seed laser is send through the optics.

The camera system can then be used to place a foil in the interaction point along the target plane with its depth of field providing a reference for the alignment along the laser’s axis. Once a single target is aligned the other targets can be positioned in the IAP by translating the frame by its grid spacing. Given that flat foils usually do not require precise alignment, this method is sufficient. If the Rayleigh length of the laser is comparatively large and the diagnostics also allow for it, a deviation along the laser axis in the order of hundreds of micrometers can be acceptable. Should a higher precision of alignment in this direction be required, a camera setup with a low depth of field or a confocal sensor can be used to align the target. In case of the confocal sensor, this can be done by calibrating the sensor to the IAP and then recording the deviation for all targets sequentially. During the shot sequence the axial position is corrected, greatly increasing the accuracy of the target plane, while maintaining a high target throughput.

However, when dealing with more complex targets, such as partial sphere targets with precise geometrical requirements and secondary targets, the alignment tolerance tightens considerably. Automatic, precise positioning of these targets in all three dimensions becomes critical, especially when aiming for high-repetition-rate experiments where manual alignment for each shot is impractical. To address these challenges, a new, two-step alignment procedure has been developed, consisting of high-resolution confocal scanning of all target in the laboratory reducing the time for on site alignment: After fabrication, all target- and the alignment feature coordinates are captured in relation to each other. On site, the target frame is placed in the experimental chamber and the four alignment features are located using a high magnification camera system. The coordinates from the laboratory measurement are then used to transform all target positions into the chamber system, allowing for the alignment of all 200 targets by only locating four alignment features. This method allows for a high target throughput, with a low on-site preperation time alongside a precision similar to manual alignment.

4.4.1 Concept

As previously described ins Section 4.3.1, the mapping process of the targets mounted in their frame begins using a 20x lens of a profilometer (Sensofar S-NEOX) to automatically approximate the positions of all targets. This information is then used to more precisely map the position of all targets and the alignment features using a 50x lens. The position of the targets apices for pre-alignment and precise mapping are obtained by fitting a sphere with the respective radius of the individual target to the measured surface. Here the location of the laser-side apex is obtained, which in turn allows to calculate the position of the concave side apex given the thickness of the target. The 3D mapping of all targets furthermore allows to flag targets that do not meet the desired specifications (see Section 4.3.1).

From this procedure the positions of all apices $\boldsymbol{p}_i^{\mathrm{P}}$ and alignment features are know in the coordinate system of the profilometer O_{P}.

Once on site, the position of the alignment features are measured again in the chamber coordinate system O_{C} using a high magnification camera calibrated to the interaction point. Idealized, this allows to calculate a coordinate transformation $\boldsymbol{A}_{\mathrm{C}}^{\mathrm{P}}$ from the profilometer coordinate system O_{P} to the chamber coordinate system O_{C}, allowing the calculation of the positions of all apices in the latter system (Siciliano et al., 2009):

$$\boldsymbol{p}_i^{\mathrm{C}} = \boldsymbol{A}_{\mathrm{P}}^{\mathrm{C}} \boldsymbol{p}_i^{\mathrm{P}} \tag{4.2}$$

In practice a more advanced approach is needed to find an optimal homogeneous transformation matrix $\boldsymbol{A}_0^{\mathrm{C}}$ to go from the profilometer to the chamber coordinates as the systems can have slight differences in linearity and orthogonality that need to be taken into account. The goal for the approach is to minimize the distance between the measured and transformed alignment features.

With the positions of the apices now known in the chamber coordinate $\boldsymbol{p}_i^{\mathrm{C}}$, the target can be shot consecutively without further alignment.

As the alignment process depends on the entire target assembly keeping its shape between measurement in the laboratory and shot sequences on the experimental site, special attention is required and custom solutions need to be developed for transportation as well as mounting in the experimental chamber and the stage of the profilometer.

4.4.2 Evaluation

The experimental campaign has been plagued by mechanical issues with the available motorized stages. This resulted in a greatly reduced throughput due to the need to manually position each target, the very thing this improved alignment concept aimed to prevent.

Nevertheless, once the stages where operational and adjusted, the targets could be aligned and shot by manually finding the alignment features and using the transformation software to calculate the positions of the apices, then allowing automatic placement. Due to the delays, no systematic quantitative verification of the quality of the alignment concept has been conducted on-site. Instead, after the experiment, a three axis setup similar to the one used on-site has been assembled and the capabilities of the setup have been verified.

For this, two frames, mapped prior the experiment have been placed in a three axis motorized mount. The 'interaction point' is defined by the center of a camera using a 50x lens with a field of view of $338\,\mu\text{m} \times 283\,\mu\text{m}$ and a shallow depth of field in the order of one micrometer. This camera is used to map the alignment features. Then, with the apex positions obtained from the algorithm and each target moved into the IAP, the camera is used to find the actual position of the targets apex relative to the IAP by using focus variation.

The results are depicted in Figure 4.14, showing the distance of the apex to the interaction point in the targets plane in the first row followed by the distance to the targets normal for Frame 8 and Frame 9. Frame 8 and 9 have been mapped prior the experiment, have travelled to the US and back to Germany and then, six months after, been placed in the setup used. Additionally Frame 8 has been mapped in the laboratory again and this alignment data has been used in a second test, with the data being named 'Frame 8 - post'.

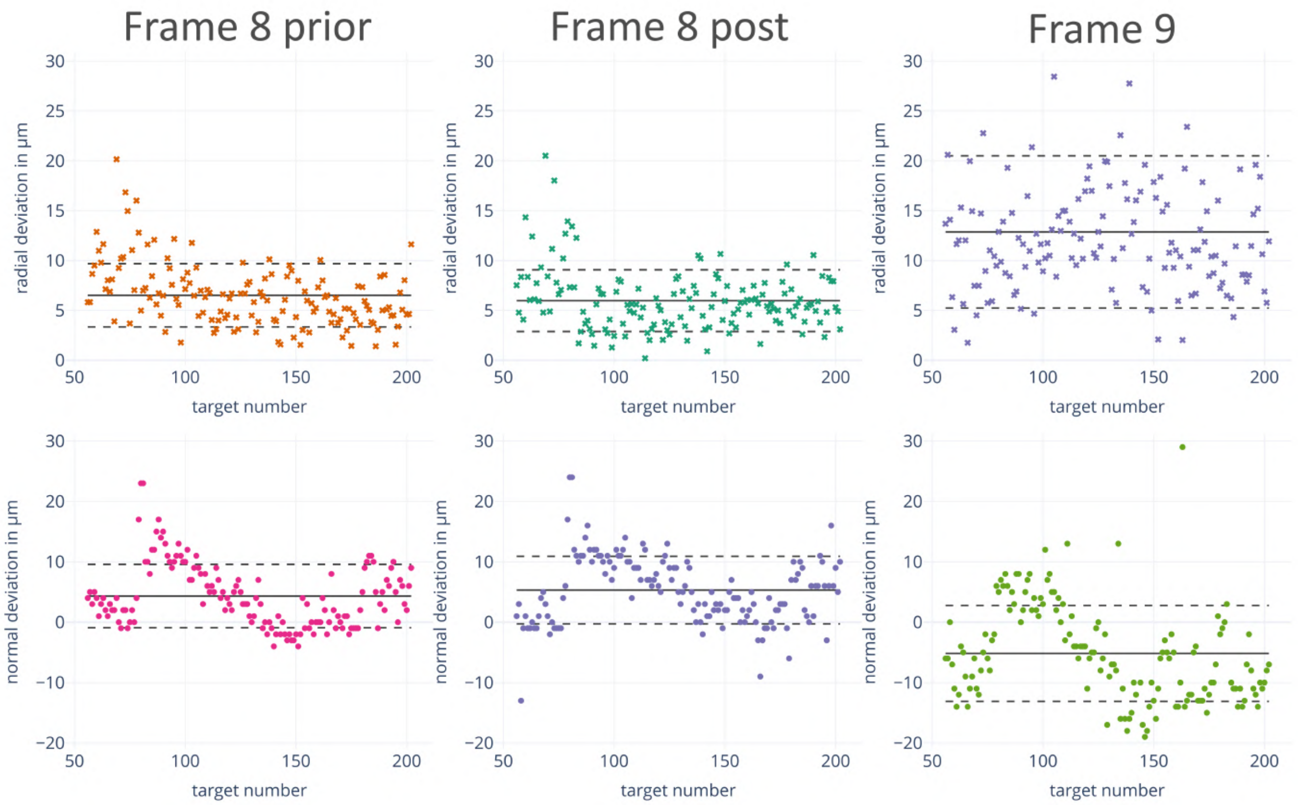

Figure 4.14: Frame 8 prior and Frame 9: Alignment measurement taken prior two transatlantic flights, 6 months prior the verification. Frame 8 post: Alignment measurement taken shortly before verification. The consistent envelope of the normal plot indicates consistent geometrical deviations in the three axis motion system. The alignment fulfilled the requirement for an accuracy of $< 20\,\mu\text{m}$.

When directly comparing the frame 8 data form the initial mapping as well as the quantification test shown

	r	σ_r	z	σ_z
Frame 8	6.0	3.1	5.3	5.6
Frame 8 post	6.5	3.2	4.3	5.2
Frame 9	12.9	7.6	-5.2	7.9

Table 4.2: Values in µm. Results from the evaluation depicted in 4.14. Further details provided in the text.

in Figure 4.14, it can be decisively concluded, that the positions of the targets as well as the alignment features have not changed their position of the course of their transportation and time.

The results, summarized in table 4.2, can be separated in two groups, the deviation within the targets plane and normal to it. Frame 8 (9) shows an average distance of the apex from the IAP in the targets plane of $r = 6.0\,\mu\text{m}(12.9\,\mu\text{m})$ with a standard deviation of $\sigma_r = 3.1\,\mu\text{m}(7.6\,\mu\text{m})$. All measurements show a constant offset in a direction (not the same) around which the values distribute. No apparent reason for the larger distribution of the radial distance values of frame 9 could be found and require further investigation.

Nevertheless, the setup fulfills the requirement of an accuracy of less than $20\,\mu\text{m}$, which equals half the laser spot size.

The second row of Figure 4.14 depicts the distance from the IAP normal to the target and shows an interesting trend: the envelope of the measured data follows the same shape for all three measurements. The most probable reason for this behaviour seems to be a pitch or yaw of at least one of the axis, which could result in a shift along the targets normal in the order of $\pm 15\,\mu\text{m}$ per motorized axis. Calculated using the maximal angular error specified for the axis used. This could be verified by repeating the measurements at a different absolute position range of the axis.

Even with the underlying shape of the data, the distribution of all points is still within $\pm 20\,\mu\text{m}$, being by far sufficient for the accuracy required by the diagnostics.

Conclusion Overall, the two-step alignment procedure combining extensive automatic pre-alignment of all targets in the laboratory, followed by minimal on-site alignment, demonstrated its viability for aligning hundreds of spherical targets. During the experimental campaign it became evident, that the success of the procedure depends on the mechanical integrity of the stages, as well as their precise alignment relative each other. Nevertheless, the method achieved an alignment accuracy within $20\,\mu\text{m}$.

During future campaigns, an automatic recognition of the alignment features on-site could boost the exchange speed between frames even further by eliminating the only manual step. Additionally, the software developed to quantify the positional error can be deployed on-site, enabling rapid verification of the entire setup, ranging from the transformation software to the motion stages. Moreover, progress has already been made transforming from the laboratory system into a system of lower quality for future campaigns, mitigating constant offsets (e.g. due to slight yaw or pitch of the axis). This can be done by either utilizing alignment features or a custom calibration target.

To summarize, this work marks the first time a large batch of partial targets has been manufactured, thoroughly characterized, and successfully aligned. This underscores the method's potential for future high-throughput laser–plasma experiments.

5 Experiment - Proton Focusing with Partial Sphere Targets

In this chapter, an experimental investigation is presented how different sizes of partial sphere targets ($\varnothing 220$ µm to 525 µm) influence the focusing and channelling of proton beams driven by high-intensity laser pulses. Two main diagnostic methods — radiochromic film (RCF) stacks combined with meshes, and foils heated by the beam and observed by a XUV imager — were used to measure the proton beam's spatial and energy distributions. The results are then compared to particle in cell (PIC) simulations, which predicts different focusing capabilities for the different sizes.

Section 5.1 details the experimental setup, describing the laser used and it's beam parameters along the two experimental and diagnostic approaches used. In the first approach RCF stacks where placed downstream along a mesh to record beam imprints, whereas the second configuration utilized foils, who's heating by the beam is observed by XUV diagnostics.

Section 5.2 describes the particle in cell (PIC) simulations preceding the campaign, which explore focussing capabilities of the different target diameters, guided by the illumination Ψ. The targets of the smallest diameter show strong focusing, while the large diameter targets show foil-like, divergent behaviour.

Section 5.3 presents the experimental data gathered by the mesh–RCF and foil–XUV setups, separated into three subsections: First the proton energy spectra and laser to proton energy conversion are obtained from the RCF data. Second, from the mesh imprint on the RCF stack, the beam's mesh-RCF magnification is calculated along the location of the 'virtual focus' by tracing the beam's path from the mesh to the RCF. Finally, the mesh–RCF as well as the foil–XUV setup allow for the investigation of the beam's size at the location of the secondary target (mesh or foil). This is then compared to the time-integrated energy density profile of the PIC simulations.

5.1 Experimental Setup

The experiment was conducted at the Colorado State University's Laboratory for Advanced Laser and Extreme Photonics (L-ALEPH), which operates a Ti:sapphire laser system capable of delivering high-intensity ultrashort pulses at a burst repetition rate of 3.3 Hz, reaching peak powers of up to 0.85 PW. The system utilizes chirped pulse amplification (CPA) (Strickland & Mourou, 1985) in conjunction with neodymium (Nd) slab amplifiers, followed by a deformable mirror and grating compressor (Wang et al., 2017).

During the experiment, the system produced 40 fs, 20 J pulses, at a wavelength of 800 nm, which were focused to a full width half maximum (FWHM) of 40 µm using a long focus f/25 off-axis parabolic mirror. With an intensity of $I \approx 3.6 \times 10^{19}\,\mathrm{W\,cm^{-2}}$ this calculates to a laser amplitude (equ 2.21) of

$$a_0 = 0.855 \times \left(\frac{I\lambda}{10^{19}\,\mathrm{W\,cm^{-2}} \cdot \mu\mathrm{m}^2} \right)^{1/2} \approx 4. \tag{5.1}$$

The beam arrives on the target at an angle of 10° relative to the normal of the partial sphere and flat targets to prevent back-scattering of the light towards its source.

Two experimental setups were employed in this campaign, each providing different insights into the proton

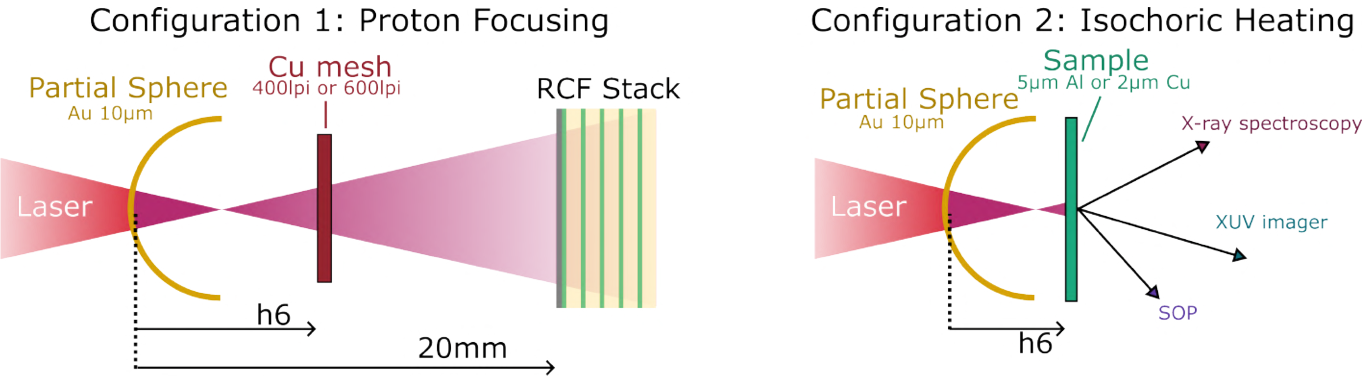

Figure 5.1: Sketches of the two configurations used in the experiment. The first configuration uses a RCF stack with a mesh to trace the proton beam. For the second configuration a foil is placed behind the target and heated by the proton beam, allowing for a direct measurement of the protons beam size.

focusing behaviour of the partial sphere targets. The first configuration, depicted in Figure 5.1, directly investigates the proton trajectories by using a mesh in between the target and radiochromic film (RCF) stack.

This setup allowed for the determination of the virtual focus position of the proton beam and provided measurements of its diameter at two distinct locations per shot. The beam passes through the grid with a known spacing, leaving an imprint on the proton beam, and therefore also on the RCF. Now the beam size can directly be measured on the RCF, but also its size when it passed through the mesh can be derived, as the grid spacing is known. Assuming a ballistic trajectory (straight line) between mesh and RCF, the magnification can be calculated. By assuming a ballistic trajectory even in front of the mesh, the virtual focusing position can be calculated, detailed in Section 3.1.2. This is the location the protons *seem* to originate from, following the purely ballistic trajectory assumption.

To maximise the amount of shots prior exchanging the RCF stack, a dedicated diagnostic replacement system has been developed. Here the RCF stack is sectioned into an array and placed on a three axis motorized stage, as previously shown in Figure 3.5. In combination with the separate target alignment system, this allowed for 20 shots without breaking vacuum or opening the chamber. Still, the RCF stack must be replaced after these 20 shots and scanned before conducting an initial fast analysis. Additionally, while $90\,\%$ of the dyeing occurs within milliseconds of irradiation, full dyeing can take up to $24\,\mathrm{h}$ (Nürnberg et al., 2009).

Both experimental setups incorporated a 2ω imager, observing the front, laser-facing side of the target to monitor pointing fluctuations for each shot, with the intention of ensuring consistent laser alignment during shot sequences.

Unlike directly tracing the protons paths, the second setup was designed to determine the proton beam diameter by measuring the heated area on a secondary sample positioned along the proton beam trajectory and utilized the following diagnostics:

- X-Ray spectroscopy: Characterisation of the sample temperature based on the temperature-dependent shift of the K_α emission.
- Extreme ultraviolet (XUV) imaging: Time integrated imaging of the XUV emission from the secondary foil, used to characterize the warm dense matter state.

- Streaked optical pyrometry: Measurement of the time dependent evolution of the temperature of the secondary foil through the acquisition of the black body emission at a specific wavelength.

All of these diagnostics are compatible with medium repetition rates in the order of $1\,\mathrm{Hz}$ as they do not need to be exchanged after a limited number of shots and provide instantaneous results, which are two major draw backs of the RCF array. They are therefore well suited for the use along with the target alignment system developed during this thesis (Section 4.4).

5.2 Focusing Dynamics of Hemispherical Targets investigated through Particle-In-Cell Simulations

In preparation to the campaign at the L-ALEPH facility, described in this thesis, a set of simulations have been performed by Dr. Valeria Ospina-Bohórquez.

The simulations were carried out for hemispheres with inner diameters (diameter of the proton emitting surface) of $100\,\mu\mathrm{m}$, $240\,\mu\mathrm{m}$, $340\,\mu\mathrm{m}$ and $540\,\mu\mathrm{m}$, with perfect opening angles of 180°. In contrast, the experimental targets used sections of spheres with an opening angle of approximately 160° and diameters of $220\,\mu\mathrm{m}$, $325\,\mu\mathrm{m}$ and $525\,\mu\mathrm{m}$. The non-ideal opening angle is inherently a result of the manufacturing procedure (Section 4.2). This slight variation in diameter and opening angle does not affect the underlying physics, and the behaviour observed in both the simulations and experiments should remain comparable. Prove of this is that, as mentioned hereinafter, the observed proton focusing dynamics remain similar in the region $240\,\mu\mathrm{m} < D_{\text{target}} < 340\,\mu\mathrm{m}$.

The simulations were conducted in a 2DV3 geometry – 2-dimensional in Cartesian space and 3-dimensional in momentum space – using the Particle in Cell (PIC) code EPOCH (Arber et al., 2015) to describe the interaction of a $0.8\,\mu\mathrm{m}$ wavelength in space and time Gaussian laser pulse with a peak intensity of $4 \times 10^{19}\,\mathrm{W\,cm^{-2}}$, focused to a $40\,\mu\mathrm{m}$ FWHM focal spot with a duration of $40\,\mathrm{fs}$, similar to the parameters of the L-ALEPH system. The simulated targets consist of a proton rich CH layer on the inner, concave side, followed by a tamper Gold layer and a preplasma, also made from gold, on the laser exposed, convex side. The latter mimics the hydrodynamic expansion initiated by the prepulse arriving ns before the main intensity peak and has a scale length of $L_n = \dfrac{\partial x}{\partial n} = 2\,\mu\mathrm{m}$.

Figure 5.2 summarizes the main results of this study. The first three rows depict the temporal evolution of the proton energy density for a $\varnothing 100\,\mu\mathrm{m}$, $\varnothing 340\,\mu\mathrm{m}$ and $\varnothing 540\,\mu\mathrm{m}$ hemispherical target, with the last row depicting a flat foil reference case. The parameter Ψ, defined as the ratio between the target diameters D_{target} and focal spot D_L diameters, characterizes the targets illumination:

$$\Psi = \frac{D_{\text{target}}}{D_{\text{L}}}. \tag{5.2}$$

The smallest target ($D_{\text{target}}, \Psi = 100\,\mu\mathrm{m},\ 2.5$) shows a good focusing capability followed be a strong divergence of the proton beam. Intermediate diameter targets ($D_{\text{target}}, \Psi = 240\,\mu\mathrm{m},\ 6.0$) and ($D_{\text{target}}, \Psi = 340\,\mu\mathrm{m},\ 8.5$) show moderate focusing, characterized by a proton channelling effect. In these simulations, the proton beam remains collimated beyond its maximum convergence point at $x \sim 280\,\mu\mathrm{m}$. Such collimation extends over a distance equal to the hemisphere's radius and is indicated by the red arrow in Figure 5.2. Finally, targets with a large diameter ($D_{\text{target}}, \Psi = 540\,\mu\mathrm{m},\ 13.5$), exhibit a behaviour relatable to flat foils: no focusing is observed and the proton dynamics are comparable to the acceleration from a flat foil.

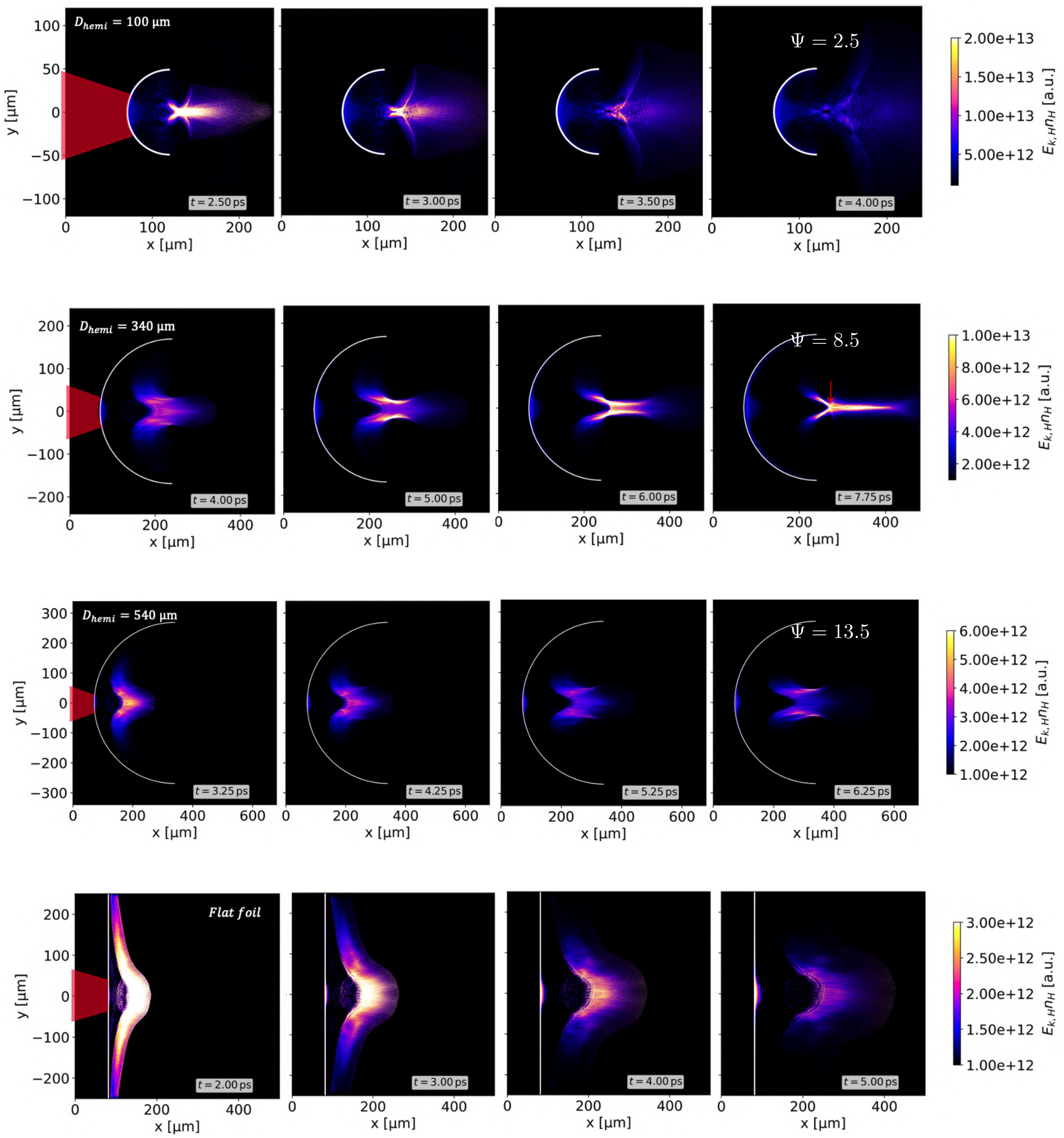

Figure 5.2: Proton energy density maps extracted at different time steps for three different target diameters compared with a flat foil. First row: $D_{\text{target}} = 100\,\mu\text{m}$, second row: $D_{\text{target}} = 340\,\mu\text{m}$, third row: $D_{\text{target}} = 540\,\mu\text{m}$ and fourth row: flat foil. The white curved and vertical lines indicate the original location of the proton-rich layer. The red laser cartoon in the left column is drawn at scale. Notice that in all cases the laser focal spot is equal to $40\,\mu\text{m}$ (FWHM). Simulations by Dr. V. Ospina-Bohórquez.

5.3 Proton Beam Measurements using Radiochromic Film Stacks

In the first configuration of this experiment, depicted in Figure 5.1, a stack of Radiochromic Film (RCF), consisting of five layers of HD-V2 (Ashland, 2021), has been used as the main diagnostic. The RCF stack allows for a spacial and energy resolved measurement of the proton beam. It was placed 20 mm away from the apex of the target, as depicted in Figure 5.1. In the following Section 5.3.1 the measurements from 50 shots are evaluated, consisting of three different target diameters and the flat reference targets.

By adding a mesh in between the apex and the RCF stack, the diameter of the beam at the position of the mesh and the RCF stack can be determined. Allowing for the calculation of the quotient between the grid spacing measured on the RCF, g_{RCF}, and the mesh's grid spacing, g_{mesh}, resulting in the magnification M (equ. 3.1). Assuming a purely ballistic trajectory between the mesh and RCF, the location of the *apparent* point source of the beam can be calculated. This location is called virtual focus position. Both, the magnification and virtual focus position, are calculated in Section 5.3.2.

By measuring the beam diameter on the RCF stack, the beam's size at the location of the mesh can be obtained, as the magnification is already known. Section 5.3.3 also utilizes measurements of the proton beam's size, obtained by using the second configuration. Here a foil has been placed at a known distance behind the apex of the partial sphere (Figure 5.1). When the protons arrive at this foil, it is heated locally to several eV, which is observed using an XUV camera. Both of these measurements are then compared with simulations.

5.3.1 Energy Conversion and Energy Distribution

To obtain an energy spectra of the proton beam, additional shots without a mesh where conducted with the amount of usable shots listed in Table 5.1. The single RCF sheets where digitally processed using computer vision algorithms and evaluated using the pyRES software package (Schmitz et al., 2024). As no calibration data has been obtained for the RCF, a calibration data set from a separate batch of HD-V2 film has been used. Furthermore on some of the data sets, the proton beam is locally attenuated by the alignment notches or is cut off, extending further than the section of the RCF. An example can be seen in Figure 5.3. Both of these effects result in a lower detected dose or spatial size. A selection of shots is depicted in Figure 5.4, representative of the proton spectrum of its target type. An average laser energy to proton conversion efficiency of 0.26 % has been measured at an average laser energy of 19.6 J across the 19 shots without a mesh listed in Table 5.1, with a maximum of 0.43 % at 20.3 J. No statistically significant difference in conversion efficiency between the different target geometries has been observed.

	Flat	∅220 µm	∅325 µm	∅525 µm
no mesh	3	4	8	4
mesh	2	6	19	4

Table 5.1: Number of shots evaluated with the RCF as its main diagnostic.

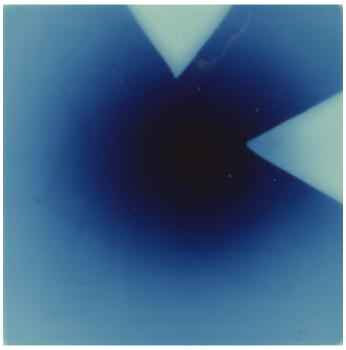

Figure 5.3: $1.5\,\mathrm{MeV}$ protons from a $\varnothing 525\,\mathrm{\mu m}$ target. The proton beam nearly extends to the edges of the section and displays the attenuation of the alignment notches. Both effects reduce the proton count.

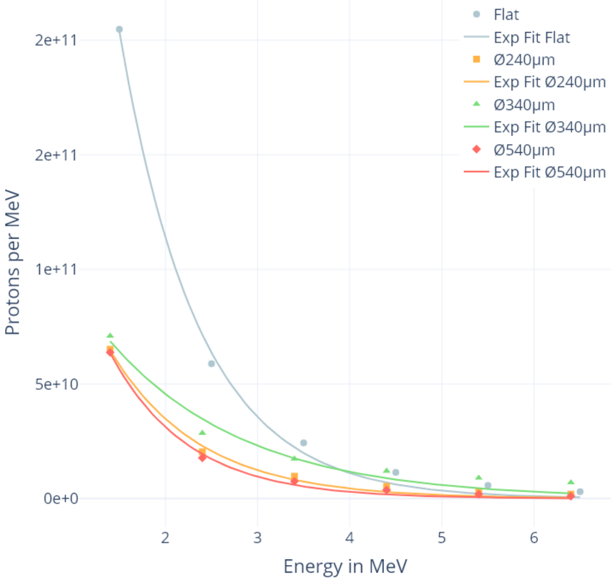

Figure 5.4: Example of the number of protons per unit energy for different primary targets.

5.3.2 Magnification and Virtual Focus Position

To obtain information about the beam's divergence and focusing, a mesh with a precise grid spacing of $42\,\mu m$ or $63.5\,\mu m$ has been placed at distances between $h_6 = 320\,\mu m$ to $960\,\mu m$ downstream the target's concave apex, followed by an RCF stack $20\,mm$ away (Figure 5.1). This results in the shadow of the mesh being imprinted into beam and therefore RCF. Assuming a ballistic trajectory, the rays can be traced back and the location of the smallest diameter can be calculated. Additionally, the magnification M, between the grid spacing of the mesh and the imprinted shadow can be calculated. Again assuming a ballistic trajectory, the location of the point source where the protons *seem* to originate from can be calculated. These methods are outlined in detail in Section 3.1.2 and were first poineered by Offermann (Offermann et al., 2011) and Bartal (T. J. Bartal, 2012).

Both techniques yield consistent results within the margin of error, confirming their reliability. Notably, the flat reference targets indicate that the virtual focus is located on the laser-facing side of the foil, in agreement with the theoretical expectations for Target Normal Sheath Acceleration (TNSA):

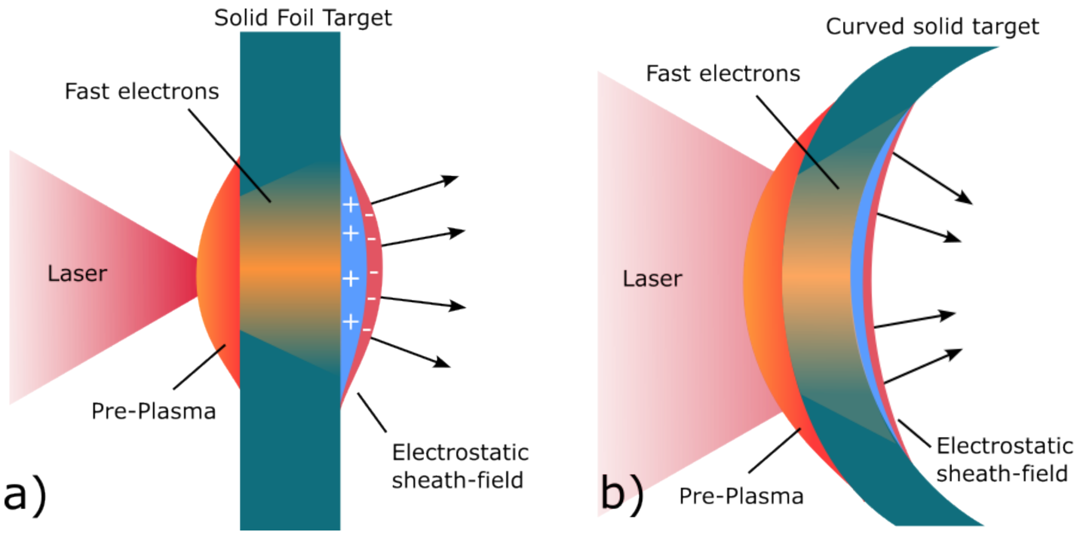

Figure 5.5: Sketch of a the sheath field accelerating protons from the targets surface. (a) The protons accelerated from the flat foil show divergent behaviour due the non planar sheath field. At the center the the field is the strongest and accelerates protons to higher energies, resulting in a lower divergence for higher energy protons. (b) The gaussian shaped sheath field is superimposed with the geometrical shape of the target, effectively resulting in a focussing for well illuminated targets ($\Psi < 6$). Based on (Higginson, 2018).

Once the laser drives the electrons through the thin target of $10\,\mu m$, the first hot electrons escape the targets rear surface, after which a sheath forms, accelerating the protons. A simplified picture of the proton focusing dynamics for flat and curved targets is sketched in Figure 5.5. An estimation for the initial size of the sheath D_S involves the target thickness l and laser spot diameter D_L and is given by (Daido et al., 2012)

$$D_S = D_L + 2l \tan\,\Theta.$$

Experimentally Θ has been measured to a value of 8° to 25° for thin targets, where the electron scattering does not strongly increase the size of the sheath (Roth & Schollmeier, 2016).

This sheath initially inherits the intensity distribution of the laser beam, resulting in the electric field following the Gaussian shape, accelerating protons normal to its density contours (Fuchs et al., 2003; M. S. Schollmeier, 2009).

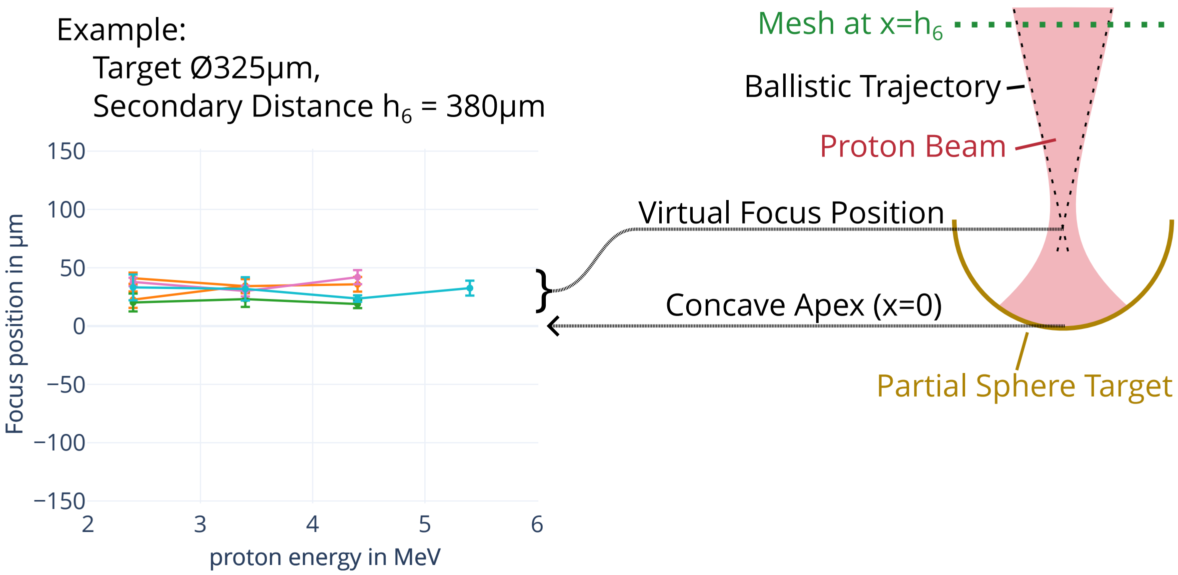

Figure 5.6: Explanatory sketch for the experiential results presented in Figure 5.7. The proton emitting, concave side of the partial sphere target references $x = 0$, with the mesh positioned at $x = 320\,\mu\text{m}$ to $960\,\mu\text{m}$.

Flat Foil Targets Therefore, protons accelerated further away from the central axis show a broader angular distribution at lower energies. This angular distribution of particles emerging from an extended surface results in virtual focus in front ($x < 0$) of a flat foil target, as seen in the first row of Figure 5.7, with a virtual focus positions at $90\,\mu\text{m}$ to $140\,\mu\text{m}$ in front of the foil (towards the laser). This behaviour stays consistent across all energies measured. Tracing back the $3.5\,\text{MeV}$ beam with a FWHM size of $700\,\mu\text{m}$ imprinted on the RCF through the mesh placed at $336\,\mu\text{m}$ to its virtual source yields a source size of approximate $38\,\mu\text{m}$, assuming a purely ballistic trajectory, in line with the size of the laser beam FWHM focal spot diameter of $\varnothing 40\,\mu\text{m}$.

Partial Sphere Targets When transitioning to spherical targets, the Gaussian sheath field is superimposed with the curvature of the targets rear surface (Roth & Schollmeier, 2016). For well-illuminated targets, characterized by $\Psi < 6$ this results in electric fields normal to the curvature along most of the targets rear surface (Figure 5.5 b)). In a simplified view, the protons are accelerated towards the geometric center of the sphere, intersecting and diverging, also shown in the first row of the simulations depicted in Figure 5.2.

For intermediate-illuminated spherical targets with $6 < \Psi < 8.5$ the electric fields are still mostly normal to the curvature. Protons are only accelerated from the area around the laser spot, resulting in a trajectory towards the geometrical center, without intersections. The resulting beam exhibits channelling beyond the partial sphere's geometrical center.

Finally, poorly illuminated targets, characterized by $\Psi > 8.5$ transition towards foil like behaviour, with a lower focusing effect.

This foil like behaviour can be observed in the fourth row of figure 5.7, depicting the virtual focus positions of $\varnothing 525\,\mu\text{m}$ partial sphere targets ($\Psi \approx 13$), showing 3 out of 4 measurements with a focal position in front of the apex ($x < 0$).

The measurements resulting from shots on $\varnothing 325\,\mu\text{m}$, $\Psi \approx 8$, show a virtual focus in between the apex and geometrical center for all secondary distances indicating the behaviour expected from a channelling of the protons.

Targets with a diameter of $220\,\mu\text{m}$ ($\Psi \approx 5.5$) show a virtual focus at the apex $x = 0\,\mu\text{m}$ for a mesh distance of $320\,\mu\text{m}$. For the mesh distances $640\,\mu\text{m}$ and $1000\,\mu\text{m}$, the virtual focus is close the apex ($x = 0\,\mu\text{m}$ to $70\,\mu\text{m}$. The shot in with a virtual focus position of $x \approx -75\,\mu\text{m}$ can probably be contributed to a miss of the sphere resulting in a shot on the surrounding foil.

Discussion The measurements presented Figure 5.7 show no data for proton energies $< 2.4\,\text{MeV}$, because the first layer of the RCF had a very non-uniform mesh imprint or was saturated.

Across different mesh distances, the virtual focus position does not exhibit any significant change. This observation indicates that the proton beam follows a ballistic, straight line trajectory by the time it reaches the first mesh at $x = 320\,\mu\text{m}$ to $340\,\mu\text{m}$ behind the apex. In addition, due to the relatively large spacing between the mesh and RCF, at the relatively small solid angle the beam covers, any radial distortion in the mesh image is negligible. Would the beam expand in a hyperbolically, i.e. with an increasing angular distribution, then a shift of the virtual focus away from the apex would be expected.

Similarly, the virtual focus position remains constant over the entire energy range of $2.4\,\text{MeV}$ to $5.4\,\text{MeV}$. This result implies that the protons' direction at the mesh is dependent on the distance from the central beam axis, but not on their energy (within the measured energy range). However, the total number of protons passing through each position of the mesh still depends on the energy, since higher energy protons follow a smaller beam diameter, i.e. a lower solid angle.

Lastly, if protons emerged purely normal to the surface of the partial sphere, crossing the geometric center, a virtual focus at that center could be observed. As the data shows otherwise, the beam must deviate from purely normal incidence, affirming non-ballistic behaviour earlier than the mesh.

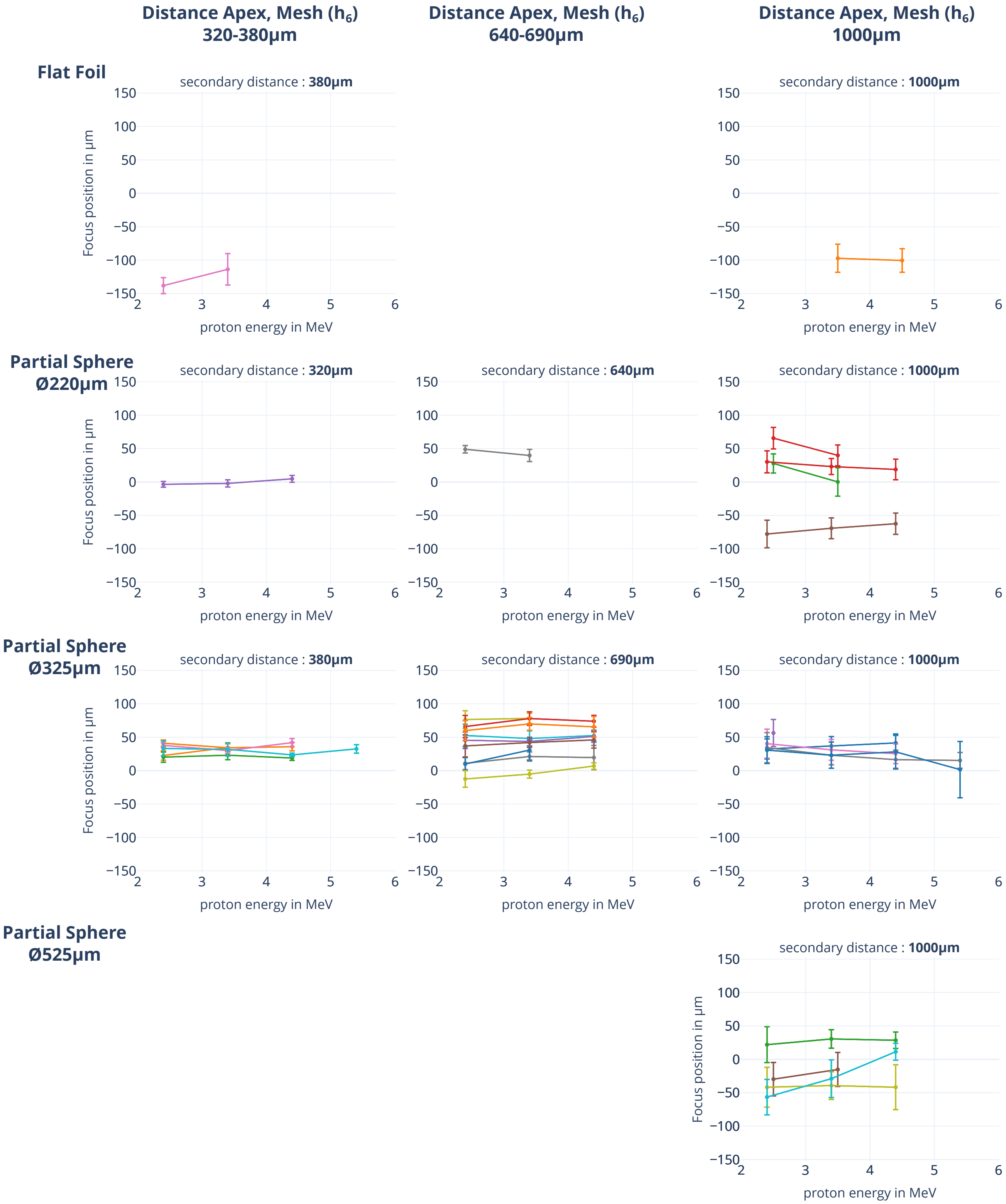

Figure 5.7: Virtual focus positions for the different target configurations. Grouped in four rows for the different primary types and three columns for different mesh distances. Foils show a virtual focus position in front of the target. $\varnothing 525\,\mu\mathrm{m}$ targets show a foil-like behaviour. Measurements from the $\varnothing 325\,\mu\mathrm{m}$ targets are consistently behind ($x > 0$) the apex. Explanatory graphic in Figure 5.6.

5.3.3 Proton Beam Size Determination and Comparison with Numerical Data

Both of the experimental configurations previously discussed (Figure 5.1) — a secondary mesh with a RCF stack and a secondary foil utilizing a XUV imager — are used to obtain the size of the proton beam at the location of the secondary target. In the first configuration a mesh with a well known grid spacing of $g_{\text{mesh}} = 42\,\mu\text{m}$ or $g_{\text{mesh}} = 63.5\,\mu\text{m}$ is placed at a distance of $h_6 = 320\,\mu\text{m}$ to $960\,\mu\text{m}$ behind the the target's concave apex, followed by a RCF stack $20\,\text{mm}$ away (Figure 5.1). This results in the shadow of the mesh being imprinted into the beam and therefore RCF.

By measuring the grid spacing on the RCF, g_{RCF}, the magnification $M = g_{\text{RCF}}/g_{\text{mesh}}$ can be calculated. Additionally, the beams size on the RCF can be estimated by fitting a 2D Gaussian distribution on the deposited dose measured from each RCF of the stack. Then, the beam size at the location of the mesh can then be derived, by dividing the RCF beam size by the magnification. For an extensive description of the calculation refer to Section 3.1.2.

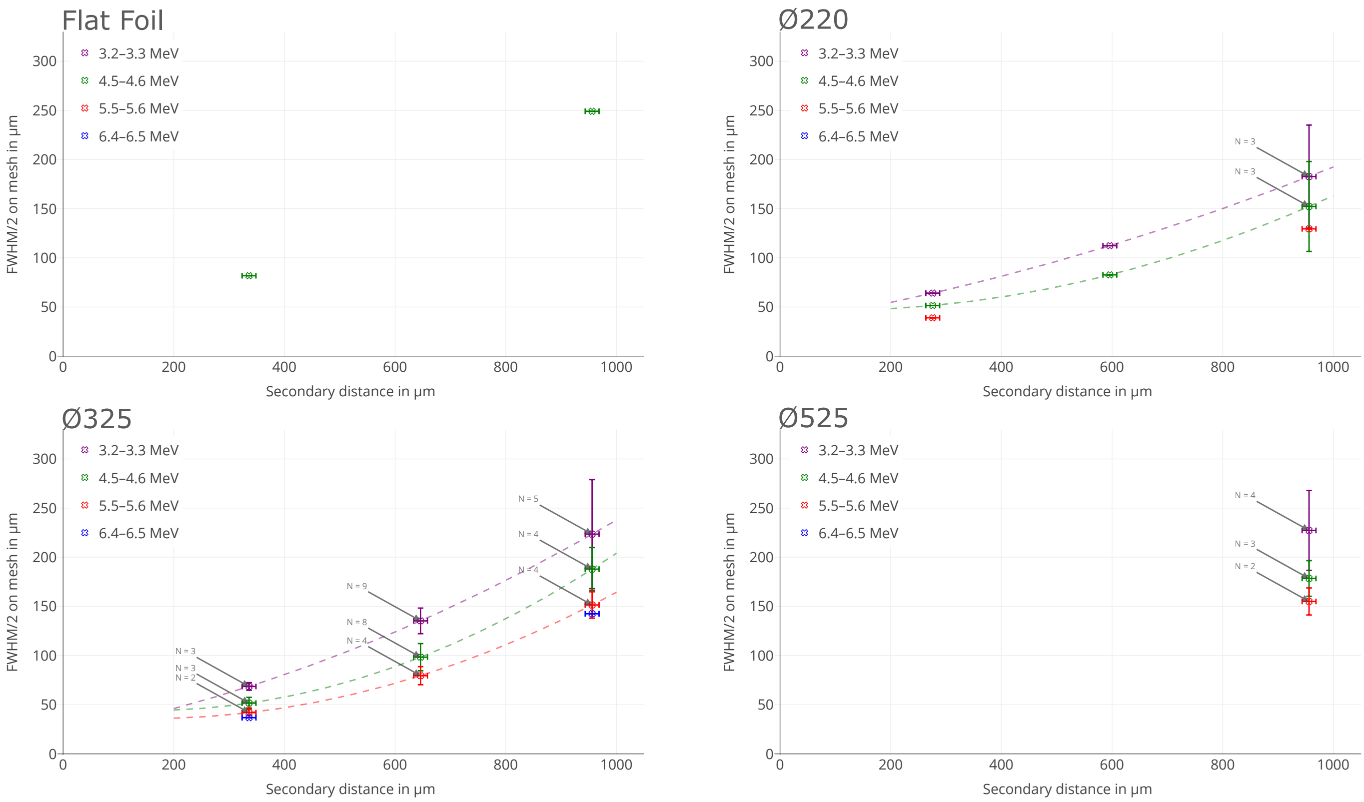

Figure 5.8: Full width at half maximum beam size at the mesh location. Data points labeled with $N = \#$ represent averages over multiple shots and the dashed lines indicate a quadratic fit for each energy. Note that the axis are not scaled equally, possibly altering the visual impression of the data.

The results of these calculations are depicted in Figure 5.8. The FWHM beam size measurements are separated by the primary, secondary (mesh) distance and energy range. The beam size results obtained from flat foil targets are consistently larger when compared to the partial sphere targets at the same energy and secondary distance, indicating a higher divergence due to the lack of any channelling or focusing effects.

Moreover, while the beam sizes at the short distances $x \sim 300\,\mu\text{m}$ of the $\varnothing 220\,\mu\text{m}$ and $\varnothing 325\,\mu\text{m}$ targets are

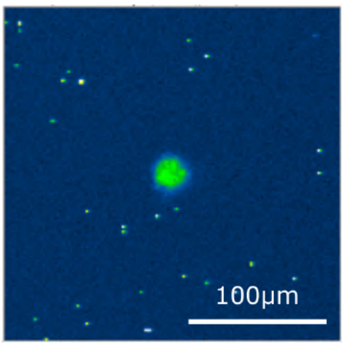

Figure 5.9: XUV image from a copper foil ($2\,\mu\mathrm{m}$) heated by the proton beam $160\,\mu\mathrm{m}$ downstream the apex of a $\varnothing 220\,\mu\mathrm{m}$ partial sphere.

similar, the beam diameters of the $\varnothing 220\,\mu\mathrm{m}$ targets are smaller for the medium ($x \sim 600\,\mu\mathrm{m}$) and far distances ($x \sim 900\,\mu\mathrm{m}$). Including the even larger expansion of the $\varnothing 525\,\mu\mathrm{m}$ target's beam at $x \sim 950\,\mu\mathrm{m}$, This indicates a beam of a lower divergence or stronger collimation for a higher illumination Ψ, as expected by the simulations.

In a second experimental configuration, secondary samples made from $2\,\mu\mathrm{m}$ copper or $5\,\mu\mathrm{m}$ Aluminium were placed behind the target. Here the proton beam heats these targets dependent of the local flux and energy distribution. The resulting thermal emission is then observed utilizing an XUV imager at $13.5\,\mathrm{nm}$ ($\sim 91\,\mathrm{eV}$), providing a direct measurement of the central part of the proton beam with the highest proton flux. Utilizing hydrodynamic simulations and assuming blackbody emission, the temperature of the sample can then be estimated.

An image from the XUV-imager, detecting the heating of a $2\,\mu\mathrm{m}$ copper foil $160\,\mu\mathrm{m}$ downstream the apex of a $\varnothing 220\,\mu\mathrm{m}$ partial sphere is shown in Figure 5.9. For this distance a spot size of $\sim 20\,\mu\mathrm{m}$ FWHM is measured at an average temperature of $T_{avg} \approx 10\,\mathrm{eV}$. At distances of $x = 320\,\mu\mathrm{m}$ from the $\varnothing 220\,\mu\mathrm{m}$ apex, the measured FWHM of the signal also averages $\sim 20\,\mu\mathrm{m}$ at a lower temperature of $T_{avg} \approx 7\,\mathrm{eV}$, indicating a beam collimation over a long distance. Similarly the secondary foils heated at $x = 230\,\mu\mathrm{m}$ from a $\varnothing 325\,\mu\mathrm{m}$ partial sphere measure a spot size diameter of $\sim 20\,\mu\mathrm{m}$ with a temperature of $T_{avg} \approx 12\,\mathrm{eV}$. This spot size presents an upper limit on the actual size of the thermal emission from the proton heating due to aberration in the optical system. With a flat foil as the primary target, no heating could be observed with the XUV imager, indicating a temperature of $< 5\,\mathrm{eV}$.

To compare the experimental data with the PIC simulations, the proton energy density has been integrated in time. The proton energy density diagnostic in a PIC simulation provides insight into the spatial and temporal distribution of energy carried by protons during the laser-plasma interaction. The proton energy density in 3D Cartesian space $E_k n(x,y,z,t)$ is defined as the total kinetic energy of protons per unit volume at a given spatial position and time multiplied by the particles weight W_i. For a proton of mass m_p and velocity $|\mathbf{v}| = \sqrt{v_x^2 + v_y^2 + v_z^2}$, the proton energy density integrated in time is

$$\int_0^T E_k n(x,y,z,t)dt = \int_0^T \sum_i \frac{1}{2} m_p |\mathbf{v}|^2 \cdot W_i dt, \tag{5.3}$$

with the simulations temporal duration T. The sum runs over all particles i present in the simulation box. The simulations were conducted in 2D Cartesian space geometry. Particles propagate along the x-axis. To obtain numerical profiles that can be compared to the experimental estimates of the proton beam diameter, Equation 5.3 must be integrated along y. Accounting for the limited 2D geometry of the simulation:

$$\int_0^T \int_{-\infty}^{\infty} E_k n(x,y,t) dy dt = \int_0^T \int_{-\infty}^{\infty} \sum_i \frac{1}{2} m_p |\mathbf{v}|^2 \cdot W_i dy dt. \tag{5.4}$$

Specifically, the XUV data will be compared with $D50$ profiles and the RCF data with $D80$ profiles, defined as the transverse coordinates encompassing $50\,\%$ and $80\,\%$ of the total proton energy. For simplicity the calculations are made over the upper half of the simulation box and symmetry around the $y = 0$ axis is assumed:

$$\begin{aligned} \int_0^T \int_0^{R50} E_k n(x,y,t) \mathrm{d}y \mathrm{d}t = 0.5 \int_0^T \int_0^{\infty} E_k n(x,y,t) \mathrm{d}y \mathrm{d}t, \\ D50 = 2 \cdot R50, \end{aligned} \tag{5.5}$$

$$\begin{aligned} \int_0^T \int_0^{R80} E_k n(x,y,t) \mathrm{d}y \mathrm{d}t = 0.8 \int_0^T \int_0^{\infty} E_k n(x,y,t) \mathrm{d}y \mathrm{d}t, \\ D80 = 2 \cdot R80. \end{aligned} \tag{5.6}$$

The XUV diagnostic is inherently sensitive to the central region of the proton beam, where the particle flux is higher, leading to an increased heating of the sample. Therefore it is compared to the numerical $D50$ profiles, which identify the beam's high energy and high density regions concentrated around the propagation axis $y = 0$. In contrast, with its high dynamic range, the RCF captures both, the high density central, as well as the low density outer part of the proton beam. Therefore, a comparison with the $D80$ profiles, which encompass a larger portion of the proton energy density, is more adequate. Both, XUV and RCF diagnostic integrate the total proton dose over time. To ensure consistency, the numerical profiles are also time-integrated.
Figures 5.10 a,c (b,d) correspond to the PIC proton energy density distributions integrated in time for the $240\,\mu\mathrm{m}$ ($340\,\mu\mathrm{m}$) sphere extracted $8\,\mathrm{ps}$ after the entrance of the laser pulse through the left simulation boundary. The top row corresponds to the $D50$ profiles and the bottom row to the $D80$ profiles. As can be clearly observed, the $D50$ profiles are narrower and remain collimated for a longer spatial extent in comparison with the $D80$ profiles. Note that Figure 5.10 a-d are plotted using a logarithmic scale: although the color scale extents through all the simulation box, most of the proton energy density is located in the focused central beam around $y = 0$.

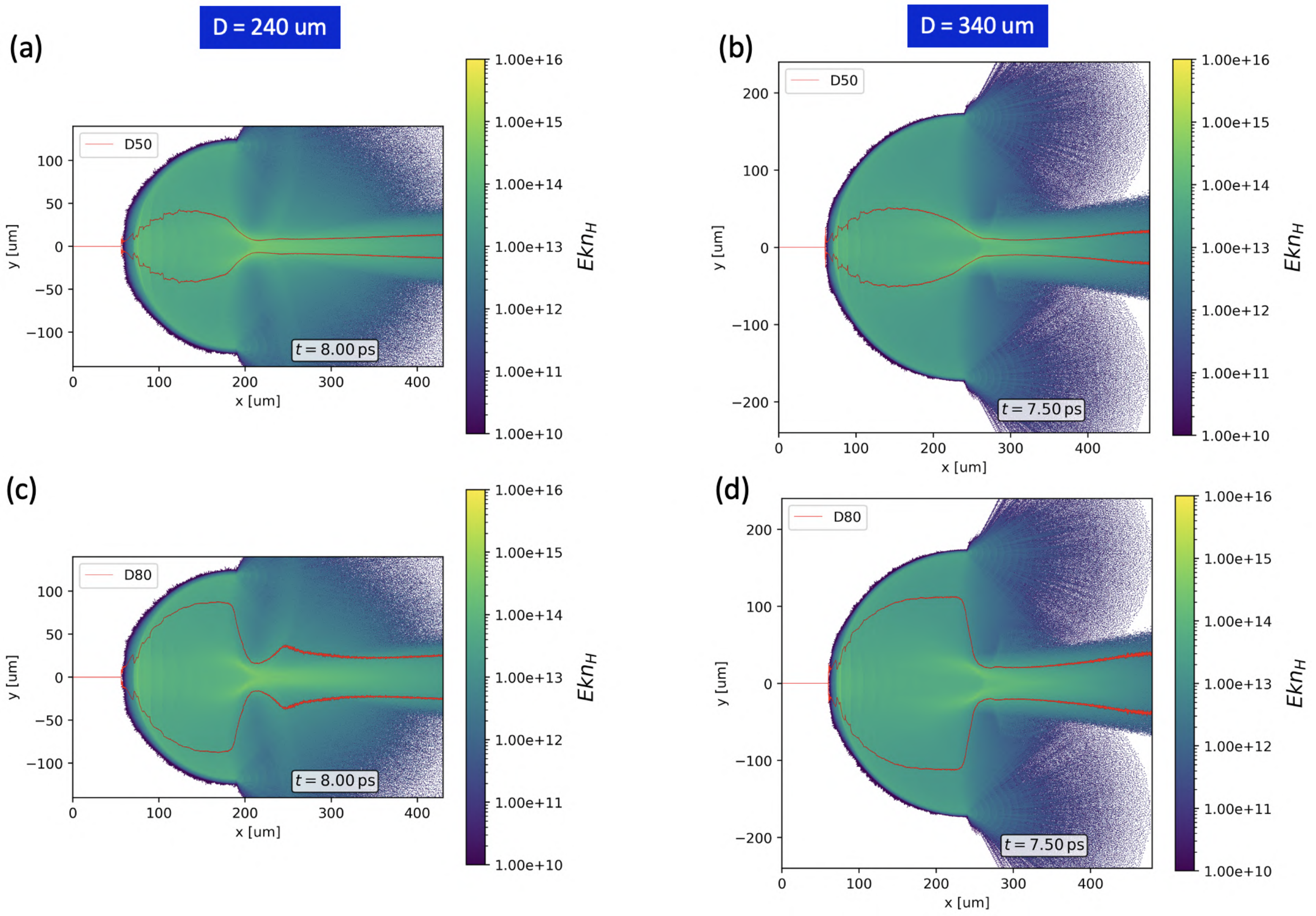

Figure 5.10: Proton energy density charts (in arbitrary units) extracted from PIC simulations $8\,\mathrm{ps}$ after the entrance of the laser pulse through the left simulation boundary and corresponding to $D_{\text{target}} = 240\,\mu\mathrm{m}$ (left column) and $D_{\text{target}} = 340\,\mu\mathrm{m}$ (right column). The top row corresponds to $D50$ profiles and the bottom row to $D80$ ones.

Figure 5.11 compares the experimental data obtained from the XUV imager with the $D50$ profiles extracted from the PIC simulations (shown in blue). The experimental data is presented as the yellow ellipses at the secondary location and corresponds in size to the measured data. This data presents an upper limit for the actual diameter of the proton beam. A more precise retrieval of the beam diameter requires forward modelling of the energy deposition and sample heating. Ongoing work couples the PIC simulation results to the hybrid code PETRA (Honrubia et al., 2009), to estimate these. Nevertheless, the extended collimation of the proton beam predicted by the PIC simulation was experimentally validated by the two heating spots recorded at $118\,\mu\mathrm{m}$ and $278\,\mu\mathrm{m}$ behind the target's apex.

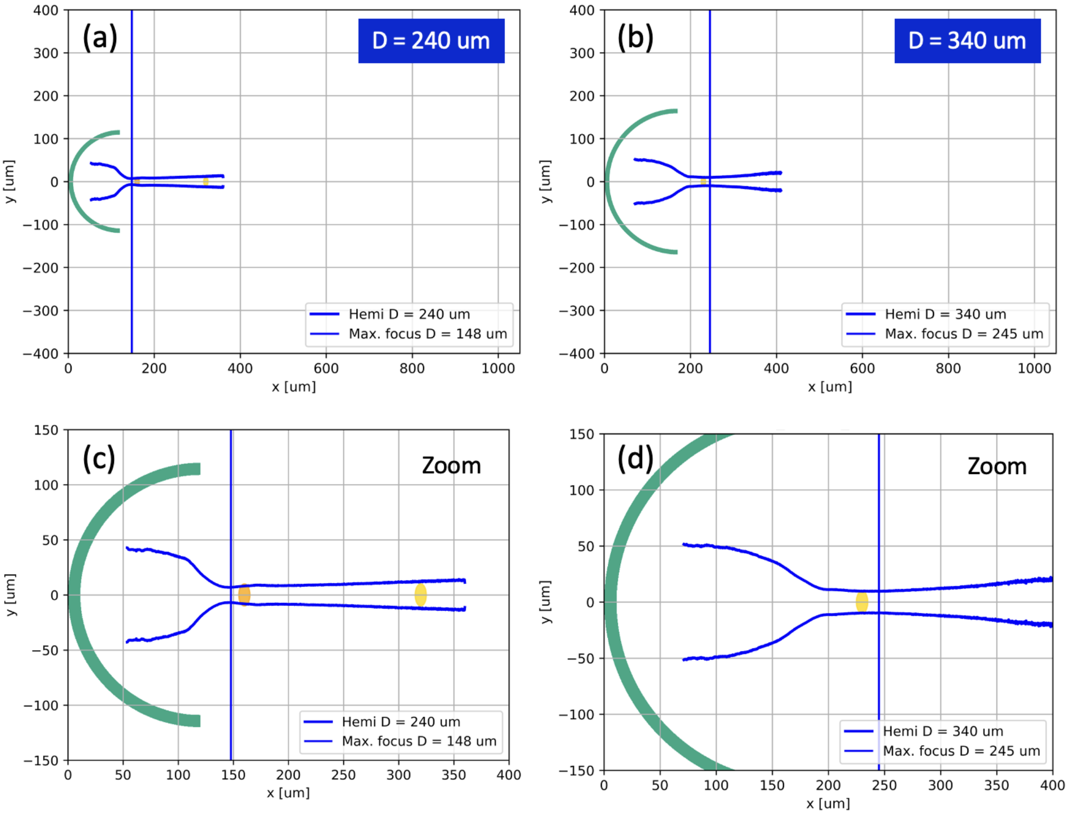

Figure 5.11: XUV experimental data (yellow ellipses) compared with $D50$ profiles extracted from PIC simulations (dark blue curves).

Figure 5.12 compares the RCF experimental data with the $D80$ profiles extracted from the PIC simulations. The $D80$ profiles (black) show good agreement with the RCF data for the $\varnothing 240$ µm and $\varnothing 340$ µm when using a parabolic extrapolation constrained at the vertex of the parabola. A linear fit matches the $\varnothing 540$ µm profiles better. The data extrapolation is required due to the spacial limitations of the simulation box. The linear trajectory of the $\varnothing 540$ µm hemisphere is linked to the flat-foil-like behaviour previously discussed in Section 5.2. Here the relatively small illumination of the sphere leads to protons being accelerated without taking profit of the focusing from the outer parts of the hemisphere, since the spacial extension of the accelerating sheath does not extend far enough. Therefore, no strong focusing is observed and the beam diverges in a similar manner to the acceleration from a flat foil.

The PIC energy density charts encompass all proton energies, making it unfeasible to directly compare them with the beam diameters of the different proton energies measured by the RCF stack, represented by the colored dots in Figure 5.12. Here it can also be observed that protons of higher energy result in a smaller beam diameter on the RCF, as a result of their inherent lower divergence (Daido et al., 2012).

For a more detailed comparison, future analysis could compute proton energy density maps discretized in energy and correlate them with the beam diameters measured at the given positions.

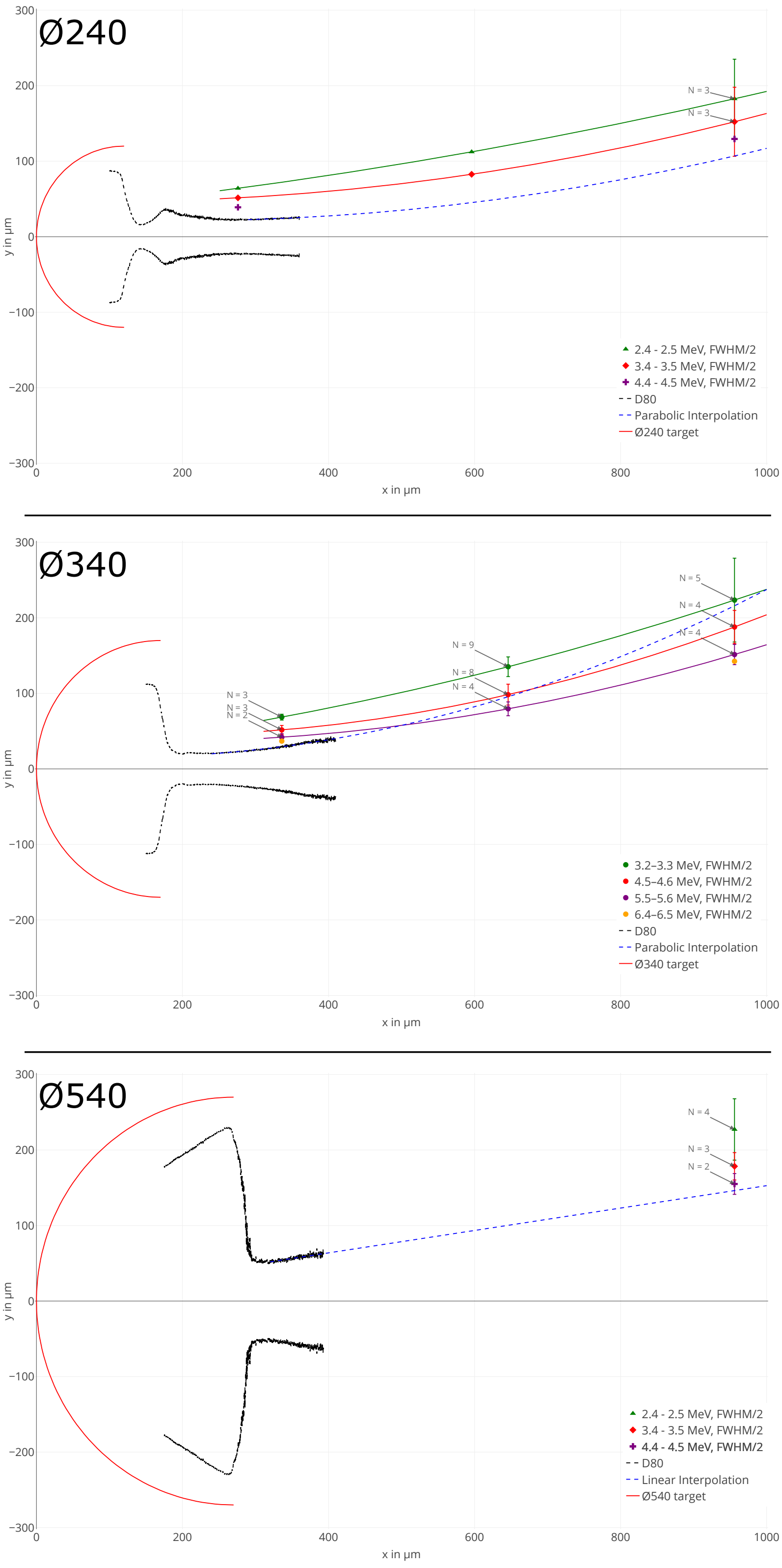

Figure 5.12: Comparison between the *D80* profiles (black curves) and the beam size on the mesh, as obtained by measuring the beam size in the RCF and accounting for the system's magnification. The blue dashed lines follow a parabolic ($\varnothing 240\,\mu\mathrm{m}$, $\varnothing 340\,\mu\mathrm{m}$) and linear ($\varnothing 540\,\mu\mathrm{m}$) extension of the *D80* profiles. Solid curves follow a quadratic fit through all data points of the corresponding energy.

6 Outlook

Over the course of this thesis, the first large-scale batch of partial sphere targets, 1050 in total, was fabricated and deployed in a single experimental campaign to deepen the understanding of focusing of laser driven proton beams for Proton Fast Ignition (PFI). Past studies researching the focussing of TNSA proton beams often relied on tens of shots in best conditions, limiting the statistical evaluation and preventing broad parametric scans. In contrast, the 320 shots taken in this campaign – enabled by a first-of-its-kind advanced and rapid alignment – significantly expanded the exploration of target geometries and diagnostic methods. This unprecedented effort included 42 distinct target configurations, surpassing all previous studies.

Target Fabrication and Metrology A batch fabrication method for arrays of partial sphere targets was established and utilized for the production of 1050 targets. Along with their secondary foils or meshes, each target was thoroughly characterized, verifying the quality and consistency of both, individual partial sphere targets as well as the assembly as a whole. Employing a coordinate measurement machine, a confocal scanning profilometer and confocal sensors, the verification of the partial sphere targets included, besides others, the thickness, opening angle and the distance between the carrier foil and apex, which has been accounted for during the assembly with the secondary targets. Furthermore, deviations from a perfect spherical shape were quantified utilizing ISO 25178 [1] ensuring consistent quality, especially on the proton emitting central region. With the targets fully assembled, the accuracy of the distance between the apices of the partial spheres and their secondary targets has been evaluated, enabling a correction from the nominal distance for a more precise experimental evaluation.

The fabrication technique – electroplating formed polycarbonate foils – produced partial sphere targets of high quality and surface finish, especially on the proton emitting, concave side. While the original dies used for the shaping of the Polycarbonate were limited by the availability of steel balls, improved machining capabilities allow for custom dies for higher quality and consistency of the spheres, or for other shapes like ellipsoids. The improved machining and measurement capabilities also allows for a more precise and consistent mount of the secondary targets, additionally ensuring an even more consistent partial sphere apex to secondary target distance. Looking ahead, an expansion of the automation in all stages is planned. An automated heated press is under development along with a streamlined setup for electroplating and measurements, increasing the number of targets produced while reducing cost. Going beyond 10000 identical partial sphere targets will be feasible in the near future via a cooperation with the 'Institut für Produktionstechnik und Umformmaschinen' (PtU) at TU Darmstadt, where metal foils under 15 µm are being formed into partial sphere or conical shapes.

Alignment Procedure Automated metrology using a confocal scanning profilometer enabled a statistical evaluation of every partial sphere target produced. Enabled by these measurements, a new two part alignment method was developed, greatly reducing the time required to precisely align batches of 200 targets on-site, boosting the target throughput during the experiment. The precision of the alignment was, with the highest contribution, limited by the geometrical error of the linear axis (pitch, straightness etc.). Expanding the

---

[1] ISO 25178-2:2021 ("Geometrical product specifications (GPS) – Surface texture: Areal – Part 2: Terms, definitions and surface texture parameters", 2023)

imaging recognition modules developed for the evaluation of the system and incorporating a calibration target frame will enhance the accuracy of the alignment system for future campaigns, by characterizing and compensating the geometrical errors. The combination of state-of-the-art batch fabrication and efficient semi-automatic alignment procedures removes a bottleneck present for complex targets at medium repetition rate facilities, opening the door to perform extensive parametric studies in high-intensity laser-plasma interactions.

Focusing of Laser Driven Proton Beams Proton Fast Ignition is an advanced ignition scheme separating the stages of deuterium-tritium (DT) fuel compression and heating, potentially achieving higher target gains and robust performances. Once the fuel is compressed by ns-scale laser pulses, an energetic proton beam is generated through target normal sheath acceleration (TNSA) during the interaction of a ps-scale laser pulse with a partial sphere target, which is protected from the implosion by a surrounding cone. The particles then heat a small volume of the compressed fuel to $\sim 10\,\mathrm{eV}$, initiating ignition and burn. The success of this approach relies on the ability to generate a proton beam with the right characteristics to heat and ignite the isochoric DT fuel assembly. Similarly the focused protons can be utilized to heat samples allowing for the study of Warm Dense Matter (WDM). A comprehensive experimental campaign at the L-ALEPH laser facility investigated these, for PFI critical, focusing properties of proton beams from partial-sphere targets. The results served to validate PIC simulations conducted for three target geometries ($\varnothing 220\,\mu\mathrm{m}, \varnothing 325\,\mu\mathrm{m}$ and $\varnothing 525\,\mu\mathrm{m}$), considering the parameters of the L-ALEPH laser system. A mesh-RCF diagnostic setup provided energy resolved beam size measurements at the location of the secondary mesh plane, $\sim 280\,\mu\mathrm{m}$ to $960\,\mu\mathrm{m}$ from the concave apex, as well as at the virtual focus position. The virtual focus position was, within the margin of error, independent of the protons' energy and the secondary mesh position. This indicated a ballistic trajectory of the protons as early as $280\,\mu\mathrm{m}$ for all targets. Smaller, well illuminated targets[2] ($\varnothing, \Psi = 220\,\mu\mathrm{m}, 6$) exhibited an extended collimation range, whereas the largest target ($\varnothing, \Psi = 525\,\mu\mathrm{m}, 13$) with the poorest illumination showed almost no collimation.

The fluctuations observed in the measured data, despite high accuracy target alignment and stable pointing, highlight the necessity of multiple measurements and statistical evaluation for each configuration when studying laser driven proton beams. This emphasizes the advantage of multiple measurements over single shot data in past experiments.

Additional measurements using a XUV imager, observed thermal emission from a secondary foil placed at two different distances downstream from the partial sphere's apex. These data indicate that smaller, well-illuminated spheres indeed produce a collimated beam well beyond the geometrical center (covering an extended distance of $\approx 280\,\mu\mathrm{m}$), while heating the target to $\sim 15\,\mathrm{eV}$. Both diagnostics compare well with Particle in Cell (PIC) simulations performed with the EPOCH (Arber et al., 2015) code, validating the code's reliability in modeling proton focusing from partial sphere targets.

Future Directions and Related Facilities. Building upon these results, an experiment is planned at the ZEUS laser facility (ZEUS, 2025) in October 2025, where a significantly larger focal spot of $\sim 100\,\mu\mathrm{m}$ FWHM, compared to the $\sim 40\,\mu\mathrm{m}$ FWHM of L-ALEPH, will enable an illumination parameter approaching unity. This regime would be challenging to achieve with smaller beams, as it would require exceptionally small partial spheres, extraordinarily tight alignment tolerances, and minimal pointing fluctuations. ZEUS can deliver up to $75\,\mathrm{J}$ in $25\,\mathrm{fs}$ pulses at a repetition rate of one shot per minute, making it suitable for large parametric scans similar to those carried out at CSU. The experiment will include both isochoric heating studies with an XUV imager and mesh radiography with scintillator-based detectors, aiming to replace conventional RCF for radiography applications. Lessons learned at CSU, particularly about target manufacturing, characterization, and alignment, will be applied. In parallel, a recent campaign at the OMEGA EP (Omega EP, 2025) in February

---

[2] $\Psi = D_{\mathrm{Target}}/D_{\mathrm{Laser}}$

2025 used similar partial sphere targets to investigate proton focusing in the $\sim 1\,\mathrm{kJ}, 10\,\mathrm{ps}$ regime. Although its shot rate is far lower (about nine shots in a 13-hour day), OMEGA EP is ideally positioned to explore a regime of higher laser energy and longer pulse durations, more closely resembling that of proton fast ignition. While the energies orders of magnitude lower than those at PFI scale, no existing facility can yet access that regime. This then represents the closest experimental regime available to date to study laser driven proton acceleration in the context of PFI.

Next-generation facilities like ELI L4 (L4 ATON, 2025), combine the best of both worlds: high energy and a moderate repetition rate, allowing for future advancements in PFI , by enabling large parameter studies required to optimize conversion efficiency and focusing.

Bibliography

A. Kramida, Yu. Ralchenko, J. Reader, & and NIST ASD Team. (2023).

AgarScientific. (2024a). Square 400 mesh tem support grids [Accessed: 2024-09-12]. https://www.agarscientific.com/square-400-mesh-tem-support-grids

AgarScientific. (2024b). Square 600 mesh tem support grids [Accessed: 2024-09-12]. https://www.agarscientific.com/tem/grids-agar/square-mesh/square-600-mesh-tem-support-grids

Altan, T., & Tekkaya, A. E. (Eds.). (2012). *Sheet metal forming: Processes and applications*. ASM International.

Arber, T. D., Bennett, K., Brady, C. S., Lawrence-Douglas, A., Ramsay, M. G., Sircombe, N. J., Gillies, P., Evans, R. G., Schmitz, H., Bell, A. R., & Ridgers, C. P. (2015). Contemporary particle-in-cell approach to laser-plasma modelling. *Plasma Physics and Controlled Fusion*, *57*(11), 113001. https://doi.org/10.1088/0741-3335/57/11/113001

Ashland. (2021). Gafchromic HD-V2 Protocol [Accessed: 2024-09-10]. https://www.ashland.com/file_source/Ashland/Documents/PHA21-008_Gafchromic%20HD-V2%20Protocol.pdf

Atzeni, S., Temporal, M., & Honrubia, J. (2002). A first analysis of fast ignition of precompressed ICF fuel by laser-accelerated protons. *Nuclear Fusion*, *42*(3), L1–L4. https://doi.org/10.1088/0029-5515/42/3/101

Bartal, T., Flippo, K. A., Gaillard, S. A., Offermann, D. T., Foord, M. E., Bellei, C., Patel, P. K., Key, M. H., Stephens, R. B., McLean, H. S., Jarrott, L. C., & Beg, F. N. (2011). Proton Focusing Characteristics Relevant to Fast Ignition. *IEEE Transactions on Plasma Science*, *39*(11), 2818–2819. https://doi.org/10.1109/TPS.2011.2155682

Bartal, T., Foord, M. E., Bellei, C., Key, M. H., Flippo, K. A., Gaillard, S. A., Offermann, D. T., Patel, P. K., Jarrott, L. C., Higginson, D. P., Roth, M., Otten, A., Kraus, D., Stephens, R. B., McLean, H. S., Giraldez, E. M., Wei, M. S., Gautier, D. C., & Beg, F. N. (2012). Focusing of short-pulse high-intensity laser-accelerated proton beams. *Nature Physics*, *8*(2), 139–142. https://doi.org/10.1038/nphys2153

Bartal, T. J. (2012). *Investigation of proton focusing and conversion efficiency for proton fast ignition*.

Batani, D., Joachain, C. J., Martellucci, S., & Chester, A. N. (Eds.). (2001). *Atoms, Solids, and Plasmas in Super-Intense Laser Fields*. Springer US. https://doi.org/10.1007/978-1-4615-1351-3

Borghesi, M., Campbell, D. H., Schiavi, A., Haines, M. G., Willi, O., MacKinnon, A. J., Patel, P., Gizzi, L. A., Galimberti, M., Clarke, R. J., Pegoraro, F., Ruhl, H., & Bulanov, S. (2002). Electric field detection in laser-plasma interaction experiments via the proton imaging technique. *Physics of Plasmas*, *9*(5), 2214–2220. https://doi.org/10.1063/1.1459457

Borghesi, M., Fuchs, J., Bulanov, S. V., MacKinnon, A. J., Patel, P. K., & Roth, M. (2006). Fast Ion Generation by High-Intensity Laser Irradiation of Solid Targets and Applications. *Fusion Science and Technology*, *49*(3), 412–439. https://doi.org/10.13182/FST06-A1159

Borghesi, M., Mackinnon, A. J., Campbell, D. H., Hicks, D. G., Kar, S., Patel, P. K., Price, D., Romagnani, L., Schiavi, A., & Willi, O. (2004). Multi-MeV Proton Source Investigations in Ultraintense Laser-Foil Interactions. *Physical Review Letters*, *92*(5), 055003. https://doi.org/10.1103/PhysRevLett.92.055003

Borneis, S., Laštovička, T., Sokol, M., Jeong, T.-M., Condamine, F., Renner, O., Tikhonchuk, V., Bohlin, H., Fajstavr, A., Hernandez, J.-C., Jourdain, N., Kumar, D., Modřanský, D., Pokorný, A., Wolf, A., Zhai, S., Korn, G., & Weber, S. (2021). Design, installation and commissioning of the ELI-Beamlines high-power, high-repetition rate HAPLS laser beam transport system to P3. *High Power Laser Science and Engineering*, *9*, e30. https://doi.org/10.1017/hpl.2021.16

Brambrink, E., Schreiber, J., Schlegel, T., Audebert, P., Cobble, J., Fuchs, J., Hegelich, M., & Roth, M. (2006). Transverse Characteristics of Short-Pulse Laser-Produced Ion Beams: A Study of the Acceleration Dynamics. *Physical Review Letters*, *96*(15), 154801. https://doi.org/10.1103/PhysRevLett.96.154801

Brunel, F. (1987). Not-so-resonant, resonant absorption. *Physical Review Letters*, *59*(1), 52–55. https://doi.org/10.1103/PhysRevLett.59.52

C. S. Liu, Tripathi, V. K., & Eliasson, B. (2020, October 1). *High-Power Laser-Plasma Interaction:* (1st ed.). Cambridge University Press. https://doi.org/10.1017/9781108635844

Carroll, D. C., McKenna, P., Lundh, O., Lindau, F., Wahlström, C.-G., Bandyopadhyay, S., Pepler, D., Neely, D., Kar, S., Simpson, P. T., Markey, K., Zepf, M., Bellei, C., Evans, R. G., Redaelli, R., Batani, D., Xu, M. H., & Li, Y. T. (2007). Active manipulation of the spatial energy distribution of laser-accelerated proton beams. *Physical Review E*, *76*(6), 065401. https://doi.org/10.1103/PhysRevE.76.065401

Chen, F. F. (2016). *Introduction to Plasma Physics and Controlled Fusion*. Springer International Publishing. https://doi.org/10.1007/978-3-319-22309-4

Chen, S. N., d'Humières, E., Lefebvre, E., Romagnani, L., Toncian, T., Antici, P., Audebert, P., Brambrink, E., Cecchetti, C. A., Kudyakov, T., Pipahl, A., Sentoku, Y., Borghesi, M., Willi, O., & Fuchs, J. (2012). Focusing Dynamics of High-Energy Density, Laser-Driven Ion Beams. *Physical Review Letters*, *108*(5), 055001. https://doi.org/10.1103/PhysRevLett.108.055001

Chen, S. N., Gauthier, M., Bazalova-Carter, M., Bolanos, S., Glenzer, S., Riquier, R., Revet, G., Antici, P., Morabito, A., Propp, A., Starodubtsev, M., & Fuchs, J. (2016). Absolute dosimetric characterization of Gafchromic EBT3 and HDv2 films using commercial flat-bed scanners and evaluation of the scanner response function variability. *Review of Scientific Instruments*, *87*(7), 073301. https://doi.org/10.1063/1.4954921

Chung, H.-K., Chen, M., Morgan, W., Ralchenko, Y., & Lee, R. (2005). FLYCHK: Generalized population kinetics and spectral model for rapid spectroscopic analysis for all elements. *High Energy Density Physics*, *1*(1), 3–12. https://doi.org/10.1016/j.hedp.2005.07.001

Colombier, J. P., Combis, P., Bonneau, F., Le Harzic, R., & Audouard, E. (2005). Hydrodynamic simulations of metal ablation by femtosecond laser irradiation. *Physical Review B*, *71*(16), 165406. https://doi.org/10.1103/PhysRevB.71.165406

Cowan, T. E., Fuchs, J., Ruhl, H., Kemp, A., Audebert, P., Roth, M., Stephens, R., Barton, I., Blazevic, A., Brambrink, E., Cobble, J., Fernández, J., Gauthier, J.-C., Geissel, M., Hegelich, M., Kaae, J., Karsch, S., Le Sage, G. P., Letzring, S., … Renard-LeGalloudec, N. (2004). Ultralow Emittance, Multi-MeV Proton Beams from a Laser Virtual-Cathode Plasma Accelerator. *Physical Review Letters*, *92*(20), 204801. https://doi.org/10.1103/PhysRevLett.92.204801

Cox, G. (2012). *Optical Imaging Techniques in Cell Biology, Second Edition* (2nd ed.). https://doi.org/10.1201/b12135

Craxton, R. S., Anderson, K. S., Boehly, T. R., Goncharov, V. N., Harding, D. R., Knauer, J. P., McCrory, R. L., McKenty, P. W., Meyerhofer, D. D., Myatt, J. F., Schmitt, A. J., Sethian, J. D., Short, R. W., Skupsky, S., Theobald, W., Kruer, W. L., Tanaka, K., Betti, R., Collins, T. J. B., … Zuegel, J. D. (2015). Direct-drive inertial confinement fusion: A review. *Physics of Plasmas*, *22*(11), 110501. https://doi.org/10.1063/1.4934714

D West & A . C. Sherwood. (1972). Radiography with 160 MeV Protons. *Nature*, *239*(5368), 157–157. https://doi.org/10.1038/239157a0

Daido, H., Nishiuchi, M., & Pirozhkov, A. S. (2012). Review of laser-driven ion sources and their applications. *Reports on Progress in Physics*, *75*(5), 056401. https://doi.org/10.1088/0034-4885/75/5/056401

Dufour, J. D. (2006). *An introduction to metallurgy* (4th) [Revised and Enlarged Edition]. Cooper Cameron Corporation.

Ehret, M., de Luis, D., Lera, R., Perez-Hernandez, J. A., Puyuelo-Valdes, P., & Gatti, G. (2023). High-repetition-rate solid tape target delivery system for ultra-intense laser-matter interaction at CLPU.

Elliott, A. D. (2020). Confocal Microscopy: Principles and Modern Practices. *Current Protocols in Cytometry*, *92*(1), e68. https://doi.org/10.1002/cpcy.68

Encyclopaedia Britannica. (2024). *Faraday's laws of electrolysis* [Accessed: 2024-09-06]. https://www.britannica.com/science/Faradays-laws-of-electrolysis

Fernández, J., Albright, B., Beg, F., Foord, M., Hegelich, B., Honrubia, J., Roth, M., Stephens, R., & Yin, L. (2014). Fast ignition with laser-driven proton and ion beams. *Nuclear Fusion*, *54*(5), 054006. https://doi.org/10.1088/0029-5515/54/5/054006

Fuchs, J., Antici, P., d'Humières, E., Lefebvre, E., Borghesi, M., Brambrink, E., Cecchetti, C. A., Kaluza, M., Malka, V., Manclossi, M., Meyroneinc, S., Mora, P., Schreiber, J., Toncian, T., Pépin, H., & Audebert, P. (2006). Laser-driven proton scaling laws and new paths towards energy increase. *Nature Physics*, *2*(1), 48–54. https://doi.org/10.1038/nphys199

Fuchs, J., Cowan, T. E., Audebert, P., Ruhl, H., Gremillet, L., Kemp, A., Allen, M., Blazevic, A., Gauthier, J.-C., Geissel, M., Hegelich, M., Karsch, S., Parks, P., Roth, M., Sentoku, Y., Stephens, R., & Campbell, E. M. (2003). Spatial Uniformity of Laser-Accelerated Ultrahigh-Current MeV Electron Propagation in Metals and Insulators. *Physical Review Letters*, *91*(25), 255002. https://doi.org/10.1103/PhysRevLett.91.255002

Gales, S., Tanaka, K. A., Balabanski, D. L., Negoita, F., Stutman, D., Tesileanu, O., Ur, C. A., Ursescu, D., Andrei, I., Ataman, S., Cernaianu, M. O., D'Alessi, L., Dancus, I., Diaconescu, B., Djourelov, N., Filipescu, D., Ghenuche, P., Ghita, D. G., Matei, C., … Zamfir, N. V. (2018). The extreme light infrastructure—nuclear physics (ELI-NP) facility: New horizons in physics with 10 PW ultra-intense lasers and 20 MeV brilliant gamma beams. *Reports on Progress in Physics*, *81*(9), 094301. https://doi.org/10.1088/1361-6633/aacfe8

Geometrical product specifications (GPS) – Surface texture: Areal – Part 2: Terms, definitions and surface texture parameters. (2023).

Geometrical product specifications (GPS) – Surface texture: Areal – Part 3: Specification operators. (2012).

Gibbon, P. (2016). Introduction to Plasma Physics. *CERN Yellow Reports*, 51 Pages. https://doi.org/10.5170/CERN-2016-001.51

Gibbon, P. (2005). *Short pulse laser interactions with matter: An introduction*. Imperial College Press. OCLC: ocm62673761.

Gibbon, P., & Bell, A. R. (1992). Collisionless absorption in sharp-edged plasmas. *Physical Review Letters*, *68*(10), 1535–1538. https://doi.org/10.1103/PhysRevLett.68.1535

Goodfellow. (2023a). Aluminium foil - technical data sheet [Product Code: A-00-FL-000114, Purity: 99%, Thickness: 0.005 mm, CAS Number: 7429-90-5]. https://www.goodfellow.com/de/aluminium-foil-1000000006

Goodfellow. (2023b). Copper foil - technical data sheet [Product Code: CU00-FL-000110, Purity: 99.97%, Thickness: 0.002 mm, CAS Number: 7440-50-8]. https://www.goodfellow.com/de/copper-foil-1000045722

Gugua, E. C., Ujah, C. O., Asadu, C. O., Von Kallon, D. V., & Ekwueme, B. N. (2024). Electroplating in the modern era, improvements and challenges: A review. *Hybrid Advances*, *7*, 100286. https://doi.org/10.1016/j.hybadv.2024.100286

Hatchett, S. P., Brown, C. G., Cowan, T. E., Henry, E. A., Johnson, J. S., Key, M. H., Koch, J. A., Langdon, A. B., Lasinski, B. F., Lee, R. W., Mackinnon, A. J., Pennington, D. M., Perry, M. D., Phillips, T. W., Roth, M., Sangster, T. C., Singh, M. S., Snavely, R. A., Stoyer, M. A., … Yasuike, K. (2000). Electron, photon, and ion beams from the relativistic interaction of Petawatt laser pulses with solid targets. *Physics of Plasmas*, *7*(5), 2076–2082. https://doi.org/10.1063/1.874030

Henke, B., Gullikson, E., & Davis, J. (1993). X-ray interactions: Photoabsorption, scattering, transmission, and reflection at E = 50-30,000 eV, Z = 1-92. *Atomic Data and Nuclear Data Tables*, *54*(2), 181–342. https://doi.org/10.1006/adnd.1993.1013

Hicks, G. S., Dover, N. P., Nichols, R., Posocco, P., Najmudin, Z., & Green, J. S. (2013). Proton spectra calculation from Radiochromic Film stacks with high-energy proton correction.

Higginson, A. (2018). Optimisation and Control of Ion Acceleration in Intense Laser-Foil Interactions, 201.

Honrubia, J. J., Fernandez, J. C., Temporal, M., Hegelich, B. M., & Meyer-ter-Vehn, J. (2009). Fast ignition of inertial fusion targets by laser-driven carbon beams. *Physics of Plasmas*, *16*(10), 102701. https://doi.org/10.1063/1.3234248

Jordan, H.-J., Wegner, M., & Tiziani, H. (1998). Highly accurate non-contact characterization of engineering surfaces using confocal microscopy. *Measurement Science and Technology*, *9*(7), 1142–1151. https://doi.org/10.1088/0957-0233/9/7/023

Kar, S., Borghesi, M., Romagnani, L., Patel, P. K., Mackinnon, A. J., Snavely, R., Key, M. H., King, J. A., Zhang, B., Akli, K. U., Freeman, R. R., Clarke, R. J., Heathcote, R., & Neely, D. (2004). Focusing of laser produced proton beams by using hemispherical targets, 3.

Kaymak, V., Aktan, E., Cerchez, M., Elkin, B., Papenheim, M., Prasad, R., Pukhov, A., Scheer, H.-C., Schroer, A.-M., Willi, O., & Aurand, B. (2019). Boosted acceleration of protons by tailored ultra-thin foil targets. *Scientific Reports*, *9*(1), 18672. https://doi.org/10.1038/s41598-019-55011-2

Keldysh, L. V. (1964). Ionization in the field of a strong electromagnetic wave. *Zh. Eksperim. i Teor. Fiz.*, *Vol: 47*. https://www.osti.gov/biblio/4662394

Kim, H. T. (2023, December 1). *Laser–Plasma Accelerators and Radiation Sources:* IOP Publishing. https://doi.org/10.1088/978-0-7503-2703-9

Kodama, R., Norreys, P. A., Mima, K., Dangor, A. E., Evans, R. G., Fujita, H., Kitagawa, Y., Krushelnick, K., Miyakoshi, T., Miyanaga, N., Norimatsu, T., Rose, S. J., Shozaki, T., Shigemori, K., Sunahara, A., Tampo, M., Tanaka, K. A., Toyama, Y., Yamanaka, T., & Zepf, M. (2001). Fast heating of ultrahigh-density plasma as a step towards laser fusion ignition. *Nature*, *412*(6849), 798–802. https://doi.org/10.1038/35090525

Kruer, W. L. (1988, July 11). Long Pulse Laser-Plasma Interactions. In H. A. Baldis & E. M. Campbell (Eds.). https://doi.org/10.1117/12.965116

L4 ATON. (2025). Laser 4 - aton 10 pw 2 kj, eli beamlines [Accessed: 2025-03-13].

Leach, R. (Ed.). (2011). *Optical Measurement of Surface Topography*. Springer Berlin Heidelberg. https://doi.org/10.1007/978-3-642-12012-1

Leemans, W. P., Gonsalves, A. J., Nakamura, K., Mao, H.-S., Toth, C., Daniels, J., Mittelberger, D., Benedetti, C., Bulanov, S., Geddes, C. G. R., Vay, J.-L., Schroeder, C. B., & Esarey, E. H. (2014). Laser plasma acceleration using the pw-class bella laser. *CLEO: 2014*, JTh1L.1. https://doi.org/10.1364/CLEO_AT.2014.JTh1L.1

Lucke, P., Last, A., Mohr, J., Ruprecht, A. K., Pruss, C., Tiziani, H. J., Osten, W., Lehmann, P., & Schonfelder, S. (2005, June 13). Confocal micro-optical distance sensor: Realization and results. In W. Osten, C. Gorecki, & E. L. Novak (Eds.). https://doi.org/10.1117/12.612418

Macchi, A., Borghesi, M., & Passoni, M. (2013). Ion acceleration by superintense laser-plasma interaction. *Reviews of Modern Physics*, *85*(2), 751–793. https://doi.org/10.1103/RevModPhys.85.751

Mark, J. E. (1999). Polymer Data Handbook.

McGuffey, C., Kim, J., Wei, M. S., Nilson, P. M., Chen, S. N., Fuchs, J., Fitzsimmons, P., Foord, M. E., Mariscal, D., McLean, H. S., Patel, P. K., Stephens, R. B., & Beg, F. N. (2020). Focussing Protons from a Kilojoule

Laser for Intense Beam Heating using Proximal Target Structures. *Scientific Reports*, *10*(1), 9415. https://doi.org/10.1038/s41598-020-65554-4

McKenna, P., Ledingham, K. W. D., Yang, J. M., Robson, L., McCanny, T., Shimizu, S., Clarke, R. J., Neely, D., Spohr, K., Chapman, R., Singhal, R. P., Krushelnick, K., Wei, M. S., & Norreys, P. A. (2004). Characterization of proton and heavier ion acceleration in ultrahigh-intensity laser interactions with heated target foils. *Physical Review E*, *70*(3), 036405. https://doi.org/10.1103/PhysRevE.70.036405

McLaughlin, W., Yun-Dong, C., Soares, C., Miller, A., Van Dyk, G., & Lewis, D. (1991). Sensitometry of the response of a new radiochromic film dosimeter to gamma radiation and electron beams. *Nuclear Instruments and Methods in Physics Research Section A: Accelerators, Spectrometers, Detectors and Associated Equipment*, *302*(1), 165–176. https://doi.org/10.1016/0168-9002(91)90506-L

Michel, P. (2023). *Introduction to Laser-Plasma Interactions*. Springer International Publishing. https://doi.org/10.1007/978-3-031-23424-8

Minsky, M. (1961). My invention relates to a new and improved electronic microscope apparatus and to a novel apparatus for mi.

Nakamura, K., Mao, H.-S., Gonsalves, A. J., Vincenti, H., Mittelberger, D. E., Daniels, J., Magana, A., Toth, C., & Leemans, W. P. (2017). Diagnostics, control and performance parameters for the bella high repetition rate petawatt class laser. *IEEE Journal of Quantum Electronics*, *53*(4), 1–21. https://doi.org/10.1109/JQE.2017.2708601

Nishiuchi, M., Kiriyama, H., Sakaki, H., Dover, N. P., Kondo, K., Pirozhkov, A. S., Sagisaka, A., Fukuda, Y., Nishitani, K., Miyahara, T., Ogura, K., Alkhimova, M. A., Pikuz, T. A., Faenov, A. Y., Watanabe, Y., Koga, J., Bulanov, S. V., Kando, M., & Kondo, K. (2017). High contrast high intensity petawatt J-KAREN-P laser facility at QST. In G. Korn & L. O. Silva (Eds.), *Research using extreme light: Entering new frontiers with petawatt-class lasers iii* (102410N, Vol. 10241). SPIE. https://doi.org/10.1117/12.2271172

Nuckolls, J., Wood, L., Thiessen, A., & Zimmerman, G. (1972). Laser Compression of Matter to Super-High Densities: Thermonuclear (CTR) Applications. *Nature*, *239*(5368), 139–142. https://doi.org/10.1038/239139a0

Nürnberg, F., Schollmeier, M., Brambrink, E., Blažević, A., Carroll, D. C., Flippo, K., Gautier, D. C., Geißel, M., Harres, K., Hegelich, B. M., Lundh, O., Markey, K., McKenna, P., Neely, D., Schreiber, J., & Roth, M. (2009). Radiochromic film imaging spectroscopy of laser-accelerated proton beams. *Review of Scientific Instruments*, *80*(3), 033301. https://doi.org/10.1063/1.3086424

Offermann, D. T., Flippo, K. A., Cobble, J., Schmitt, M. J., Gaillard, S. A., Bartal, T., Rose, D. V., Welch, D. R., Geissel, M., & Schollmeier, M. (2011). Characterization and focusing of light ion beams generated by ultra-intensely irradiated thin foils at the kilojoule scale. *Physics of Plasmas*, *18*(5), 056713. https://doi.org/10.1063/1.3589476

Omega EP. (2025). Omega laser facility [Accessed: 2025-03-13].

Paunovic, M. (2010). Modern Electroplating.

Pelka, A., Gregori, G., Gericke, D. O., Vorberger, J., Glenzer, S. H., Günther, M. M., Harres, K., Heathcote, R., Kritcher, A. L., Kugland, N. L., Li, B., Makita, M., Mithen, J., Neely, D., Niemann, C., Otten, A., Riley, D., Schaumann, G., Schollmeier, M., … Roth, M. (2010). Ultrafast Melting of Carbon Induced by Intense Proton Beams. *Physical Review Letters*, *105*(26), 265701. https://doi.org/10.1103/PhysRevLett.105.265701

Piel, A. (2010). *Plasma Physics: An Introduction to Laboratory, Space, and Fusion Plasmas*. Springer Berlin Heidelberg. https://doi.org/10.1007/978-3-642-10491-6

Qiao, B., Foord, M. E., Wei, M. S., Stephens, R. B., Key, M. H., McLean, H., Patel, P. K., & Beg, F. N. (2013). Dynamics of high-energy proton beam acceleration and focusing from hemisphere-cone targets by high-intensity lasers. *Physical Review E*, *87*(1), 013108. https://doi.org/10.1103/PhysRevE.87.013108

Romagnani, L., Fuchs, J., Borghesi, M., Antici, P., Audebert, P., Ceccherini, F., Cowan, T., Grismayer, T., Kar, S., Macchi, A., Mora, P., Pretzler, G., Schiavi, A., Toncian, T., & Willi, O. (2005). Dynamics of Electric Fields Driving the Laser Acceleration of Multi-MeV Protons. *Physical Review Letters*, *95*(19), 195001. https://doi.org/10.1103/PhysRevLett.95.195001

Roth, M., Allen, M., Audebert, P., Blazevic, A., Brambrink, E., Cowan, T. E., Fuchs, J., Gauthier, J.-C., Gei el, M., Hegelich, M., Karsch, S., Meyer-ter-Vehn, J., Ruhl, H., Schlegel, T., & Stephens, R. B. (2002). The generation of high-quality, intense ion beams by ultra-intense lasers. *Plasma Physics and Controlled Fusion*, *44*, B99–B108. https://doi.org/10.1088/0741-3335/44/12B/308

Roth, M., Cowan, T. E., Key, M. H., Hatchett, S. P., Brown, C., Fountain, W., Johnson, J., Pennington, D. M., Snavely, R. A., Wilks, S. C., Yasuike, K., Ruhl, H., Pegoraro, F., Bulanov, S. V., Campbell, E. M., Perry, M. D., & Powell, H. (2001). Fast Ignition by Intense Laser-Accelerated Proton Beams. *Physical Review Letters*, *86*(3), 436–439. https://doi.org/10.1103/PhysRevLett.86.436

Roth, M., Jung, D., Falk, K., Guler, N., Deppert, O., Devlin, M., Favalli, A., Fernandez, J., Gautier, D., Geissel, M., Haight, R., Hamilton, C. E., Hegelich, B. M., Johnson, R. P., Merrill, F., Schaumann, G., Schoenberg, K., Schollmeier, M., Shimada, T., … Wurden, G. A. (2013). Bright Laser-Driven Neutron Source Based on the Relativistic Transparency of Solids. *Physical Review Letters*, *110*(4), 044802. https://doi.org/10.1103/PhysRevLett.110.044802

Roth, M., & Schollmeier, M. (2016). Ion Acceleration - Target Normal Sheath Acceleration. *CERN Yellow Reports*, 231 Pages. https://doi.org/10.5170/CERN-2016-001.231

Schmitz, B., Metternich, M., & Boine-Frankenheim, O. (2024). Automated reconstruction of the initial distribution of laser accelerated ion beams from radiochromic film (RCF) stacks. *Rev. Sci. Instrum.*

Schollmeier, M., Roth, M., Blazevic, A., Brambrink, E., Cobble, J., Fernandez, J., Flippo, K., Gautier, D., Habs, D., Harres, K., Hegelich, B., Heßling, T., Hoffmann, D., Letzring, S., Nürnberg, F., Schaumann, G., Schreiber, J., & Witte, K. (2007). Laser ion acceleration with micro-grooved targets. *Nuclear Instruments and Methods in Physics Research Section A: Accelerators, Spectrometers, Detectors and Associated Equipment*, *577*(1–2), 186–190. https://doi.org/10.1016/j.nima.2007.02.052

Schollmeier, M. S. (2009, January). *Optimization and control of laser-accelerated proton beams* [Doctoral dissertation, Technische Universität Darmstadt]. http://tuprints.ulb.tu-darmstadt.de/1232/

Siciliano, B., Sciavicco, L., Villani, L., & Oriolo, G. (2009). *Robotics* (M. J. Grimble & M. A. Johnson, **typeredactors**). Springer London. https://doi.org/10.1007/978-1-84628-642-1

Snavely, R. A., Key, M. H., Hatchett, S. P., Cowan, T. E., Roth, M., Phillips, T. W., Stoyer, M. A., Henry, E. A., Sangster, T. C., Singh, M. S., Wilks, S. C., MacKinnon, A., Offenberger, A., Pennington, D. M., Yasuike, K., Langdon, A. B., Lasinski, B. F., Johnson, J., Perry, M. D., & Campbell, E. M. (2000). Intense High-Energy Proton Beams from Petawatt-Laser Irradiation of Solids. *Physical Review Letters*, *85*(14), 2945–2948. https://doi.org/10.1103/PhysRevLett.85.2945

Snavely, R. A., Zhang, B., Akli, K., Chen, Z., Freeman, R. R., Gu, P., Hatchett, S. P., Hey, D., Hill, J., Key, M. H., Izawa, Y., King, J., Kitagawa, Y., Kodama, R., Langdon, A. B., Lasinski, B. F., Lei, A., MacKinnon, A. J., Patel, P., … Zheng, J. (2007). Laser generated proton beam focusing and high temperature isochoric heating of solid matter. *Physics of Plasmas*, *14*(9), 092703. https://doi.org/10.1063/1.2774001

Strickland, D., & Mourou, G. (1985). Compression of amplified chirped optical pulses. *Optics communications*, *55*(6), 447–449.

Tabak, M., Hammer, J., Glinsky, M. E., Kruer, W. L., Wilks, S. C., Woodworth, J., Campbell, E. M., Perry, M. D., & Mason, R. J. (1994). Ignition and high gain with ultrapowerful lasers*. *Physics of Plasmas*, *1*(5), 1626–1634. https://doi.org/10.1063/1.870664

Todd, R. H., Allen, D. K., & Alting, L. (1994). Manufacturing processes reference guide. *Industrial Press Inc.*

Umicore Galvanotechnik GmbH. (2009, June). *Auruna® 552 arbeitsanleitung* [Stand: 15. Juli 2009]. Schwäbisch Gmünd, Germany. https://www.umicore-galvano.com

Wang, Y., Wang, S., Rockwood, A., Luther, B. M., Hollinger, R., Curtis, A., Calvi, C., Menoni, C. S., & Rocca, J. J. (2017). 085 PW laser operation at 33 Hz and high-contrast ultrahigh-intensity $\lambda = 400$ nm second-harmonic beamline. *Optics Letters*, *42*(19), 3828. https://doi.org/10.1364/OL.42.003828

Wilcox, G., & Gabe, D. R. (1992). 1. faraday's laws of electrolysis. *Transactions of The Institute of Metal Finishing*. https://doi.org/10.1080/00202967.1992.11870951

Wilkinson, P. (1986). Understanding gold plating. *Gold Bulletin*, *19*(3), 75–81. https://doi.org/10.1007/BF03214646

Wilks, S. C., Kruer, W. L., Tabak, M., & Langdon, A. B. (1992). Absorption of ultra-intense laser pulses. *Physical Review Letters*, *69*(9), 1383–1386. https://doi.org/10.1103/physrevlett.69.1383

Wilks, S. C., Langdon, A. B., & Cowan, T. E. (2001). Energetic proton generation in ultra-intense laser–solid interactions. *Phys. Plasmas*, *8*(2), 9.

Wilks, S., & Kruer, W. (1997). Absorption of ultrashort, ultra-intense laser light by solids and overdense plasmas. *IEEE Journal of Quantum Electronics*, *33*(11), 1954–1968. https://doi.org/10.1109/3.641310

Wilson, R. R. (1946). Radiological Use of Fast Protons. *Radiology*, *47*(5), 487–491. https://doi.org/10.1148/47.5.487

Xu, N., Streeter, M. J. V., Ettlinger, O. C., Ahmed, H., Astbury, S., Borghesi, M., Bourgeois, N., Curry, C. B., Dann, S. J. D., Dover, N. P., Dzelzainis, T., Istokskaia, V., Gauthier, M., Giuffrida, L., Glenn, G. D., Glenzer, S. H., Gray, R. J., Green, J. S., Hicks, G. S., … Najmudin, Z. (2023). Versatile tape-drive target for high-repetition-rate laser-driven proton acceleration. *High Power Laser Science and Engineering*, *11*, e23. https://doi.org/10.1017/hpl.2023.27

ZEUS. (2025). Zeus laser system, university of michigan [Accessed: 2025-03-13].

Acknowledgment

Ich möchte diese Arbeit mit einem Dank an all diejenigen abschließen, die mich auf diesem Weg begleitet und unterstützt haben.

Mein besonderer Dank gilt meinem Doktorvater Prof. Markus Roth, der mir nicht nur die großartige Erfahrung meine Masterarbeit am LBNL zu erarbeiten ermöglichte, sondern mich auch in seine Arbeitsgruppe aufnahm. Dort konnte ich mich thematisch frei bewegen, Unterstützung einholen und während zahlreicher Reisen um die Welt tolle Erfahrungen sammeln.

Prof. Stephan Kuschel danke ich dafür, dass er meine Dissertation als Koreferent begutachtet. Mein Dank gilt außerdem Prof. Oliver Boine-Frankenheim und Prof. Michael Vogel für ihr Mitwirken am Promotionsverfahren.

Großer Dank geht an Gabriel Schaumann, auf dessen Unterstützung ich mich stets verlassen konnte. Das ermöglichte mir, mich frei in der Gruppe und in meiner Arbeit zu entfalten. Durch sachliche Diskussionen, konstruktive Kritik oder auch einen gemeinsamen Plausch bei einem Espresso hat mir die Zusammenarbeit mit dir große Freude bereitet und mich sowohl fachlich als auch persönlich bereichert.

I would like to sincerely thank Valeria Ospina-Bohórquez and Xavier Vaisseau for their support and investment in this thesis. It would not stand as it does without your input, explanations, and critique. Working with you during the experiments was a delight, and our conversations were immensely valuable not only from an academic point of view, but also personally.

Insbesondere Cora Thom, aber auch meinen Kollegen Patrick Lutz, Jakob Kurzschenkel und Nils Schott möchte ich für die langen und oft stressigen Tage danken, die nötig waren, um die Experimente für die beiden Strahlzeiten in Colorado vorzubereiten.

Christoph Bläser danke ich für die gemeinsamen tollen Jahre im Büro und die gegenseitige Unterstützung. Genauso möchte ich meinen derzeitigen Kollegen Oliver Rothermel, Matthias Resch, Patrick Lutz und Markus Hesse danken, die stets ein offenes Ohr für mich haben und meinen Arbeitsalltag bereichern.

Nicht zu vergessen ist das Team der Mechanischen Werkstatt des Instituts für Kernphysik, das mir jederzeit mit Ratschlägen, Tipps und Tricks zur Seite stand. Ebenso möchte ich dem Team der L-ALEPH Facility danken, das das hier präsentierte Experiment überhaupt erst ermöglicht hat.

Mein Dank gilt auch Judith Feldmann und Markus Domschke vom Dekanat Physik, die stets das Wohl der Studierenden und Promovierenden im Blick haben und verlässliche Unterstützung bieten.

Meinen Freunden danke ich für ihre Rücksicht und ihr Verständnis im vergangenen Jahr, insbesondere Jonas Enes und Tristan Biber für ihr stets offenes Ohr und guten Ratschläge.

Von tiefstem Herzen bin ich meiner Familie dankbar. Nicht nur während dieser Promotion, sondern bereits mein ganzes Leben lang kann ich mich auf eure Unterstützung und Rückendeckung verlassen.

Mein größter Dank gilt Stephanie Karpowski, die nun schon seit mehr als einer Dekade eng an meiner Seite steht. Ohne dich wären die letzten Jahre in dieser Form nicht möglich gewesen. Deine Unterstützung und Liebe sind von unschätzbarem Wert für mich und lassen sich nicht in Worte fassen.

Academic Curriculum Vitae

- **2013** – Obtained the *Abitur* at Ludwig Georgs Gymnasium.
- **2013–2018** – Studied Physics, Bachelor of Science, at the Technical University (TU) Darmstadt.
  - **Bachelor's Thesis:**
    "Design and Implementation of a Segmented Faraday Cup"
    Developed a Faraday Cup with spatial resolution, along with the necessary electronics and software for remote operation.
- **2018–2020** – Studied Physics, Master of Science, at TU Darmstadt.
- **2019–2020** – Recipient of a stipend for conducting the Master's thesis research at Lawrence Berkeley National Laboratory (LBNL).
  - **Master's Thesis:**
    "Development of an Energy Analyzer for a Wafer-Based RF Ion LINAC"
    Hardware development and simulation.
- **2021–2025** – Doctoral Student at the Technical University Darmstadt.